MICRORESPIROMETRY TO STUDY CERAMIDE-INDUCED MITOCHONDRIAL DYSFUNCTION IN DIABETIC RETINOPATHY

By

Yan Levitsky

A DISSERTATION

Submitted to
Michigan State University
in partial fulfillment of the requirements
for the degree of

Physiology—Doctor of Philosophy

2020

ABSTRACT

MICRORESPIROMETRY TO STUDY CERAMIDE-INDUCED MITOCHONDRIAL DYSFUNCTION IN DIABETIC RETINOPATHY

By

Yan Levitsky

Diabetic retinopathy (DR) is a sight-threatening complication of diabetes mellitus and a leading cause of preventable vision loss worldwide. Classically regarded as a vascular disease, the clinically observable lesions and hallmark histopathological findings are found in the vascular compartment. The metabolic insults affecting retinal cells in DR are multifactorial and complex; however, hyperglycemia, dyslipidemia, and chronic inflammation are thought to be major contributors. Diabetic dyslipidemia affects systemic and local lipid metabolism driving the pro-inflammatory and pro-apoptotic retinal cell changes.

Sphingolipids are known to play a key role in cell functioning. Ceramides, the central bioactive sphingolipid species, control cellular responses to cytotoxic stressors. Ceramides can be generated *de novo* or through sphingomyelinase pathways. Important *in vivo* and *in vitro* results have demonstrated that acid sphingomyelinase (ASMase)-induced ceramide generation is a major contributor to retinal barrier cell apoptosis in diabetes. Results from studies in ASMase knockout models have shown that these animals are resistant to an array of cytotoxic insults, confirming that ASMase-dependent ceramide generation is important for apoptosis execution. Recent reports have demonstrated mitochondrial ceramide accumulation in response to cytotoxic insults in animal and *in vitro* models. Limited observations of oxidative metabolism are reported in the literature as limited biological material is an impediment for comprehensive metabolic characterization of retinal cells in the context of DR. Removal of such obstacles lays the foundation for this work.

Comprehensive metabolic examination of DR model systems requires highly sensitive, flexible, and

accurate measurements of cell or organelle oxygen consumption, a functional measure of oxidative metabolism. The instruments which perform such a measurement are called respirometers. Though commercially available options exist they each present unique limitations which can be remediated by rational design of a dedicated microfluidics-based microrespirometer.

The first part of this work focuses on the development of a sensitive and customizable method of measuring O_2 consumption rates by a variety of biological samples in microliter volumes without interference from the aerobic environment. The work demonstrates use of 3D printing utilizing photopolymer (VeroClear) to reproducibly form micron-scale microchannels. The photopolymer demonstrated low oxygen permeability, optical clarity, and, in combination with optode-based O_2 sensing, produced a microrespirometer showing > 100x dynamic range for O_2 consumption rates. Measurements are demonstrated with solution-based, suspension-based, and adherent samples.

The role of ASM-dependent mitochondrial ceramide accumulation in diabetes-induced retinal pigment ephithelial cell damage is described next. Mitochondria isolated from diabetic rat retinas (7 weeks duration) showed an increase in the ceramide-to-sphingomyelin ratio compared to controls whereas, the ceramide-to-sphingomyelin ratio was decreased in mitochondria isolated from ASM-knockout mouse retinas compared to wild-type littermates. Cellular ceramide was elevated in RPE cells derived from diabetic donors compared to control donors, with a corresponding increase in IL-1β, IL-6, and ASM expression. RPE from diabetic donors showed fragmented mitochondria and a decreased respiratory control ratio (RCR). Treatment of ARPE-19 cells with high glucose resulted in a decrease in citrate synthase activity at 72 h. Inhibition of ASM with desipramine (15 μM, 1 h daily) abolished the decreases in metabolic functional parameters. These results are consistent with diabetes-induced increase in mitochondrial ceramide through an ASM-dependent pathway leading to impaired mitochondrial function in RPE cells.

To all my personal giants, whose shoulders allowed me to see so far.

ACKNOWLEDGEMENTS

This work would not be possible without the support and guidance from many people.

I would first like to thank my advisors Dr. Julia V. Busik and Dr. Denis A. Proshlyakov for all their help and guidance in this endeavor. None of this would be possible without their advice. I felt welcome in both labs and am also grateful for all the advice and support they provided in personal life as well. The challenges with which I was presented on this journey have been truly transformative and the lessons will not soon be forgotten.

Apart from my advisors, I would like to extend my sincerest gratitude to my dissertation committee, Dr. Robert Wiseman, Dr. Lawrence (Karl) Olson, Dr. Jason Bazil and Dr. Louis Glazer. Their constant support, advice and encouragement was instrumental in this process and it was a rarity for me to walk away from a conversation without a list of topics to learn about. These challenging and insightful interactions have played an important role in shaping me as a scientist.

I would also like to thank all of the past and present lab members in the Busik and Proshlyakov labs: Dr. Christopher John, Allison Stettler, Nathan Frantz, Emily Groth, Maggie Conway, Artem Muchnik, Adam Fillion, Dr. Chao Huang, Dr. Qi Wang, Dr. Nermin Kady, Svetlana Navitskaya, Kiera Fisher, Travan Gentles, David J. Pegouske, Philip Kirschner and Delaney McFarland. I enjoyed working alongside each of them and especially enjoyed talking shop and learning from each one.

Dr. Sandra S. Hammer, Svetlana Navitskaya, Kiera Fisher, Dr. Christopher John, and Allison Stettler deserve an extra special thank you for the tremendous amount of help they offered me at varying points in this process, both with the science and otherwise.

I would also like to acknowledge my undergraduate assistant David J. Pegouske. He was instrumental in the success of this project and I was honored in taking part of his maturation into a capable and independent member of the lab. He will make an excellent physician one day.

Finally, I want to extend my deepest appreciation to my friends and family. My mother, father and brother have been my support system throughout this program and my life. Despite us being hundreds of miles apart, I never felt like I was alone. I am especially grateful to my mother for abstaining from bodily injury to my person considering all the holidays I did not spend with them. The constant encouragement I received from my friends here in Michigan kept me going in the dark times when I just wanted to give up. I am grateful to each one of you.

This work would not have been possible without the financial support of the National Eye Institute of the National Institutes of Health, the Michigan State University DO/PhD Program, and the Michigan State University Graduate School.

TABLE OF CONTENTS

LIST OF FIGURES

KEY TO ABBREVIATIONS

DM	Diabetes mellitus
DR	Diabetic retinopathy
BRB	Blood-retinal barrier
FIELD	Fenofibrate Intervention and Event Lowering Diabetes
ACCORD	Action to Control Cardiovascular Risk in Diabetes
VEGF	Vascular endothelial growth factor
RPE	Retinal pigment epithelial
ROS	Reactive oxygen species
AGE	Advanced glycation end products
RAGE	Receptors of advanced glycation end products
GAPDH	glyceraldehyde-3-phosphate dehydrogenase
S1P	Sphingosine-1-phosphate
SM	Sphingomyelin
SMases	Sphingomyelinases
ASMase	Acid sphingomyelinase
NADH	Nicotine adenine dinucleotide
$FADH_2$	Flavin adenine dinucleotide

ETC	Electron transport chain
Pmf	Proton motive force
PDMS	Polydimethylsiloxane
CCCP	Carbonyl cyanide m-chlorophenylhydrazone
ATP	Adenosine triphosphate
ADP	Adenosine diphosphate
TCA	Tricarboxylic acid
mGPDH	Mitochondrial glycerophosphate dehydrogenase
DHODH	Dihydroxyorotate dehydrogenase
ETF	Electron transferring flavoprotein
Q	Ubiquinone/ubiquinol pool
TMPD	N,N,N',N' tetramethylphenylenediamine
P_i	Inorganic phosphate
DPBS	Dulbecco's phosphate buffered saline
BSA	Bovine serum albumin
PS	Polystyrene
KCN	Potassium cyanide
PtOEP	Platinum octaethylporphyrin
MfR	Microfluidic respirometer

PEEK	Polyetheretherketone
BREC	Bovine retinal endothelial cells
AA	Antibiotic/Antimycotic
GOx	Glucose oxidase
Glu	Glucose
PMMA	Polymethylmethacrylate
BB_c	Base cellular respiration buffer
RB_c	Respiration buffer
LB_c	Leak buffer
IB_c	Inhibition buffer
MIB	Mitochondrial isolation buffer
R_{O2}	Oxygen consumption rates
N_2	Nitrogen
Glu-GOx	Glucose-glucose oxidase
STZ	Streptozotocin
$ASM^{-/-}$	ASM knockout
nESI	Nano-electrospray ionization
Cer	Ceramide
PBST	Phosphate buffered saline, 1% Tween-10

IL1ß	Interleukin 1ß
IL6	Interleukin 6
ICAM1	Intercellular adhesion molecule 1
VDAC	Voltage-dependent anion channel
IgG	Immunoglobulin G
MS	Mass spectrometry
RCR	Respiratory control ratio
DC	Differential centrifugation
UC	Ultracentrifugation
UDP-glucose	Uridine diphosphate glucose

Chapter 1: Introduction

1.1 Diabetes

Diabetes mellitus (DM) is a chronic metabolic disorder characterized by elevations in serum glucose due to decreased production of insulin from the pancreas, type I diabetes, or impaired tissue response to serum insulin, termed type II diabetes. Corresponding to the rise in obesity and metabolic syndrome, type II diabetes accounts for approximately 90 – 95% of all cases whereas type I diabetes accounts for approximately 5% [1]. Diabetes mellitus is a major health concern with an estimated 10.5% of the current U.S. population affected by the disease [2]. If current incidence trends persist indefinitely, 1 in 3 persons could be diagnosed with diabetes by 2050 [1,2].

The clinical sequelae of diabetes are coarsely grouped into macro- and microvascular complications. The former includes pathologic changes to large caliber vessels increasing the risk for cardiovascular disease and stroke, whereas the latter are characterized by changes to small vessels resulting in diabetic retinopathy, nephropathy, and neuropathy [3]. As the prevalence of DM continues to increase, so too are the complication rates expected to rise. Despite such bleak predictions, delivery of health care is a powerful tool to stem the tide of disease. For instance, the annual incidence of diabetic retinopathy decreased 77% from 1980 to 2007, changes which are attributed to improvements in disease detection and management [4,5].

1.2 Diabetic Retinopathy

1.2.1 Background

In this work, attention is focused on diabetic retinopathy (DR), a common complication of DM and the leading cause of blindness among working age adults [5]. The 10-year incidence of DR has been estimated at 74% with an estimated 20 – 25% of diabetic patients developing sight-threatening macular edema in

the same time period [5]. Though secondary prevention measures and treatments are available, there are no known cures.

1.2.2 Clinical Perspective

Diabetic retinopathy has long been considered a vascular disorder and clinical severity categorizations are based on observation of vascular lesions by fundoscopy. Signs of DR include microaneurysms, small red dots in superficial retinal layers signifying outpouching of a capillary wall. Dot and blot hemorrhages result from microaneurysm rupture whereas exudates accumulate due to leakage of serum through a faulty blood-retinal barrier (BRB). Local nerve-fiber layer infarctions are evident as cotton-wool spots and signal local regions of retinal non-perfusion. Other changes include venous loops and beading as well as remodeling of capillary beds, typically found adjacent to non-perfused regions [6].

Diabetic retinopathy is divided into non-proliferative and proliferative stages, with the former further divided into mild, moderate and severe [6]. Mild non-proliferative DR is characterized by the presence of at least one microaneurysm, whereas the moderate stage requires presence of hemorrhages, microaneurysms and hard exudates [6]. The severe stage follows the 4-2-1 rule; hemorrhages or microaneurysms occur in four quadrants, venous beading in two quadrants and at least one quadrant containing microvascular abnormalities [6]. Progression to the proliferative stage is accompanied by neovascularization, edema, retinal fibrosis and vitreal hemorrhage inducing tractional detachments of the retina [6]. If left untreated, DR progression results in complete vision loss.

1.2.3 Treatment and Prevention

Multidisciplinary secondary prevention of DR progression centers on effective and early DM management, typically in primary care settings. Current standard of care for DM patients focuses on control of serum glucose, lipids, and blood pressure [7–13]. Intensive glycemic control, defined as a hemoglobin $A1_C$ of

approximately 7% or less, to reduce DM complication rates in type I and type II patients has been well supported by landmark clinical trials [10,13,14]. Long lasting protection of early intensive glycemic control has been demonstrated as well. Upon termination of the Diabetes Control and Complications Trial, both the intensive glycemic control- and standard management cohorts were assigned to intensive glycemic control protocol and long-term follow up revealed the persistence of a protective effect in the early glycemic control cohort, indicating that predisposed tissues are irreversibly changed early in the course of DM onset [15]. Such results established the current standard of care which seeks to establish intensive glycemic control as early in the disease process as possible [15]. Despite the strong effect of glycemia normalization to prevent complication onset and progression, the intervention is not curative. In the decades since the glycemia hypothesis has been supported so fully, DR has come to be regarded as complex and multifactorial with disease onset and progression affected by local and systemic factors such as dyslipidemia, blood pressure and inflammation [16,17].

Several observations implicate dyslipidemia in the progression of DR. Firstly, dyslipidemia is associated with formation of hard exudates which are strongly predictive of vision loss [7,16]. Furthermore, the Fenofibrate Intervention and Event Lowering Diabetes (FIELD) study demonstrated the reduced need for laser photocoagulation in DR patients treated with fenofibrate [9,12] whereas the Action to Control Cardiovascular Risk in Diabetes (ACCORD) trial showed that DR progression risk was decreased by about one third when fenofibrate was added to simvastatin compared to simvastatin alone [7,8,13]. Blood pressure management showed similarly protective effects [13]; however, follow up studies failed to show a significant association [18]. Medical management of DM remains the cornerstone of complication risk reduction. These measures, however, are not curative and efforts to develop specific, vision-saving therapies continue.

The earliest effective treatment for DR was pan retinal photocoagulation [19,20]. This technique consists of using high intensity laser light to ablate retinal regions containing abnormal vessels [21]. The proposed

mechanism supposes absorption of the incident laser light by the pigment epithelium resulting in rapid heating and destruction of the outer retina. Though destructive, retinal oxygenation is promoted through the choriocapillaris due to retinal thinning, as well as by a decrease in whole retina oxygen demands due to ablation of photoreceptors [21]. Additionally, elimination of hypoxic or ischemia regions of the neuroretina results in decreased secretion of pro-angiogenic factors, likely playing a role in the protection from disease progression [5,21]. Retinal photocoagulation provided the first vision-preserving treatment indicated for late stage (proliferative) DR; however, the treatment is aimed at preventing progression to frank vision loss and is accompanied by loss of peripheral visual fields, and decreased night vision [21].

Though photocoagulation is still in use today, recent advances in specific medical treatments for DR have focused on controlling the pathological neovascularization process by modulating inflammatory and pro-angiogenic stimuli commonly found in the diabetic retina [17,22]. The most well studied has been vascular endothelial growth factor (VEGF), a pro-angiogenic growth factor secreted in response to ischemia or inflammation resulting in pathogenic retinal vascularization [17]. Though photocoagulation remains a popular choice, aptamer- or immune-based therapies against VEGF as well as intravitreal corticosteroids are options for use in many clinical contexts [7].

1.3 Cellular Changes in Diabetic Retinopathy

The retina is a multilayered neural tissue which transduces photons to electrical currents for transmission to, and interpretation in, the brain. The high metabolic demands of the neuroretina place high perfusion demands on the vascular supply; however, retinal architecture is constrained to maintain transparency as a light transducing tissue. Thus, vascular density in the light path of incoming photons is minimized while simultaneously maintaining optimal retinal perfusion. To cope with such constraints, the retina has evolved a dual blood supply, ensuring adequate perfusion capacity while maintaining a relatively low vascular density in the optical path of incoming photons, as depicted in Figure 1.1 [23]. Lying outside of

the light path, the choriocapillaris is a high flow, low arteriovenous ΔpO_2 system found dorsal to the retinal pigment epithelium, supplying the outer one third of the retina. In contrast, the inner two-thirds of the retina is perfused by a series of vascular plexuses characterized by low flow and high arteriovenous ΔpO_2 [24]. These characteristics suggest that the metabolic demands of the inner retina are matched by a perfusion system operating near maximal capacity whereas perfusion through the choriocapillaris maintains a high excess capacity for oxygen delivery to the outer retina.

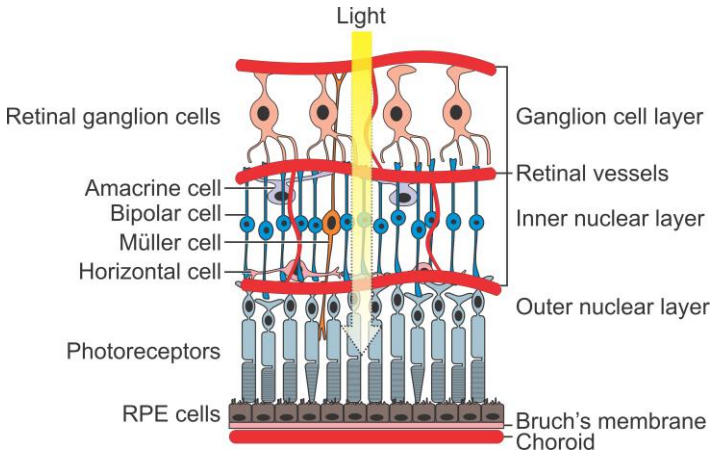

Figure 1.1. Schematic of the neuroretina and vascular supply. Select retinal layers (outer nuclear, inner nuclear, ganglion cell layers) and accompanying dual vascular supplies (choroid, retinal vessels) are depicted on the right. Cell types are shown on the left. The path of an incoming photon is depicted as a yellow arrow (light). RPE = retinal pigment epithelial.

Exchange between the blood and retina is tightly regulated at both vascular supplies, giving rise to two distinct blood-retinal barriers (BRB). The cellular components of the outer barrier include the retinal pigment epithelial (RPE) cells whereas the cellular components of the inner barrier include epithelial cells and pericytes. Diabetes-induced changes to these components are well described in the literature, however, the cells comprising the inner BRB, retinal endothelial cells and pericytes, have received considerable attention. Indeed, endothelial cell apoptosis, pericyte dropout and formation of acellular capillaries are the hallmark histopathological changes associated with DR whereas retinal vascular permeability is frequently used as an end point to study disease progression in animal models [25].

Though classically assumed to be a vascular disease, diabetes affects all cells of the retina including the neural and glial cells as well as pericytes, endothelial and epithelial cells. In fact, the hemodynamics of the choroidal and inner retinal vascular supplies (see above) suggest that the inner retinal metabolic demand is met with a sparse vascular supply operating near maximum capacity resulting in a high sensitivity to metabolic or hypoxic insults [23]. Indeed, neurodegeneration in post-mortem diabetic eyes without evidence of vascular lesions suggests this to be an early event in DR [26]. The diabetes-induced neuroretinal changes include increased apoptotic marker expression and glial cell activation in the diabetic retina [26–28]. Increased rates of apoptosis have been reported in the inner plexiform and inner nuclear layers of diabetic rats [29] moreover, ganglion cell apoptosis with associated thinning of the nerve fiber layer are consistently observed across rodent models of diabetes [27,30]. Though vascular dysfunction has been the center of focus in DR research, technological advancements have paved the way to unraveling the complex interplay between the vascular- and neuro-retina [25,31].

1.4 Molecular Mechanisms

The molecular events leading to DR progression are complex and varied; however, it is now appreciated that DR is the product of hyperglycemia, dyslipidemia, and chronic inflammation [17,22,31]. In fact, key *in vitro* studies have shown that retinal endothelial cells generate reactive oxygen species (ROS) and activate inflammatory and apoptotic pathways in response to cytokine stimulation rather than hyperglycemia [32]. These key findings argue for vascular injury resulting from a glucose-induced cytokine release attributed to neighboring cells rather than a direct glucose effect on retinal endothelial cells.

1.4.1 Hyperglycemia

In cells which cannot downregulate glucose uptake, hyperglycemia is thought to increase glucose-related biochemical pathway flux leading to changes in cellular function [33]. Indeed, increased polyol pathway flux depletes cytosolic NADPH and glutathione, predisposing cells to oxidative stress [34]. Hyperglycemia

also favors the non-enzymatic glycation of proteins which can be irreversibly modified to yield advanced glycation end products (AGE). As AGE are formed irreversibly, long-lived proteins are particularly vulnerable to accruing a significant population of AGE modified proteins, resulting in changes to protein structure and function [35]. Additionally, AGE bind to receptors of AGE (RAGE) leading to expression of pro-inflammatory and pro-angiogenic genes [36], an effect that is seen in diabetes-induced diacylglycerol accumulation and protein kinase C activation [37]. Importantly, a unifying mechanism has been proposed to explain the disparate observations of hyperglycemia-induced cellular damage [33]. Observations of ROS emission from mitochondria at a high proton motive force suggest that hyperglycemia induces flux through oxidative phosphorylation resulting in increased proton motive force, ROS release, inhibition of glyceraldehyde-3-phosphate dehydrogenase (GAPDH) and glycolysis further favoring glucose flux through collateral pathways [33,38]. Though hyperglycemia remains the key factor in DM complication rates, other factors are implicated in DR progression and are described below.

1.4.2 Dyslipidemia

Diabetic dyslipidemia refers to changes in local and systemic metabolism of a diverse array of lipid classes including plasma triglycerides, cholesterol, and lipoproteins [16]. Plasma lipid and lipoprotein levels and composition are dramatically altered in diabetes [39] and disease severity is associated with serum lipid markers [40,41]. Retinal specific lipid metabolism leads to a unique fatty acid profile which is significantly altered in diabetes, suggesting that local retinal lipid metabolism plays a key role in DR progression [42–44]. The next section will focus on sphingolipid changes in diabetic retinopathy.

1.4.3 Sphingolipids and Ceramide

Sphingolipids are a diverse class of bioactive lipids subserving a variety of cellular functions such as cell growth, proliferation, apoptosis, inflammation and others [45]. Ceramides are the central sphingolipid species, serving as an intersection between major sphingolipid metabolic pathways. The diversity of the

sphingolipidome can be rationalized by considering the availability of multiple modification sites to the chemical structure of ceramides, as shown in Figure 1.2A [45]. Ceramides contain two fatty acids which vary in their chain lengths providing for several degrees of freedom in modulating ceramide biological and physicochemical properties [43]. Additionally, the 4-5 trans double bond can be reduced to yield dihydroceramide whereas modification of the 1-hydroxyl position with various head groups yields ceramide-1-phosphate, sphingomyelin, or glycosylated ceramides [46].

Ceramide is the central hub of sphingolipid metabolism, connecting all sphingolipid metabolic pathways, allowing the interconversion of distinct sphingolipid species (Figure 1.2B) [47]. Total sphingolipid pools are controlled by the relative influx of free fatty acids versus their efflux from the sphingolipid metabolic network. Cellular free fatty acids are incorporated into the sphingolipid metabolic network by condensation with serine to give, in the case that the fatty acid is palmitate, 3-ketodihydrosphingosine which is subsequently converted to ceramide in the *de novo* synthesis pathway [45]. Fatty acid efflux from the sphingolipid pool, on the other hand, is through sphingosine-1-phosphate (S1P) hydrolysis by S1P lyase, yielding a fatty aldehyde which can be oxidized to a free fatty acid [45].

The interconversion of distinct sphingolipid species through ceramide suggests that it is the relative ratios of sphingolipid species which determine the final biological response. This feature of sphingolipid metabolism led to the term “sphingolipid rheostat” to describe the control over cell fate by the ratio of ceramide, a pro-apoptotic lipid, to sphingosine-1-phosphate, a pro-survival signal [48,49]. Ceramides are generated *de novo* or by interconversion from other sphingolipid species.

A major source of ceramide generation during cellular stress responses is the sphingomyelinase-catalyzed hydrolysis of sphingomyelin (SM) to ceramide and phosphorylcholine [50]. Sphingomyelinases (SMases) are a group of proteins differentiated by the pH optima at which they demonstrate maximal activity, referred to as acidic, neutral, and alkaline SMases.

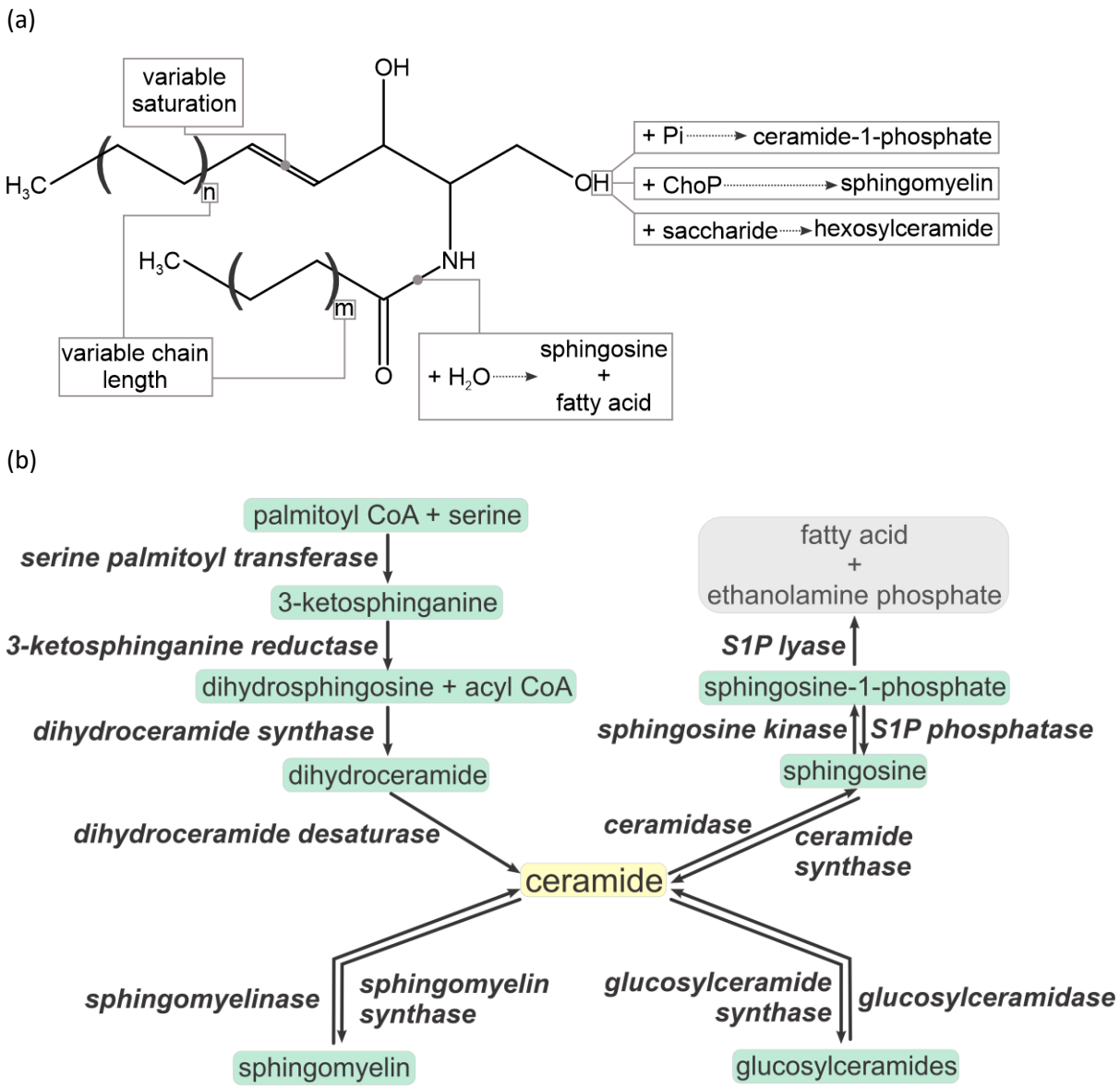

Figure 1.2. Ceramide is the central hub of sphingolipid metabolism. (a) Chemical moieties of a generic ceramide which are sites of chemical transformation yielding a diverse sphingolipidome. Pi = inorganic phosphate, ChoP = phosphorylcholine, m = number of methylene groups in the acyl chain of the exchangeable fatty acid, n = number of methylene groups in the acyl chain of the sphingoid base, m may or may not equal n. (b) Sphingolipid metabolic network (green). Ceramide (yellow) provides the link for interconversion of sphingolipid species whereas control over total sphingolipid pools is provided by free fatty acid influx at serine palmitoyl transferase and efflux (grey) at sphingosine-1-phosphate (S1P) lyase.

Alkaline sphingomyelinase has restricted expression in humans, whereas acid and neutral SMases are ubiquitous [16]. Acid SMase (ASMase) has received much attention for its role in the etiology of Neimann-

Pick disease type A, a lysosomal storage disorder where infants present with hepatosplenomegaly, central nervous system involvement, and rarely survive past 2-3 years of age [51]. Generation of ASMase knockout mouse models led to the observation that ASMase deficiency provided significant protection from a host of apoptotic stressors such as hypoxia, ischemia-reperfusion, and radiation [52]. In fact, cells derived from Niemann-Pick patients show significant resistance to ionizing radiation-induced apoptosis [53].

These observations suggest that ASMase-dependent ceramide generation plays a fundamental role in cellular responses to stressors, such as those encountered in the diabetic retina (see above). Consistent with this, the Busik lab has demonstrated protection from retinal ischemia-reperfusion injury in an ASM knockout mouse model compared to wild type controls [54]. Other work in the same laboratory demonstrated that the retina expresses both neutral and acidic SMases; however, only ASMase upregulation was observed in ischemia reperfusion injured eyes [54].

Immunoblotting for ASMase protein content in cell culture revealed high expression levels in human retinal endothelial cells with smaller but detectable levels in human retinal pigment epithelial and Müller cells. Correspondingly, ASMase enzyme activity was highest in retinal endothelial cells and retinal pigment epithelial cells, with lower levels detected in human Müller cells [54]. Activation of ASMase by cytokine treatment results in pro-inflammatory signaling whereas its inhibition leads to reduced inflammatory gene expression in human retinal endothelial cells [55]. These results support a central role for ASMase-dependent ceramide generation in the increased apoptosis rates characteristic of DR.

1.4.4 Downstream Effects of Ceramide Accumulation

Cellular ceramide accumulation is a well-accepted and ubiquitous feature of apoptosis. Though many mechanisms have been proposed to explain the effects of ceramide in the cell, the exact mechanism by which ceramide exerts its biological effects are not known. These effects, furthermore, are likely to involve

several parallel effects at distinct sites in the cell depending on the physiological context of each system [56]. Ceramide was once thought to serve as second messenger but is now known to have significant physicochemical effects on biological membranes as well [53,56]. Accumulation of ceramide stiffens membranes, playing a key role in generation of lipid rafts for cell signaling, vesicle budding/fusion, and cell migration [56,57]. Here the focus will be on the role of mitochondrial ceramide accumulation in apoptotic cells.

1.4.5 Mitochondrial Ceramide

Mitochondrial structure and function changes are thought to play an early and central role in DR onset and progression. Diabetes-induced changes to mitochondrial structure and function have been demonstrated using *in vivo* and *in vitro* DR models [58–62]. Furthermore, hyperglycemia-induced ROS production has been proposed as a unifying mechanism to explain the disparate biochemical derangements evident in the hyperglycemic retina and retinal cells [33,58]. While descriptions of diabetes-induced mitochondrial ceramide changes in retinal cells are lacking (see Chapter 3), mitochondria are known to contain several classes of sphingolipids, including sphingomyelin (SM) and ceramide, as well as enzymes of sphingolipid metabolism [63]. Mitochondrial ceramide accumulates secondary to cytotoxic stressors such as cytokines, UV radiation, and ischemia-reperfusion injury via *de novo* and SMase-dependent pathways. Whereas exposure of neutrophils to bacterial toxins or UV irradiation of HeLa cells each result in mitochondrial ceramide accumulation in a sphingomyelinase-dependent manner, similar changes in mouse brain after ischemia reperfusion injury are instead attributed to *de novo* synthesis [64–66]. Interestingly, over expression of a mitochondrially-targeted bacterial SMase in MCF7 breast cancer cells resulted in apoptosis whereas expression in other cellular compartments had no effect, suggesting that *in situ* SMase-dependent mitochondrial ceramide accumulation plays an essential role in cellular apoptosis [67].

The effects of mitochondrial ceramide generation depend on the specific site of generation as its poor water solubility prevents spontaneous intermembrane transfer [63]. In the mitochondrial outer membrane, ceramides are thought to facilitate formation of pores resulting in release of proapoptotic cytochrome *c* [68–72]. Whether ceramide spontaneously forms membrane channels or instead interacts with pro- or anti-apoptotic Bcl-2 family proteins is still an open question. In the inner mitochondrial membrane, ceramide inhibits respiratory complexes, favoring ROS generation and oxidative stress-induced apoptosis [63,73]. It is noteworthy that these effects are not mutually exclusive. Because ROS generation is a common early feature of cells exposed to apoptotic stimuli whereas outer membrane permeabilization initiates the execution of apoptosis, the levels of mitochondrial ceramide may fluctuate in a time- and pathway-dependent manner.

1.5 Purpose and Scope

The critical role of ASMase-dependent ceramide generation in retinal cell damage in DR and the mounting evidence of mitochondrially targeted ceramide as a control point over cell fate provides the motivation for this work. Functional characterizations of retinal bioenergetic changes are conspicuously missing in the literature due to lack of available comprehensive and flexible methodology. To address this need, the development of a novel 3D printed microrespirometer is described in Chapter 3. Chapter 4 provides descriptions of diabetes-induced, ASMase-dependent mitochondrial ceramide accumulation in retinal pigment epithelial cells and the functional consequences thereof. The next chapter provides a description of respirometry and a framework for its use as a screening platform or as a tool to study oxidative metabolism in finer mechanistic detail.

Chapter 2: Bioenergetics Studies by Respirometry

2.1 Bioenergetics Background

Bioenergetics is the study of biological energy transduction, describing how biological oxidation of partially oxidized hydrocarbons (e.g. carbohydrates from food) is efficiently coupled to ATP generation through electrochemical cellular machinery. The bulk of this machinery resides within the mitochondria, semi-autonomous cellular organelles thought to have originated from the endocytosis and retention of a free-living prokaryote by a eukaryote owing to a symbiotic relationship between the entities [74].

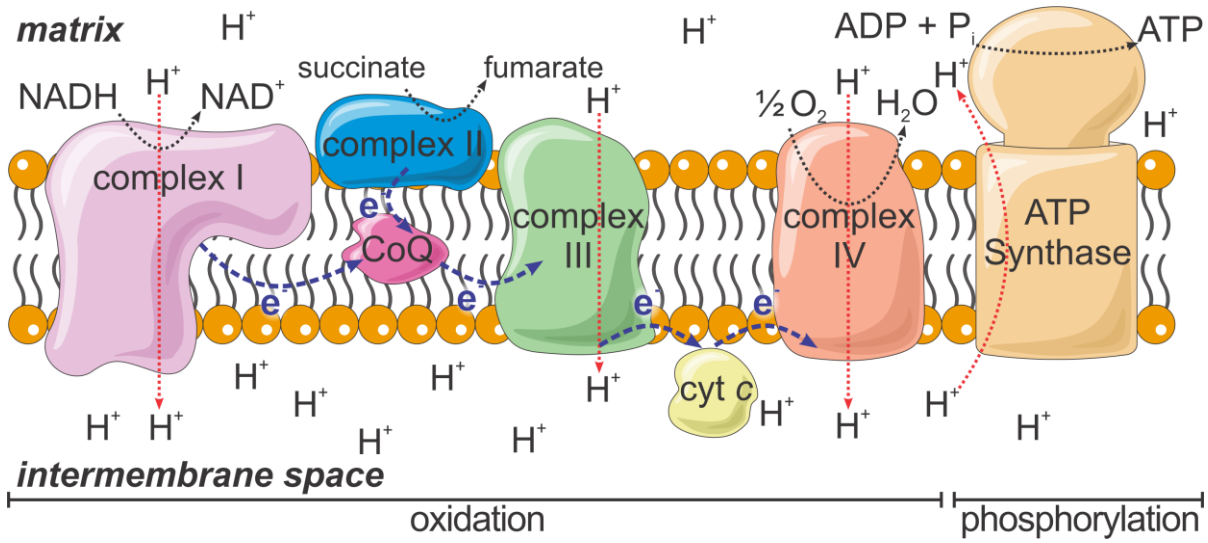

Figure 2.1. Schematic representation of oxidative phosphorylation machinery. Oxidation of electron carriers by the ETC is coupled to proton extrusion (red arrows) from the mitochondrial matrix and generation of a proton motive force (pmf). Phosphorylation, driven by proton ingress, yields ATP.

Mitochondria are double bilayered cellular organelles and house the necessary machinery for efficient pathways of biological energy transduction. Modern day understanding of the physicochemical mechanisms of mitochondrial energy transduction originates with Mitchell's Chemiosmotic theory, a conceptual framework which earned Peter Mitchell the Nobel Prize for Chemistry in 1978 [75]. The Chemiosmotic theory posits that the coupling of ADP phosphorylation with that of the oxidation reactions occurs through generation of a proton gradient across the impermeable inner mitochondrial membrane,

as depicted in Figure 2.1 [76]. In this conceptual framework, electron carriers (NADH, $FADH_2$, CoQ, and cyt *c*), reduced through cellular catabolic processes, are oxidized in the electron transport chain (ETC) resulting in extrusion of protons to the intermembrane space side of the mitochondrial inner membrane (oxidation). Turnover of the ETC, therefore, establishes a proton motive force (pmf) which is used for ATP synthesis (phosphorylation). The electrochemical gradient induced by the pmf provides the free energy necessary not only for ATP synthesis, but also the transport of a variety of charged species undergoing electrogenic exchange at the impermeable inner mitochondrial membrane [77]. Terminal reduction of oxygen occurs at complex IV of the inner mitochondrial membrane. This site serves as a sink for reducing equivalents and oxygen, providing the driving force for the respiratory cascade and forming the basis of using respirometry to study biological energy transduction [78,79].

The coupling of oxidative phosphorylation through the pmf, as well as the reliance of substrate oxidation on mitochondrial and extra-mitochondrial processes, allows for interrogation of a range of functional segments of cellular metabolism by monitoring respiratory flux [80–82]. Classically, the mainstay of *in vitro* bioenergetics research is carried out by monitoring the consumption of oxygen by whole tissue, cells or organelle preparations [83]. The instruments used for these studies are respirometers and they provide the continuous monitoring of oxygen concentration needed to derive the rates of oxygen consumption by biological samples. A description of respirometry instrumentation and its application to biological systems follows.

2.2 Respirometer Evolution

2.2.1 Warburg Manometer

Some of the earliest methods for measuring oxygen consumption are attributed to manometric methods, such as used by Otto Warburg to study the metabolism of healthy and tumor tissue leading to the discovery of the Warburg Effect [84]. An illustrated schematic of a Warburg Manometer is depicted in

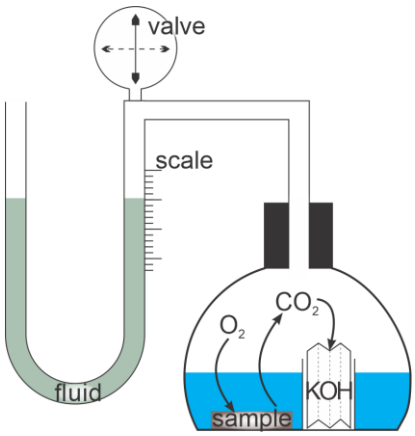

Figure 2.2. Constant volume (Warburg) manometer. A respiring sample is maintained in a sealed flask connected to a manometric U shaped tube filled with an appropriate manometric fluid. A valve positioned between the sample and manometer opened (vertical, solid line) between trials to equilibrate the buffer and headspace with the atmosphere and is closed (horizontal, dashed line) during respirometry. As the biological sample metabolizes available carbon sources, the headspace above the sample is depleted of oxygen and enriched in carbon dioxide. The headspace is scrubbed free of emitted CO_2 by a potassium hydroxide-soaked tissue paper. The graduated scale quantifies the decrease in gas volume due to uptake of O_2 by the biological sample.

Figure 2.2. The core operating principal of the Warburg constant volume manometer relies on measuring the changes in headspace gas pressure produced by a respiring biological sample in a sealed chamber. Oxidative metabolism results in consumption of O_2 and production of CO_2 [85]. If uncompensated, the CO_2 production abrogates the loss of gas pressure due to O_2 depletion. Therefore, a potassium hydroxide-soaked tissue paper is included in the sealed vessel to scrub CO_2. By removing the emitted CO_2, headspace gas pressure changes are attributed entirely to changes in the partial pressure of O_2. As the total gas in the headspace of the respirometer decreases due to O_2 consumption and CO_2 scrubbing, the height of the manometric fluid in the sample arm of the U shaped tube rises due to the pressure differential between the sample headspace and the atmosphere. A graduated scale on the sample arm of the manometer is used to read the changes in gas volume directly. Measuring the change of O_2 as a function of time provides the requisite raw data necessary to calculate the rate of oxygen uptake by the biological material. Despite the crude methodology by modern standards, manometric methods such as those used by Warburg were precise, accurate, temperature controlled, parallelized for efficiency, and modified to measure both

oxygen consumption and carbon dioxide release by thin tissue slices *in vitro* [84,86]. These and similar instruments allowed the study of whole animal or tissue metabolism well before the cellular, molecular, and biochemical underpinnings of metabolic processes were described. The Warburg manometer, however, suffered from several drawbacks which limited its usefulness for bioenergetics in the decades to come. The time resolution of the instrument is poor as changes in headspace gas depend on the respiratory rate of the sample and conditions of the assay, as well as the volume of the apparatus, and usually require long times between data sampling to accurately resolve headspace pressure differences. Sampling rates, therefore, fell well short of the ~1 Hz easily attainable by modern standards and detailed studies of metabolic changes on short times scales would prove technically challenging [81,87,88]. Additionally, the instrument required a fair amount of technical knowledge and constant attention to operate, making data acquisition slow and difficult.

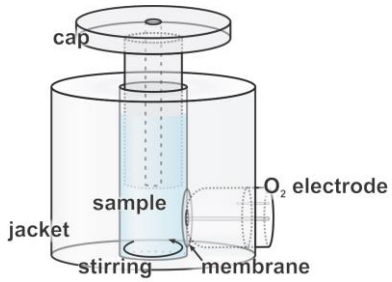

Figure 2.3. Schematic of a Clark-type electrode respirometer. Sample chamber is separated from the Clark-type electrode by a semi-permeable membrane permitting oxygen diffusion. Continuous stirring is typically provided by a magnetic stir bar and the jacket provides thermoregulation of the sample. The cap is used to partition the sample from atmospheric oxygen and an injection port is typically

2.2.2 Clark-Type Electrode Respirometer

The next technical breakthrough in respirometer design occurred with the advent of gas analyzers. The most relevant to this work is the Clark electrode, named after its inventor, Leland Clark, as first described in the 1950's [83]. Whereas manometric methods relied on inferring changes in partial pressures or volumes of the gaseous analytes by monitoring headspace gas properties, electrochemical detection permitted direct measurement of dissolved oxygen in the aqueous phase [83][89]. This fundamental shift

to directly measuring oxygen content in biological fluids represents the origin of biosensors and has withstood the test of time as it remains a popular instrument for metabolic studies until today [90]. Modern day respirometers make use of advances in manufacturing, electronics, and materials science but retain the same fundamental detection method and overall design elements as the original Clark-type electrode respirometers [80,91]. A schematic of a generic Clark-type electrode respirometer is shown in Figure 2.3. The electrode component is made of a platinum cathode and a silver anode, separated from the sample by an oxygen permeable membrane. The opposing face of the membrane is in contact with the sample in the sample chamber. Maintenance of the cathode at -0.6 V produces the following chemistry on the cathode surface:

$$O_2 + 4\,H^+ + 4\,e^- \rightarrow 2\,H_2O$$

Reduction of oxygen on the cathode results in a current that is proportional to the [O_2] in the sample if several conditions are satisfied. First, the requisite consumption of oxygen at the electrode surface induces concentration gradients which drive oxygen flux from the sample to the surface of the electrode. The greatest impedance to oxygen diffusion lies at the semipermeable membrane, which is required to prevent fouling of the electrode surface by biological fluids and must be carefully chosen to retain sufficient response times and signal stabilities of the electrode. In fact, Clark tested several candidate membrane materials including cellophane, dialysis membrane and condoms, showing that the response time and stability of the electrode depended strongly on the composition and thickness of the selected membrane [83]. Modern day instruments use highly optimized materials and film properties to ensure responsive, accurate and stable signals [81]. Next, to relate the current generated at the cathode to the bulk [O_2], Clark-type electrode respirometers require a stirred sample volume to eliminate significant oxygen gradients within the sample chamber. If left unstirred, these gradients would limit oxygen delivery to the cathode surface and the current would reflect mass transport kinetics instead of bulk [O_2]. Indeed, the landmark studies by Chance and Williams performed on isolated mitochondria used a vibrating Clark-

type electrode to achieve a similar effect allowing them to measure mitochondrial respiratory rates in a range of metabolic states and to determine ADP:O ratios [92,93]. Clark-type electrode respirometers have been the gold standard tool for bioenergetics studies for many decades and modern-day respirometers have been optimized for the unique requirements of accurate respirometry in the molecular biology revolution (see below).

2.2.3 Modern Iterations

Much like electrochemical oxygen detection fundamentally revolutionized respirometry more than six decades ago, so too are modern oxygen detection techniques and manufacturing methods paving the way for innovative designs of modern-day respirometers. The most relevant developments of the last several decades are the optode-based chemical sensors which use chemical indicators and spectroscopic methods to detect a range of analytes in a variety of environments including in the gas phase, plant soils, seawater, and biological fluids [94,95]. Oxygen optodes measure the lifetime of the excited electronic state of chemical indicators and relate changes in excited state lifetimes to oxygen content. As oxygen is particularly efficient at quenching such excited states, the lifetime of the excited state indicator is highly sensitive to the oxygen content in the sample [95]. Theoretical and practical considerations of using oxygen optodes in respirometry are described more fully below.

Key advantages to using oxygen optodes in modern day respirometers are as follows. As an optical method, optode oxygen sensors do not consume oxygen, increasing the sensitivity of the respirometer to slowly respiring samples and simplifying data analysis and interpretation compared to Clark-type electrode oxygen detection [95]. Furthermore, optodes have the unique advantage that the sensor thin film need not be physically accessible to the experimenter. As an optical technique, the detection instrumentation needs only an optically clear path to the thin film sensor, allowing for the design of sample chambers with minimal connections to potential sinks or sources of oxygen such as the ambient

atmosphere. These properties make oxygen optodes popular in microfluidic applications, where oxygen sensors are incorporated into hypoxia incubators [96–98] as well as respirometer-like devices [88,99–104].

Microfluidic respirometers have the potential to offer the flexibility and sensitivity necessary for adaptation into standard laboratory practice; however, few examples exist and will be summarized here. Kelbauskas and colleagues developed a two-component microchamber device incorporating phosphorescent O_2 and pH optodes [101]. The device consists of two separate components, the lid, a silicon wafer including micropocket arrays containing the sensor optodes, and a separate wafer serving as a cell growth substrate. After cell attachment, the two components are aligned and the microchambers hermetically sealed using mechanical pressure. The hermetic seal was validated by showing no intrachamber changes in measured [O_2] upon incubation of aerobic solutions in anaerobic environments. To further validate the hermetic seal, the group demonstrated linear oxygen concentration profiles until anoxia using respiring human esophageal epithelial cells. These results are consistent with the low apparent K_m of complex IV for oxygen and minimal oxygen diffusion into the microchambers [81,101]. Non-negligible oxygen back diffusion (discussed below) would manifest as loss of the expected linearity of the oxygen concentration profile due to the dependence of back diffusion on the sample chamber oxygen content [87,88]. While this device focuses on multiplexing biosensors in a static microchamber, the small sample demand (<100 cells) and microliter volume scales can justify the microfluidic classification despite the lack of fluidic handling provisions. Importantly, this work shows that microchambers, housing < 100 cells, can be hermetically sealed rendering them impermeable to gas exchange with the atmosphere, a requisite for accurate respirometry.

Using a similar approach, Pham and colleagues developed microchambers for single mitochondrion respirometry [99]. Employing photolithography and wet etching of oxygen impermeable glass wafers, they fabricated arrays of microwells into which oxygen optodes were deposited. A lid, manufactured from

polydimethylsiloxane (PDMS) and coated with Viton rubber to act as oxygen barrier, was compressed against the microwell array with a piston to form the microchamber. The microchambers were hermetically sealed as oxygen readings were insensitive to alternating room air (21% O_2) with 100% O_2 gas after coating with Viton. Loading of mitochondria into the wells was stochastic and no attempts at deterministic patterning were made. Nevertheless, the authors reported detection of mitochondrial-dependent respiration, which was sensitive to the uncoupler carbonyl cyanide m-chlorophenylhydrazone (CCCP). Though a higher respiratory rate was observed in wells containing two mitochondria compared to wells containing one mitochondrion, the upper and lower limits of detection and non-mitochondrial apparent oxygen consumption were not reported [99].

Kondrashina and colleagues reported on the adaptation of commercially available microfluidic slides (μ-slides) as microrespirometers by measuring oxygen consumption using soluble fluorescent O_2 sensors [88]. In this paradigm, the group detected oxygen consumption from 30,000 cells and further demonstrated that the apparent oxygen consumption was appropriately sensitive to mitochondrially targeted drugs such as uncouplers and electron transport chain inhibitors. Despite the ease of use exhibited by this system, the authors noted that oxygen back diffusion through the polymer of the μ-slide was significant as even the maximum cell density (90,000 cells per slide) failed to deoxygenate the microchannel. Nevertheless, the adapted μ-slides allowed repetitive assessment of respiratory rates by perfusion of fresh media at regular intervals [88].

Prefabricated and sealed microfluidic chips require injection of cell suspensions and subsequent incubation to facilitate attachment and spreading, a process working on the order of minutes to hours. To facilitate maintenance of buffering power and normoxia of the media, while minimizing water loss during the cell attachment phase, such devices utilize polymers with high CO_2, O_2 and, preferably, low H_2O permeabilities or solubilities. These requirements are in direct opposition to accurate respirometry, discussed below, but, importantly, may be remediated by use of surface coatings for high permeability

polymers [105]. Due to the mutual exclusivity of barrier property requirements for cell culture and accurate respirometry, strategies aimed at allowing standard cell culture methods with transient microchamber or microchannel formation are highly desirable. These approaches are described below and in Chapter 3.

The most widely adapted respirometer across a range of biomedical disciplines has no doubt become the SeaHorse Bioscience Extracellular Flux Analyzer [87,106,107]. The extracellular flux analyzer uses a standard 24- or 96-well format with a sensor cartridge equipped with fluorescent probes sensitive to O_2 and pH [106]. The sensor cartridge is lowered to within ~200 μm of the well bottom, creating a microchamber on the order of ~7 μL total volume [87,106]. Formation of transient microchambers using an actuated lid allows for seeding, culturing and manipulation of cell samples using standard laboratory techniques and conditions whereas the small effective chamber volume during measurement provides high respirometer sensitivities, detecting respiratory activity of 1 – 10 μg mitochondrial protein per well or ~10^5 cells [87,106]. The lid actuating mechanism is further employed to permit repetitive probing of organelle or cell samples by raising and lowering the cartridge to allow mixing of the small probed volume with the bulk media in the well [106]. Sample titrations, to mimic classic titration-based bioenergetics assays, are afforded by inclusion of four reagent delivery chambers which are loaded with appropriate stock solutions prior to measurement and programmatically controlled to deliver the reagents during the assay [106]. The enhanced sensitivity afforded by drastically reduced chamber volumes, high throughput nature of microplate-based assays coupled with multiplexed sensing and the high compatibility with standard cell culture techniques has resulted in widespread adoption of routine bioenergetic characterizations of systems which have been difficult to study with less sensitive or lower throughput methodology [108]. Despite the substantial improvement in methodology, there is significant oxygen back diffusion into the microchamber which limits the sensitivity of the raw measurement and is corrected with a kinetic modelling scheme [87]. Furthermore, the microplate-based method requires adherence of

samples to the well, therefore cells or organelles in suspension must be immobilized prior to measurements. Finally, experimental protocols are limited to a maximum of four reagent additions per experiment, requiring preliminary experiments to determine optimum assay conditions as well as inclusion of several assay repetitions to fully characterize biological systems of interest [106].

The molecular biology revolution of the life sciences has brought novel demands upon the bioenergetics field. Modern day microrespirometers clearly have the potential to retain the properties of current large volume apparatuses. Adoption of modern-day engineering breakthroughs will yield simple, low-cost, accurate, and flexible microrespirometers to afford routine bioenergetic characterization of physiologically relevant model systems.

2.3 Microrespirometer Design Elements

Respirometry involves continuous real-time detection of oxygen content of a given sample. The time-dependent oxygen concentration changes are then used to characterize the functional state of a given biological sample. Engineered features and data analysis strategies are developed to ensure accurate assignment of respiratory rates to functional metabolic states. As an illustrative example, consider measurement of substrate-supported whole cell respiration. The apparent oxygen consumption rate, defined here as the negative of the oxygen disappearance rate, is the sum of the rates of all processes affecting oxygen concentration in the bulk sample, summarized as:

$$R_{app} = \sum R_i = R_{sample} + R_{el} + R_{diff}$$

Where R_{sample} is the portion of the rate attributed to the biological sample, R_{el} is the portion attributed to the electrode and R_{diff} is a generic term to describe mass transfer with any potential sinks or sources of oxygen such as the walls of the container, stir bars, and sites of interaction with the ambient atmosphere. Extraction of R_{sample} from R_{app} requires knowledge of R_{el} and R_{diff}, by direct intra-experiment measurement

or *a priori* characterization. The rate of oxygen consumption at the electrode and that of diffusive processes are both dependent on the oxygen content of the sample. This non-linearity requires complex modeling to offer accurate corrections [87]. Instead, engineering solutions can minimize the contribution of these terms thus providing for accurate and straightforward data analysis and interpretation.

These engineering elements are incorporated into the Oroboros O2k oxygraph, which utilizes an optimized Clark-type electrode and large sample chamber volumes to produce stable, accurate currents with small but non-zero R_{el}. These significant improvements yield a large volume respirometer with high resolution of both oxygen concentrations and oxygen consumption rates [109,110]. Further design improvements include careful material selection to minimize potential oxygen sources (R_{diff}) by using low O_2 solubility/permeability materials for sample chamber construction [80,110]. The result of such optimizations yields a large volume respirometer (~2 mL) capable of measuring respiratory activity of less than 1 million fibroblasts or endothelial cells [80]. The high resolution and high dynamic range permit accurate assessments of oxidative metabolism at the low oxygen concentrations typical of physiologically relevant systems [79,110,111]. As with all Clark-type electrode respirometers, the requisite stirring of the chamber contents provides a technical challenge to measuring natively adherent samples.

It stands to reason that similar design elements, if incorporated into a microfluidic system, can effectively yield a useful microrespirometer offering orders of magnitude increases in sensitivity with enhanced flexibility for experimental design using flow-through configurations. Approaches to implementing the two fundamental elements of a microfluidic respirometer, microchannel formation and analyte detection methods, are described below.

2.4 Microchannel Formation

Formation of microchannels is the basis for development and manufacture of microfluidic devices. Though many techniques are available, the dominant form of microchannel formation remains casting

polymethylsiloxane (PDMS) on photolithographic molds due to the ease of producing micron-scale features and capacity of PDMS to form strong bonds to glass [112]. Despite the relative ease-of-use, there are several key drawbacks. First, PDMS has high permeability and solubility to water and gases and, furthermore, shows high rates of adsorption of hydrophobic reagents [96]. Additionally, while soft lithography is a powerful tool for embossing surface structures in PDMS, fabrication of three-dimensional geometries is much more complex. Finally, fabrication requires technical knowledge and specialized facilities, creating a high barrier to entry by non-specialists [96].

3D printing has emerged as a viable alternative to standard micromanufacturing techniques owing to its rapid rise in popularity and technical innovations [113]. Additive manufacturing, or 3D printing, was described in the 1980's as a manufacturing technique to complement traditional, subtractive, methods [114]. 3D printing differs from traditional methods in that parts are formed by successive layer addition, hence additive, as opposed to removal of stock material by milling, drilling, or cutting to form the final part. The mechanism of formation of each layer varies from fused deposition modeling, where a continuous plastic filament is heated and extruded onto a build plate, to laser-stereolithography, where layers are successively photopolymerized from a liquid resin with a computer guided light source [114]. Resolution of 3D printers, while anisotropic, has reached the micron scale, and 3D printed microfluidic devices are becoming popular owing to the complex geometries and lower barrier to entry afforded by the wide array of available 3D printing materials and technology [115]. Availability of materials has expanded greatly, and parts are available in a host of materials for varying applications requiring optical clarity, variable hardness or other physical specifications [115].

Importantly, the rapid expansion of polymer availabilities in recent years has led to materials with unknown chemical and biological properties [116,117]. The rapid growth in popularity of 3D printing surely predicts a great variety of material choices in the coming years, nevertheless, current work employing uncharacterized 3D printed polymers adopts strategies, such as passive polymer overcoating,

to overcome such issues [114,115,117].

Microfluidic devices are designed to incorporate provisions for monitoring specific aspects of biological samples contained within the formed microchannels. The relevant measurement for microrespirometry is real-time detection of dissolved oxygen using optode-based sensing. Theoretical and practical aspects of thin film oxygen sensors are described next.

2.5 Oxygen Sensing

Optode-based sensors are composed of three essential components, a chemical sensor, an immobilization matrix and optical excitation and detection instrumentation. Thin film sensors can be applied to a variety of surfaces and sampled using fluorescence intensity or fluorescence lifetime measurements [88,95,118,119].

2.5.1 Stern Volmer Relation

Thin film optodes operate on the principle of intermolecular collisional quenching described by the Stern Volmer relation [95,119,120]. The following is a brief description of the underlying physicochemical processes which lay the foundation for the development of thin film biosensors.

Consider a chemical species (A) which can absorb a photon to yield its excited state (A*). Relaxation to the ground state can be represented by the following system of equations:

$$A^* \rightarrow A + h\nu \qquad (1)$$

$$A^* \rightarrow A \qquad (2)$$

$$A^* + Q \rightarrow A + Q^* \qquad (3)$$

Where (1) represents fluorescence or phosphorescence, (2) represents radiation-less decay and (3) represents bimolecular collisional quenching of A* by the quencher, Q. We can consider the time-

dependent excited state decay behavior by assuming a pulse of photons producing a population of excited state molecules ($[A^*]_0$) in the presence of excess Q at t = 0. The decay of [A*] can be described kinetically as:

$$\frac{d[A^*]}{dt} = -k_1[A^*] - k_2[A^*] - k_q[Q][A^*] \quad (4)$$

Assuming [Q] >> [A*], $\frac{\partial[Q]}{\partial t} \sim 0$, and [A*] = $[A^*]_0$ at t = 0, integration yields the pseudo-first order expression of the form:

$$ln\frac{[A^*]}{[A^*]_0} = -(k_1 + k_2 + k_q[Q])t \quad (5)$$

Setting $\tau \stackrel{\text{def}}{=} \frac{1}{k_1+k_2+k_q[Q]}$, we can re-arrange (5) to give:

$$[A^*] = [A^*]_0 e^{-\frac{t}{\tau}} \quad (6)$$

In equation (5), k_1 and k_2 are the unimolecular rate constants describing fluorescence and radiation-less decay respectively, k_q is the bimolecular rate constant describing collisional quenching of A* by Q, and, in equation (6), τ is the lifetime of the excited state fluorophore in the presence of Q. In the case that the system lacks a quenching species, the relaxation pathways are limited to equations (1) and (2) and the corresponding rate expression for [A*] is:

$$\frac{d[A^*]}{dt} = -k_1[A^*] - k_2[A^*] \quad (7)$$

Which is integrated analogously to (4) to give:

$$[A^*] = [A^*]_0 e^{-\frac{t}{\tau_o}} \quad (8)$$

Where k_1 and k_2 are the same constants as in (5) whereas $\tau_0 \stackrel{\text{def}}{=} \frac{1}{k_1+k_2}$, is the excited state lifetime in the absence of quencher. The ratio:

$$\frac{\tau_0}{\tau} = \frac{k_1 + k_2 + k_q[Q]}{k_1 + k_2} \quad (9)$$

Can be rearranged, to yield the Stern-Volmer relation:

$$\frac{\tau_0}{\tau} = 1 + \tau_0 k_q[Q] \quad (10)$$

Plotting $\frac{\tau_0}{\tau}$ as a function of [Q] reveals a line with slope = $\tau_0 k_q$, from which the bimolecular rate constant can be extracted.

2.5.2 Application to Biosensors

The use of excited state quenching to construct oxygen biosensors relies on measurements of τ_0 and τ at known quencher concentrations to construct a Stern-Volmer plot which serves as the calibration for oxygen sensing. Fluorometers are required to detect the changes in excited state lifetimes as described above. For use as an oxygen biosensor, the measurement can be performed with steady-state or pulsed excitations providing intensity or lifetime information, respectively [95,119]. Though both methods are employed, lifetime measurements yield greater reproducibility for solid-state thin film sensors as they are independent of dye concentration and film thickness [95,118].

Used as biosensors, the bimolecular rate constant k_q is irrelevant and the Stern-Volmer relationship is expressed as $\frac{\tau_0}{\tau} = 1 + K_{SV}[Q]$, where K_{SV}, the Stern-Volmer quenching constant, is the fitting parameter. Lifetime measurements on unknown samples are interpolated to yield [Q], the analyte of interest. In the case of $[O_2]$ determination, τ_0 is measured by exposing the sensor to a practically feasible anaerobic solution ($[O_2]_{anaerobic} = 0$) and an identical aerobic solution of known $[O_2]_{aerobic} > 0$, typically a buffered salt solution at a defined temperature, pressure and humidity [121]. Arbitrary $[O_2]$ can be determined in unknown samples provided $[O_2]_{anaerobic} \leq [O_2] \leq [O_2]_{aerobic}$.

The Stern-Volmer relationship derived above assumes homogeneity of the fluorophore and quencher

system. While this assumption is valid for dissolved fluorophores in liquids, the case of optode-based biosensors diverges from such ideal behaviors. Optode-based thin films immobilize a fluorophore in a solid matrix and collisional quenching relies on diffusion of the quencher through the solid film. This method of entrapment produces inherent heterogeneity of the fluorophore microenvironments resulting in varying quencher accessibilities and a curvilinear Stern-Volmer plot [122]. A common model applied to describe thin-film oxygen sensors with pronounced curvature of the Stern-Volmer plot is the two-site model of the form:

$$\frac{\tau_0}{\tau} = \left(\frac{f_1}{1 + K_{SV1}[Q]} + \frac{f_2}{1 + K_{SV2}[Q]}\right)^{-1} \quad (11)$$

Where f_1 and f_2 are the fractional contributions from each site in the absence of quencher whereas K_{SV1} and K_{SV2} are the quenching constants for each site [119]. In systems with marked curvature of the Stern-Volmer plot and which require highly precise [O_2] determinations, multisite models such as (11) are of importance.

Development of an accurate, sensitive, flexible, and inexpensive respirometer allows for comprehensive examination of cell or tissue metabolism. Diverse biological systems can be studied globally, as appropriate for screening experiments, or in greater mechanistic detail. The next section will describe how respirometry can be used to screen for, and later to localize, metabolic dysfunction.

2.6 Whole Cell Respirometry

Respirometry of whole cells or tissue slices represents a physiologically relevant system for the determination of metabolic dysfunction. This relevance stems from the dependence of oxygen consumption rates on the entirety of biological substrate oxidation, depicted in Figure 2.1. A generic substrate (S_0), destined for full oxidation in mitochondria, is subject to transfer across membranes (1 and 3) and flux through metabolic pathways (2 and 4). Terminal oxidation occurs in the mitochondrial matrix

and electron transport chain (ETC) (5), housing the site of oxygen consumption. Oxidation in the ETC is coupled to generation of a proton motive force (pmf) across the inner mitochondrial membrane (5), whose discharge drives phosphorylation of ADP at ATP synthase (7). The pmf can additionally be discharged through proton leak pathways without contributing to phosphorylation (6). Alternate metabolic pathways divert intermediates for storage or synthesis (S_2) depending on the physiological demands on the system. Ironically, these dependencies are also the origin of significant limitations to whole cell respirometry.

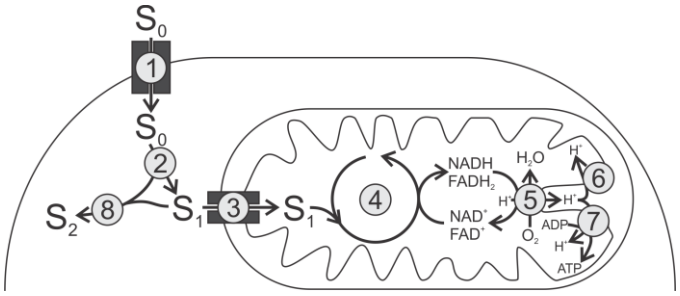

Figure 2.4. Schematic of exogenous substrate oxidation by whole cells or tissues. Exogenous substrate (S_0) traverses the plasma membrane (1) with cytosolic metabolism (2) yielding an intermediate (S_1) which is transported into the mitochondrial matrix (3). Oxidation in the mitochondrial matrix (4) produces reducing equivalents (NADH, $FADH_2$) to couple oxidation with proton translocation to generate a proton motive force (5). The proton motive force is discharged through ATP synthase to drive ADP phosphorylation (7) or through a non-productive 'leak' pathway (6). Metabolic intermediates can be shuttled into other pathways, represented as (S_2) and (8).

As control over oxygen consumption is simultaneously shared by substrate oxidation, ATP turnover, and proton leak [123,124], changes in substrate-supported (basal) respiratory activity may, at worst, show false-negatives or, at best, produce detectable changes without adequate information to localize the source. For example, release of mitochondrial cyt-ochrome c during apoptosis impairs transfer of reducing equivalents from Complex III to Complex IV of the ETC and is expected to impair basal respiratory activity. Measurement of basal respiratory rates in whole cells or tissues, however, may fail to resolve such differences [125].

Metabolic dysfunction in whole cells or tissue is therefore typically assessed using sequential titrations with membrane permeable molecules to shift control over oxygen flux to different components of cellular metabolism. A typical titration experiment yields estimates of basal respiration, proton leak supported respiration, maximum respiratory capacity, phosphorylation-linked respiration and non-mitochondrial respiration [77]. In each case described below, it will be assumed that respiratory states of a treatment group will be compared to the corresponding respiratory states in an appropriate control group.

2.6.1 Basal Respiration

Basal respiration is assessed by providing carbon sources to whole cells or tissues which mimic *in vivo* extracellular substrate availability. The basal respiratory rate is not particularly useful without an estimate of the imposed metabolic load on the system, as oxygen consumption is also under the control of ATP demand in this state. Nevertheless, providing a series of carbon sources can reveal changes in oxidation of lipids, carbohydrates, and amino acids if dysfunctions lead to substantial deficiencies in substrate delivery [77,126]. Detection of altered substrate supported respiration in one class of substrates, palmitate for example, suggests alterations to substrate oxidation pathways. The basal respiratory rate is additionally useful to estimate the proportion of respiration linked to ATP synthesis, which is calculated as the difference between basal respiration rate and the respiratory rate in the presence of an ATP synthase inhibitor [127,128]. A common substrate for whole cell respiration is glucose; however, pyruvate lactate, palmitate, and amino acids are provided as replacements or in combination [81,129,130].

2.6.2 Leak Respiration

Mitochondrial membranes are not completely impermeable to protons, and all mitochondria possess inherent proton leak ((6) in Figure 2.1) [127,131]. Assessing whole cells or tissues in the leak state involves titrating oligomycin into a respiring sample in the presence of saturating substrates. Oligomycin inhibits ATP synthase, increasing the pmf and decreasing oxygen consumption rates. The low respiratory rate

observed with optimum oligomycin concentrations is controlled by the proton leak with a component consisting of pmf discharge through electrogenic ion exchange at the inner membrane [132]. Detection of increased respiratory rates in the presence of oligomycin suggests increased permeability of the inner mitochondrial membrane to protons. Without a corresponding increase in basal respiratory activity, increased proton leak results in diminished ATP generation through oxidative phosphorylation [127].

It is important to note here that, at the molecular level, the leak proton current may be due to influx of protons to the matrix without production of ATP (proton leak) or oxidation of reducing equivalents without extrusion of protons from the matrix (proton slip). Proton leak through the inner membrane is ohmic and inhibition of ATP synthase results in slight hyperpolarization of the inner membrane, accelerating the leak current, and, in turn, the respiratory activity. Thus, oligomycin treated samples are a slight overestimate of the true proton leak. Though proton leak is thought to be the major contributor, respirometry alone cannot be used to resolve proton leak and proton slip mechanisms [131,133].

2.6.3 Maximal Respiration

Maximal respiratory rates are achieved for a given set of substrates by treatment with chemical uncouplers to dissipate the pmf, shifting control over respiration to substrate delivery and inherent turnover capacity of the ETC [77]. Maximal respiratory rates are typically attributed to the highest rates observed with uncoupler titration of oligomycin-inhibited samples. In the presence of oligomycin, however, maximal OCR is underestimated by up to 47%, an effect that is cell type dependent [134]. Accurate determination of maximal OCR in whole cells or tissues, therefore, requires uncoupler titration in the absence of oligomycin.

2.6.4 Background Oxygen Consumption Rate

Determination of the apparent respiratory rate in the presence of ETC inhibitors, such as rotenone and antimycin A, is required to accurately calculate and assign respiratory rates to metabolic states [81]. Non-mitochondrial oxygen consuming processes originate from both the biological sample and the instrumentation. Addition of inhibitors to measure background rates allows for correction of experimental data and accurate numerical assignments to respiratory states. Such measures are necessary to avoid biasing flux control ratio calculations [123].

2.6.5 Additional Experimental Considerations

Lipophilic reagents, such as oligomycin and uncouplers, must each be titrated to achieve an optimum reagent to membrane ratio and a maximum observable response. Titration accounts for variations in cell density or membrane content and ensures that a consistent respiratory state is achieved in all samples. Chemical uncouplers are particularly important to titrate as they inhibit respiration at high concentrations [111]. If experimental instrumentation limits capability to intra-experimentally titrate compounds, preliminary studies should be performed to determine optimal reagent concentrations and, importantly, sensitivity of measured parameters to changes in reagent concentration.

Raw respiratory rates reflect respiratory activity contained in the sample chamber and must be normalized to obtain cell-specific or mitochondrial-specific parameter values. Normalization of data can therefore play a significant role in dysfunction localization. Raw respiratory rates can be normalized to i) total cell or tissue mass by cell counting, weighing or assaying total protein, ii) mitochondrial content by mtDNA content, immunoblotting for markers, measuring TCA cycle enzyme activity, or iii) a reference respiratory state to serve as internal standard [123,124,135]. Employing each strategy, whether individually or in combination, aids in localizing changes to bioenergetic properties. Normalization to total sample mass or mitochondrial content can resolve mitochondrial content changes from changes to

mitochondrial-specific metabolism [127]. Normalization to a reference state is the basis for flux control analysis, a framework for analyzing steady state biochemical pathway flux [136]. Each normalization scheme offers benefits and limitations but, importantly, they need not be mutually exclusive. Flux control analysis is available with appropriate assignment of reference state, while total protein and mitochondrial markers can be estimated from a common detergent extract [137].

With these considerations in mind, information density can be increased greatly in the case of whole cell or tissue respirometry. While amenable as a screening tool, these procedures suffer from a paucity of mechanistic information. Respirometry can be used to study metabolism in finer detail, as will be described below.

2.7 Permeabilized Cell Respirometry

Detailed characterization of bioenergetic (dys)function in a disease model by respirometry requires removal of confounding factors, yielding access to mitochondria with plasma membrane impermeable reagents. Mechanistic bioenergetic characterizations have classically used suspensions of isolated mitochondria in isotonic buffers mimicking the composition of the cytosol. Indeed, much of what we know today about the fundamental mechanisms governing oxidative metabolism were discovered in isolated mitochondria [92,138]. Recently, however, the universal validity of this system has been questioned. Mitochondrial purification results in large losses to sample yield, potential enrichment or depletion of mitochondrial subpopulations, as well as changes to mitochondrial structure, thus limiting the applicability of this method in a wide range of biological systems [139,140]. In contrast, selective permeabilization of cells or tissues provides a convenient method for direct physical access to mitochondria, mimicking that of the isolated mitochondria case [80,129,141]. In this paradigm, the mitochondria remain constrained within the cytoskeletal framework whereas soluble cytosolic contents are removed by dilution into the extracellular space. Free access to the cytosol allows for use of a variety

of substrates and mitochondrial-specific reagents without the limitations imposed by plasma membrane transport and cytosolic processing.

2.7.1 Permeabilization

Selective plasma membrane permeabilization uses detergents or bacterial toxins to interact with plasma membrane cholesterol resulting in pore generation [141,142]. Mitochondrial membranes are spared owing to limited cholesterol content [141,142]. Using respirometry to monitor plasma membrane permeabilization requires assessment of plasma membrane permeability to non-permeable small molecules and quality control assessments to ensure intactness of mitochondrial membranes in the presence of permeabilizer.

The most convenient set of reagents to monitor permeabilization progress are succinate and rotenone [81,135]. As a cell permeable complex I inhibitor, rotenone will maintain low respiratory rates until the normally impermeable succinate gains access to the cellular cytosolic space to stimulate respiration through complex II. This combination provides a means to monitor both time- and concentration-dependent effects of whole cell permeabilization.

Optimal permeabilizer concentrations ensure maximal plasma membrane permeabilization without affecting the mitochondrial membranes. Mitochondrial membrane integrity is validated to ensure appropriate permeabilization conditions. Respirometric characterization of outer membrane integrity relies on detection of respiratory stimulation by addition of exogenous cytochrome *c* [135]. Stimulation of respiration by exogenous cytochrome *c* addition, preferably in the presence of saturating ADP or uncoupler, is diagnostic of outer membrane permeability. The inner membrane on the other hand can be probed by measuring a respiratory control ratio using optimal ADP and oligomycin concentrations, allowing direct comparison with known high-quality mitochondrial preparations.

It should be mentioned here that permeabilization of cells, and especially of tissues, introduces complications to experimental interpretation. First, permeabilized muscle fibers display a greater than ten-fold increase in the apparent K_m for ADP compared to isolated mitochondria from the same tissue [143]. Similar patterns are seen with oxygen affinities in permeabilized muscle fibers, showing distortions in oxygen traces about the aerobic-anaerobic transition suggesting apparent K_m for oxygen of 50 μM whereas isolated mitochondrial oxygen affinities are estimate between 0.1 – 10 μM [O_2] [81]. Finally, translation of findings from isolated mitochondria to permeabilized tissue is not always possible. This is demonstrated by failure to resolve acute changes to ADP-stimulated respiration in saponin-permeabilized liver from ground squirrels in torpor. Characterization of isolated mitochondria, however, showed the expected 60-70% decrease [144]. Finally, permeabilized myofibers from young adult and senescent rats showed modest changes to respiratory activity, hydrogen peroxide emission and mitochondrial permeability transition pore induction by calcium, whereas isolated mitochondria demonstrate greater than 50% decreases in maximum ADP-stimulated respiratory rates, with similar patterns in ROS emission and mitochondrial permeability transition pore induction by calcium [145].

In whole tissue preparations, apparent changes to binding affinities are typically attributed to long diffusion distances and, potentially, retention of diffusive barriers with retention of intracellular structures [141,143]. In cases where substrate delivery may be diffusion controlled, these restrictions are partly remediated by titrating reagents to maximum effect. This is exemplified by utilization of hyperoxia and high ADP concentrations (>2 mM) to accurately determine maximum oxidative phosphorylation turnover in permeabilized myofibers [81]. Nevertheless, cautious interpretation of certain calculated parameters, such as binding constants, from respirometry studies using permeabilized tissues is warranted.

Whether using isolated mitochondria or permeabilized cells or tissues, direct access to mitochondria provides the basis for detailed mechanistic studies to localize dysfunctional metabolic segments in a biological system of interest.

2.7.2 Localization of Dysfunctional Segments

Turnover of the ETC relies on substrate delivery and generates a proton motive force to drive ADP phosphorylation. As the ETC is the site of oxygen consumption, respirometry is well suited to studying these components of oxidative metabolism. A schematic of the functional organization of these pathways is presented in Figure 2.2. Addition of exogenous substrates into the sample medium partially reconstitutes the tricarboxylic acid (TCA) cycle, generating reducing equivalents in the form of NADH and/or $FADH_2$ which enter the ETC. Electron flow also enters the ETC through dehydrogenases which do not depend on the TCA cycle, including mitochondrial glycerol phosphate dehydrogenase (mGPDH), di-

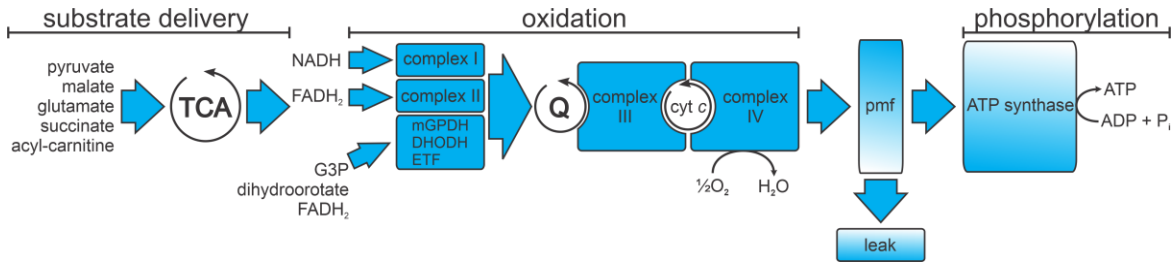

Figure 2.5. Functional organization of metabolic processes controlling respiratory activity in isolated mitochondria or permeabilized cells. Substrate delivery involves oxidation of TCA cycle intermediates to produce electron carriers such as NADH and $FADH_2$. Terminal oxidation of electron carriers occurs in the mitochondrial electron transport chain (oxidation), consuming oxygen and producing a proton motive force (pmf). Electron carriers enter the electron transport chain through a variety of enzymes and converge at the ubiquinone/ubiquinol pool (Q), driving flux through complexes III and IV. Cytochrome *c* couples oxidation of Q with reduction of oxygen at complex IV. The pmf is generated at complexes I, II, and III and dissipated through ATP synthesis (phosphorylation) or non-productive leak pathways. G3P = glycerol-3-phosphate, mGPDH = mitochondrial glycerol phosphate dehydrogenase, DHODH = dihydroorotate dehydrogenase, ETF = electron-transferring flavoprotein.

hydroorotate dehydrogenase (DHODH) and electron-transferring flavoprotein (ETF) as examples [80,146]. Electron flows converge on the ubiquinone/ubiquinol pool (Q), which is oxidized by cytochrome *c* at complex III. Cytochrome *c* then provides reducing equivalents for oxygen reduction at complex IV. Complexes I, III, and IV couple redox chemistry with proton translocation to generate a pmf which either drives ADP phosphorylation or is alternatively dissipated through non-productive leak pathways.

Respirometry can be used to study specific segments of this system to localize metabolic dysfunctions. What follows is a description of respirometry-based assays to localize dysfunctional segments of oxidative metabolism. Equivalent to the whole cell/tissue strategy described above, it is assumed that comparisons will be made to appropriate biological control samples in an identical respiratory state.

2.7.3 Leak state

Addition of saturating substrates to respiring mitochondria or permeabilized samples yields a leak state, analogous to that for whole cell/tissue preparations described above. In the presence of saturating substrates, endogenous ADP is quickly phosphorylated and, in the absence of retained ATPase activity, minimizes ATP synthase turnover, favoring pmf accumulation [141]. The high pmf decreases respiratory activity and shifts respiratory control to the proton leak through the inner membrane [77,80]. As mentioned above, contamination with ATPases presents a confounding factor as small amounts of adenylates could drive ATP synthase turnover and, in turn, artificially elevate respiratory rates in the leak state. Retention of ATPase activity in permeabilized samples is especially likely, therefore the leak state in these samples is evaluated by inhibiting ATP synthase with oligomycin in the presence of saturating substrates [141].

2.7.4 Complex I

Complex I (NADH:ubiquinone oxidoreductase) serves as an entry point for NADH generated by activation of matrix dehydrogenases. Redox chemistry is coupled to proton extrusion at complex I, thus this complex contributes to pmf generation. Reconstitution of the TCA cycle forms the basis for determining complex I-linked respiration [130]. As shown in Figure 2.3, pyruvate added with malate provides NADH and acetyl-CoA from pyruvate dehydrogenase whereas malate oxidation by malate dehydrogenase provides NADH and oxaloacetate for condensation with acetyl-CoA. Glutamate may be used with malate or added to pyruvate/malate to generate α-ketoglutarate and produce NADH through α-ketoglutarate dehydrogenase

[81,147]. Succinate accumulation is negligible due to efflux via the dicarboxylate transporter [130]. This substrate combination, therefore, results in generation of NADH but negligible $FADH_2$ thus entering the ETC predominantly through complex I [130]. The efficiency of respiration using pyruvate/malate or glutamate/malate is cell and tissue specific and preliminary experiments may be used to evaluate appropriate combinations [147]. Inclusion of saturating ADP or optimized uncoupler is required to limit control over respiratory flux by the phosphorylation system.

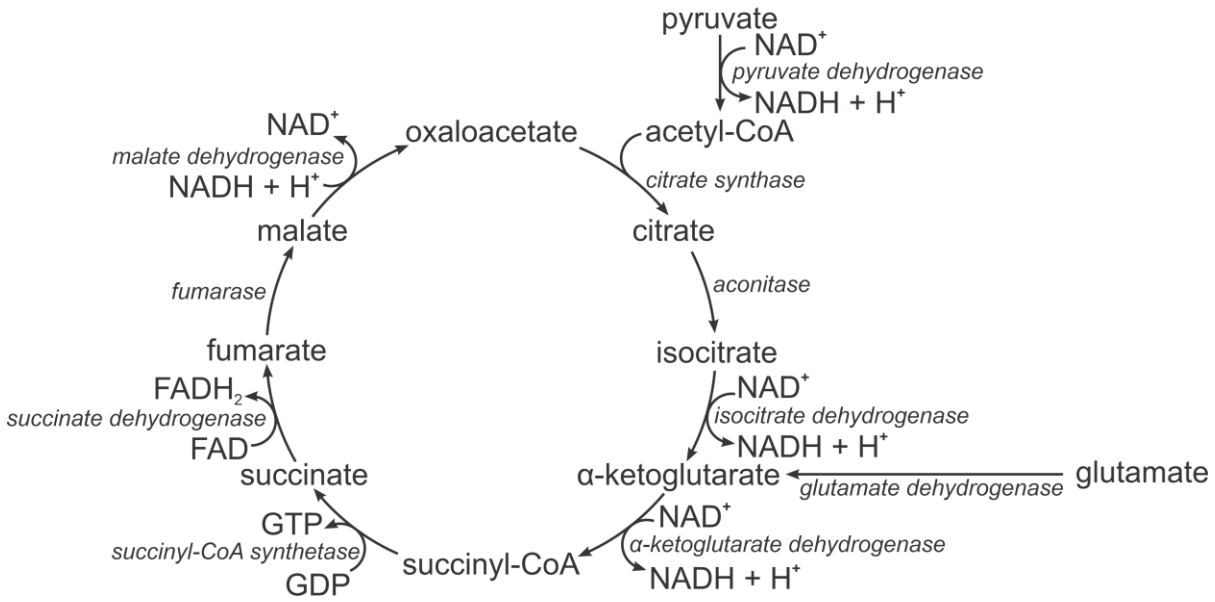

Figure 2.6. Tricarboxylic acid cycle turnover provides substrate for the electron transport chain. NADH is generated by pyruvate-, isocitrate-, α-ketoglutarate-, and malate dehydrogenases in the mitochondrial matrix. Succinate dehydrogenase (complex II) fuels ETC flux through $FADH_2$. Glutamate dehydrogenase produces NADH or NADPH. Metabolites and cofactors are shown in block lettering, enzymes displayed in italics.

2.7.5 Complex II

Complex II (succinate dehydrogenase) is at the interface of the mitochondrial ETC and TCA cycle. Using a FAD-cofactor, succinate oxidation at complex II produces fumarate for the TCA cycle and ubiquinol to drive ETC turnover but does not extrude protons to generate the pmf. Partial reconstitution of the TCA cycle with succinate results in succinate dehydrogenase-mediated $FADH_2$ generation (Figure 2.3),

therefore succinate can be added alone to support complex II-linked respiration but reverse electron transfer through complex I is eliminated by inclusion of the complex I inhibitor, rotenone [108,135,141]. As above, inclusion of ADP or uncouplers is warranted minimize flux control by the phosphorylation system.

2.7.6 Complex III

Complex III (coenzyme Q:cytochrome *c* oxidoreductase) catalyzes the oxidation of ubiquinol to ubiquinone with the concomitant reduction of cytochrome *c* (Figure 2.2). Redox chemistry at complex III is coupled to extrusion of protons to generate a pmf. Electron flux through the ETC converges at the Q-pool, and therefore, complexes III and IV present the final common path for electron flow through the ETC [79,130]. The high flux capacities of complexes III and IV are well suited to maintain high ETC turnover in the presence of convergent electron flow from mixed substrates [130,148]. This functional organization introduces artifactual control over respiratory flux by substrate delivery when using complex-specific substrates alone. Using substrate mixtures to maximize flux through complexes III and IV is discussed below; however, soluble complex III substrates, such as durohydroquinone, bypass the Q-pool and support respiratory flux directly through complexes III and IV [149]. Inclusion of malonate or rotenone, to inhibit complexes II and I respectively, favors electron flux toward molecular oxygen.

2.7.7 Complex IV

Complex IV (cytochrome *c* oxidase) is the terminal oxidase in the ETC, catalyzing the oxidation of cytochrome *c*, reduction of molecular oxygen, and proton extrusion to generate the pmf. Cytochrome *c*, the natural substrate for complex IV, cannot cross the outer membrane to supply exogenous reducing equivalents directly to complex IV in intact mitochondrial preparations. Instead, N,N,N’,N’-tetramethylphenylenediamine (TMPD) is provided in micromolar amounts in the presence of millimolar ascorbate [149]. TMPD serves as electron donor to drive complex IV turnover whereas ascorbate serves

to reduce the oxidized TMPD to maintain steady state turnover [150]. Importantly, substantial background oxygen consumption is expected from TMPD/ascorbate alone which is furthermore sensitive to temperature, pH and ionic strength of the sample media [81]. It is highly recommended that background oxygen consumption is carefully measured with this system to avoid systematic errors in data interpretation. As above, inclusion of ADP or uncoupler is necessary for assessment of complex IV turnover.

2.7.8 Maximum Electron Transport Chain Turnover

In the fully uncoupled state, oxygen consumption rates are controlled by the intrinsic ETC turnover capacity and substrate delivery. The conceptual framework of convergent electron flow predicts that substrate delivery may become limiting if restricted to complex-specific combinations, such as pyruvate/malate for complex I-linked respiration [151]. *In vitro* reconstitution of substrate delivery pathways therefore relies on combinations of substrates to maintain high ETC turnover [145]. Respiratory rates in the presence of pyruvate, malate, and succinate for example, are higher than respiratory rates with pyruvate/malate or succinate/rotenone alone [130,145]. As substrate preference is a system-specific property, preliminary experiments comparing respiratory activities supported by several substrate combinations provides the requisite information necessary for experimental design whereas detectable differences in these parameters could signify metabolic reprogramming in the system of interest. Inclusion of complex I- and complex II-linked substrates, such as pyruvate, malate, and succinate, as well as acylcarnitines to stimulate ß-oxidation, can ensure maximum substrate delivery [149].

Additional considerations for enhancing substrate supply lie in the modulation of post-translational modifications to enzymes in oxidative metabolic pathways. Treatment with dichloroacetate, for example, favors dephosphorylation and maximal activity of pyruvate dehydrogenase, further enhancing substrate supply to complex I [152].

Using chemical uncouplers to stimulate maximum respiratory activity depolarizes the inner membrane, removing control over respiration by the phosphorylation system. Respirometry is used to study changes in the phosphorylation system by replacing chemical uncouplers with saturating ADP to activate the whole of oxidative phosphorylation.

2.7.9 Phosphorylation System

The phosphorylation system consists of the adenine nucleotide translocator, phosphate transporter, and ATP synthase which function to import substrates for ATP synthase (ADP and P_i) and to export ATP to the cytosol to meet cellular energy demands [153]. Saturating ADP in the presence of saturating substrates induces maximal turnover of oxidative phosphorylation, composed of the ETC and ATP synthase coupled through the pmf (Figure 2.2). Detectable changes in oxidative phosphorylation turnover can be attributed to ETC capacity or ATP synthase but, importantly, are easily resolved by subsequent titration with uncoupler [81]. Loss of detectable differences upon uncoupler titration is consistent with dysfunction in the phosphorylation system whereas retention of differences suggests ETC changes, assuming mitochondrial content is controlled for. Use of ADP in permeabilized samples requires titration to maximum effect to identify and minimize potential diffusion limitations [143].

2.7.10 Upstream Substrate Delivery

Detection of impaired oxidation of a specific combination of substrates aids greatly in localizing dysfunctional metabolic segments; however, it is incapable of differentiating whether substrate supply or complex-specific changes drive the observed differences [135]. Direct addition of NADH to respiring mitochondria is ineffective at supporting respiration due to poor permeability of NADH through the inner membrane. Interestingly, use of alamethicin, a bacterial pore-forming toxin, induces NADH permeability through the inner membrane to drive ETC turnover through complex I [135]. As all membranes are permeabilized in the presence of alamethicin, exogenous cytochrome *c* is included to maintain ETC

turnover. Bypassing substrate delivery pathways to drive flux through the ETC directly, resolves ETC changes from those to upstream pathways including membrane transport and dehydrogenase activity [135].

2.7.11 Conclusion

Measuring rates of oxygen consumption by biological material has been a cornerstone of metabolic research for decades. Respirometry is used to reveal fundamental mechanisms underlying bioenergetics and is currently applied to a broad range of biological systems to study cancer, neurodegeneration, and immune cell metabolism. Respirometer design has evolved to offer highly stable, accurate, and precise instruments capable of operating competently under demanding conditions whereas miniaturization of sample chambers enabled highly sensitive and high throughput respirometry to be adapted by non-specialist laboratories for routine bioenergetics characterizations. Modern micromanufacturing methods such as 3D printing and the availability of a wide array of materials has enabled the formation of micron-scale features in complex 3D geometries. Combining optode-based oxygen sensing and 3D printing-based micromanufacturing can produce novel, flexible, and highly sensitive microrespirometers for use in non-specialist laboratories.

Respirometry is a powerful tool for bioenergetics studies as it allows for interrogation of a range of biological samples at varying levels of detail. Model systems such as whole cells or tissues are well suited to rapid screening by respirometry owing to rapid sample preparation, high yields, and the high physiological relevance. Standardized titration protocols yield quantitative estimates of basal, leak, ATP-linked, maximal, and background respiratory rates. Furthermore, normalization of respiratory rates to measures of total cell/tissue mass or to measures of mitochondrial content resolves inherent metabolic changes from changes to cell/tissue specific mitochondrial content.

Isolated mitochondria or permeabilized samples provide the requisite access to segment oxidative metabolism into finer detail and efficiently localize changes in metabolism. Retention of mitochondrial membrane integrity allows for *in vitro* reconstitution of oxidative metabolism to detect changes in pathway-specific substrate delivery including substrate transport and oxidation, complex-specific turnover capacity, maximal ETC capacity, oxidative phosphorylation system capacity, and integrity of inner and outer mitochondrial membranes.

The next chapter describes design and development of a novel 3D printed microrespirometer utilizing the design elements discussed above.

Chapter 3: Micro-Respirometry of Whole Cells and Isolated Mitochondria.

3.1 Introduction

Oxidation is the most common means of transducing hydrocarbons into energy. Aerobic organisms oxidize molecules in a stepwise manner while synthesizing adenosine triphosphate (ATP), the energy currency of the cell. Mitochondria are the specialized organelles where oxidation is coupled to phosphorylation by capturing the energy of electron transport, via a chain of proteins to O_2, to create a proton gradient across the inner mitochondrial membrane, which then fuels ADP phosphorylation.

As the main ATP generation mechanism of the cell, mitochondria have been extensively studied for over a century. The rate of oxygen consumption, the final step of the mitochondrial electron transport chain, provides information about the activity of electron transport chain protein complexes, transporters and ATP synthase. Two major approaches, polarographic or fluorescence quenching, are used for the measurement of O_2 concentration in solution, which provide the necessary data for calculation of oxygen consumption rates [83,87,88]. Sophisticated titration protocols using varying substrate and inhibitor combinations were developed to glean information about specific segments of the oxidative phosphorylation machinery. Though tremendous progress has been made in understanding mitochondrial function using these approaches, there are several limitations of currently available methodology. As polarographic measurements are based on the current produced by reduction of O_2 on an electrode, oxygen consumption by the sample must be significantly higher than that on the electrode, dictating the high tissue demand of this approach. Fluorescence quenching methods do not impose this demand, however, existing approaches utilize open configurations that require compensation for ingress of atmospheric oxygen due to diffusion. Finally, both polarographic and fluorescence quenching measurements are performed with static samples that only allow for cumulative, non-reversible titration protocols [80,106].

An enclosed flow-through cell respirometer has the potential of improving the currently available methodology by decreasing sample demand, greatly enhancing flexibility, and revolutionizing experimental approaches. The advantages of the flow-through approach were first demonstrated by Jekabsons and Nicholls [154]. Using oxygen electrodes to determine pre- and post-sample differentials in oxygen tension in a continuous medium steam, they monitored the respiration of primary cerebellar granule neuron cultures and determined the ATP supply and demand, proton leak, and mitochondrial respiratory capacity during chronic glutamate exposure. Although revolutionary, this approach required complex custom assembly and was not amenable to automation and scaling up for high-throughput measurements.

Recent developments in microfluidics and 3D printing technology provide new opportunities in the development of custom instrumentation [155]. In this study, we used O_2-impermeable 3D printing plastics to manufacture microchannels. Optical transparency of the plastic allowed us to sample an oxygen-sensitive fluorescence-based thin film deposited on the inner surface of the channel without exposing the sample to atmospheric O_2. We show that adherent cells can be cultured directly on-chip and sampled over prolonged periods of time using repetitive and reversible stimulation of a given sample for observation of metabolic response. In addition to adherent cells, the experimental protocol can be adapted to isolated mitochondria and cell suspensions. Ease of production, flexibility in protocol design, and direct quantitative reporting of O_2 consumption rates make this system highly amenable to both precise individual measurements of traditional respirometry and parallelization as needed for drug discovery and testing.

3.2 Methods

3.2.1 Materials

Dulbecco's phosphate buffered saline (DPBS; D8662), bovine serum albumin (BSA), oligomycin, carbonyl

cyanide m-chlorophenyl hydrazone (CCCP), polystyrene pellets (PS), KCN and general laboratory chemicals were of reagent or better grade from Sigma-Aldrich (St. Louis, MO) and were used as acquired. Platinum octaethylporphyrin (PtOEP) was from Frontier Scientific (Logan, Utah). Prefabricated materials were from McMaster-Carr (Elmhurst, IL).

3.2.2 Micro-respirometric Oxygen Sampling

The microfluidic respirometer (MfR) was designed in Autodesk Inventor (Autodesk Inc, San Francisco, CA) and printed on an Objet Connex 350 or J750 (Objet Geometries Inc, Billerica, MA) 3D printer in VeroClear, a polymethylmethacrylate-like clear resin (Objet Geometries Inc). MfR consisted of three parts (Figure 3.1A): the manifold (top), the sensing chip (middle), and the compression base (bottom). The manifold provided fluidic interface to the chip and positioned sampling optical fiber immediately above the optode (below). Continuity of the ports was achieved by compression of o-rings (size -001, Buna-N, shore durometer 70A) between the chip and the manifold. The entire assembly was compressed vertically using four bolts, hand tight. Pressure was transferred to the chip and the o-rings via a stacked wave disk spring for better alignment of contact surfaces of the chip and the manifold without pressure points.

Two interchangeable versions of the chip were produced: closed shell (Figure 3.1B) and open shell (Figure 3.1C) configurations for suspension and adherent samples, respectively. A 2.0 mm wide by 0.15 mm deep microchannel of the same geometry was manufactured by 3D printing in VeroClear in both cases.

In the closed-shell configuration, the channel was formed by permanent adhesion of the printed part to the flat glass substrate. Four parts of Loctite EA E-30CL epoxy mixture were thinned with 1-part chloroform and applied along the perimeter of the microchannel, ensuring no spillover into the channel. The chip was spun at 2100 rpm for 20 seconds and solvent evaporated for 5 minutes at room temperature. A glass cover, cleaned in acetone, was applied to the chip and cured overnight under mechanical pressure.

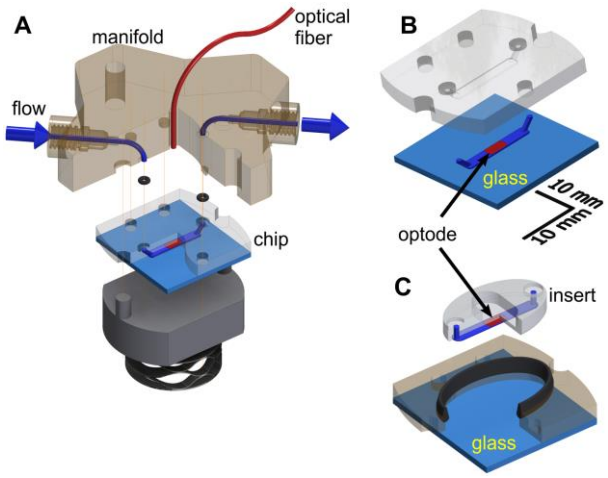

Figure 3.1: Schematic of the MfR for adherent and non-adherent samples. (A) An exploded view of MfR. Solution flow is shown in blue. Optical fiber and O_2 sensor are shown in red. O-rings are shown in black. Vertical lines show alignment points. (B) Closed shell configuration for suspension measurements, showing a 3D-printed chip adhered to glass (cyan). (C) Open shell configuration for adherent measurments. Integral seal is shown in black.

In the open-shell configuration, the 3D-printed part was split into two components (Figure 3.1B). The outer section of the chip formed a well and was adhered to the glass the same way as for the closed-shell version. It ensured proper alignment on the central, oval section (insert) against the manifold. The microfluidic channel was formed by pressing the insert against the glass without additional adhesives. An elongated, 1.4 mm by 2.6 mm cross section soft seal (shore durometer 26A – 28A) was co-printed in Tango+ 3D printing resin along the perimeter of the well to prevent leaks. The seal was positioned along the upper edge of the well (Figure 3.1B) to provide simultaneous 2-way contact with the outer edge of the insert and the bottom surface of the manifold.

In both configurations, the microchannel-containing surface was oriented upwards on the printer bed to prevent support material deposition in the microchannel. Bulk supporting plastic was removed using a brush with medium-soft plastic bristles followed by overnight soaking in a stirred solution of 2 M potassium hydroxide in water saturated with sodium bicarbonate as a mild abrasive. Cleaned parts were washed with deionized water and air dried before further use. Glass-contacting surfaces of chips in both designs were polished on 5 µm grit silicon carbide sheet after optode deposition to improve flatness.

The O_2 optodes were deposited by casting or spin coating methods. For drop casting, a ~220 mg/mL stock solution of PS in bromobenzene or chloroform was prepared at room temperature overnight. The working PS/PtOEP solution was prepared by 1:4 (v/v) dilution of PS stock with a 2 mg/mL solution of PtOEP in the same solvent. One microliter of the PS/PtOEP mixture was deposited into the center of the microchannel and dried under a stream of warm air (T < 50 °C). For spin coating, PtOEP (~ 1 mg/mL) and 12.5 – 25% (m/m) PS in bromobenzene or chloroform solution was applied to the chip followed by spinning at 1000 rpm for 2 minutes. Remaining solvent was removed under reduced pressure (0.2 bar) overnight.

The measurements are based on the reversible quenching of the luminescence intensity and decay time of PtOEP by oxygen modelled by the Stern–Volmer equation[25]. The measurements were performed using a NeoFox GT phase fluorimeter with NeoFox Viewer software (Ocean Optics, Dunedin, FL). Fluorescence lifetime of the PtOEP sensor was acquired through the MfR wall by an unterminated optical fiber (ThorLabs Inc., Newton, New Jersey) at a minimal sensor to fiber distance (Figure 3.1D, see Results). The optical fiber was coupled to a bifurcated optical fiber of the fluorimeter by a bare fiber terminator (ThorLabs).

3.2.3 Oxygen Permeability and Solubility

Oxygen permeability was measured following ASTM D-3985 using a Mocon Oxtran 2/21 (Minneapolis, MN) as previously described [156,157]. VeroClear discs were printed at 0.5 mm (N = 2) and 0.2 mm (N =2) thicknesses in two separate batches. Measured thicknesses were within 8% of the nominal thicknesses (0.184 ± 0.008 mm; 0.185 ± 0.010 mm; 0.477 ± 0.003 mm; 0.479 ± 0.009 mm), thus nominal values were used for calculations. Polyetheretherketone (PEEK) film (76.2 µm thick) was cut to size and measured under identical conditions (N = 4). The thin film was conditioned for 1 hr. Measurements were performed at 23°C and 37°C using dry 100% O_2 at a flow rate of 20 sccm against 10 sccm flow of 98% N_2, 2% H_2 as a carrier gas.

Assessment of oxygen solubility was performed using air-equilibrated and anaerobic water in ambient air and in a glovebox (Pas-Labs Inc., Lansing, Michigan) purged with nitrogen (<10 ppm O_2). Anaerobic water was prepared using a Schlenk line over 7 cycles between 0.026 atm vacuum and 1 atm Ar gas with agitation. Solutions were delivered to the chip from a gas-tight syringe through a minimal length of PEEK tubing.

3.2.4 Cell Culture and Respiration Assays

ARPE-19 cells (ATCC, CRL-2302, passage 31) were grown on 75 cm2 polystyrene flasks (T75 flask; Corning Life Sciences, Oneonta, NY) in 50% Dulbecco's modified Eagle's medium low glucose base media (DMEM; Corning Cellgro, Manassas, VA), 50% F-12 supplement (Life Technologies, Grand Island, NY), 1% antibiotic/antimycotic mix (Thermo Fisher Scientific, Waltham, MA) with 10% fetal bovine serum (Atlas Biologicals, Fort Collins, CO). Bovine Retinal Endothelial Cells (BREC) were isolated and cultured as previously described in 10% Fetal Bovine Serum (FBS) Complete Media with 1% Antibiotic/Antimycotic (AA) (Gibco; ThermoFisher; Waltham, MA) [43]. Passages 4-8 were used for all experiments. At 100% confluence, cells were trypsinized (0.25% trypsin-EDTA) (Thermo Fisher Scientific) and counted using the Trypan blue exclusion cell viability method (Sigma Aldrich). Cells were either plated on the MfR well or stored, in suspension, on ice for adherent or non-adherent measurements, respectively. 100% confluence, cells were trypsinized, counted and either plated in the MfR well or stored on ice prior to measurements.

3.2.5 Glucose Oxidase Assays

Stock solutions of glucose oxidase (GOx) and glucose were prepared in 50 mM potassium phosphate buffer, pH 7.5, and diluted in the same buffer as necessary. Assays were prepared by mixing 1:1 (v/v) of glucose and GOx stock solutions to a final concentration of 75 mM glucose and varying concentrations of GOx as indicated. The microchannel was flushed with blank buffer between trials.

3.2.6 Non-Adherent Samples

ARPE-19 cell suspensions were stored in buffer containing 148 mM NaCl, 5 mM KCl, 0.81 mM $MgSO_4$, 0.83 mM Na_2HPO_4, 0.14 mM KH_2PO_4, 1 mM $CaCl_2$, 25 mM $NaHCO_3$, 15 mM glucose at pH 7.5 [132]. Aliquots of the cell suspension stock were mixed with various buffers (*vide supra*) immediately prior to loading 2.0 - 33×10^3 cells/µL into the MfR using a 20 µL pipette. The microchannel was flushed with PBS between trials.

A high-resolution respirometer, Oxygraph-2k (Oroboros Instruments Corp., Innsbruck, Austria), was used as a reference following standard protocols at 23° C [80,110].

3.2.7 Adherent Samples

A removable, 3 mm in diameter by 3 mm in height seeding mask was used in preparation of the adherent cell respirometry. The seeding mask was printed in VeroClear and overcoated with polymethylmethacrylate (PMMA) by dip coating into a 5% (m/m) solution of PMMA in methylethylketone and drying overnight at 50° C. The open-shell well (Figure 3.1C) and the seeding mask were sterilized by washing with 70% ethanol in water followed by 15 min of UV irradiation prior to seeding.

ARPE-19 cells were loaded into the mask at densities of 3.5 – 7.0×10^3 cells/mm^2 and cultured overnight. Photomicrographs were acquired using an inverted light microscope equipped with an AmScope 0.3 megapixel color CMOS camera (United Scope, Irvine, CA) prior to measurements. Surface density was calculated using ImageJ software by converting the RGB photomicrograph into 16-bit greyscale and applying a median filter (2 pixel radius). Find maxima was used to segment cells (noise tolerance of 5 – 8) excluding edge particles.

Respiratory activity was measured under stationary medium conditions. Medium flow of 10 - 20 µL/min for re-oxygenation and reagent replenishment was controlled by a syringe infusion pump (Model 22,

Harvard Apparatus, MA). Stationary conditions were assured by a manual diversion valve that isolated the chip from the pump.

The base cellular respirometry buffer (BB_C) consisted of DPBS with calcium and magnesium (Sigma-Aldrich) supplemented with 0.2% BSA. Respiration buffer (RB_C) consisted of BB_C supplemented with 10 mM glucose, 10 mM lactate, and 1 mM pyruvate. Leak buffer (LB_C) contained RB_C with 2.5 µM oligomycin. Uncoupling buffer (UB_C) contained LB_C with 5 µM CCCP. Inhibition buffer (IB_C) contained UB_C with 5 mM KCN [77].

3.2.8 Mitochondrial Isolation and Assay

ARPE-19 cells were trypsinized, resuspended in ice cold mitochondrial isolation buffer (MIB) (200 mM sucrose, 50 mM mannitol, 5 mM MOPS, 1 mM EGTA, 5 mM K2HPO4, pH 7.5) and homogenized using a Teflon pestle (20 strokes at 3000 RPM). Homogenate was centrifuged at 600 g for 10 min and supernatant was collected. Pellet was resuspended in 3 mL of fresh ice-cold MIB, homogenized and centrifuged two more times collecting supernatant every time. The pooled supernatants were centrifuged at 7,000 g for 10 min, discarding supernatant. The pellets were resuspended in 200 µL of MIB, pooled and centrifuged again for 10 min at 7000 g, repeating three times. Final pellet was resuspended in a minimal volume of ice-cold MIB and stored on ice prior to use. All steps were performed at 4° C [158]. Isolated mitochondria were stored on ice prior to measurements.

The base mitochondrial respiration buffer consisted of 130 mM KCl, 20 mM Tris, 10 mM EGTA, 1 mM sodium phosphate at pH 7.5. Mitochondrial leak buffer contained 5 mM pyruvate, 0.5 mM malate, 10 mM succinate in base buffer. Leak buffer was supplemented with 0.24 mM ADP for ADP-stimulated respiration. Inhibited rates were determined by addition of 5 mM KCN and ADP to leak buffer. Total mitochondrial protein was determined using Bradford assay (BioRad).

3.2.9 Calibration and Data Analysis

Calibration was performed daily using air equilibrated buffer as the aerobic standard (245 µM) and fresh ~1 mM sodium dithionite solution in the same buffer as anaerobic standard [121,159]. The Stern-Volmer relation was used to convert fluorescence lifetime to O_2 concentration [118,160,161]. Oxygen consumption rates (R_{O2}) were determined by linear fitting of steady state phases. For enzyme assays, background activity was corrected by subtracting R_{O2} of the buffer blank. For mitochondrial or cellular measurements, the R_{O2} of inhibited samples was subtracted from all others. Polynomial background drift corrections were applied to O_2 traces in some instances. Data analysis was performed using IgorPro (Wavemetrics Inc., Portland, OR) software.

3.3 Results

3.3.1 3D Printed Chip and Oxygen Optode Geometry

Figure 3.1 shows a schematic of the device consisting of 3D printed flat chip with O_2 sensor film deposited in the microchannel. Optically transparent VeroClear allowed sampling of the sensor by the optical fiber (Figure 3.1D). Patency of the microchannels was ensured by low-pressure perfusion prior to use. Distance between the optode and the optical fiber was 1.75 mm in the non-adherent configuration and 0.55 mm in the adherent configuration. An acceptance angle of 23^o for the 1.0 mm fiber resulted in circular fields of view with diameters of 2.48 mm and 1.47 mm for the non-adherent and adherent configurations, respectively. Drop-coated optode, with a limiting area of 1.8 mm^2, was probed by an oversized field of view in the non-adherent configuration. In the adherent configuration, a section of an oversized optode was sampled by a limiting 1.7 mm^2 field of view.

Nominal dimensions of non-adherent microchannels were 0.25 mm deep by 1.20 mm wide. Average printed microchannel width was 1.09 ± 0.117 mm (N = 3). Average channel depth was 0.235 ± 0.013 mm

(N = 3) and 0.145 ± 0.017 mm (N = 3) before and after polishing, respectively. Nominal and measured dimension of the adherent configuration were 0.150 mm vs 0.131 ± 0.018 mm (N = 3) in depth and 2.00 mm vs 2.23 ± 0.006 mm (N = 3) in width.

3.3.2 Sample Demand for Cellular Respiration

ARPE-19 cells were chosen for their robust respiratory capacity and high rate of proliferation, yielding abundant sample for instrument characterization.

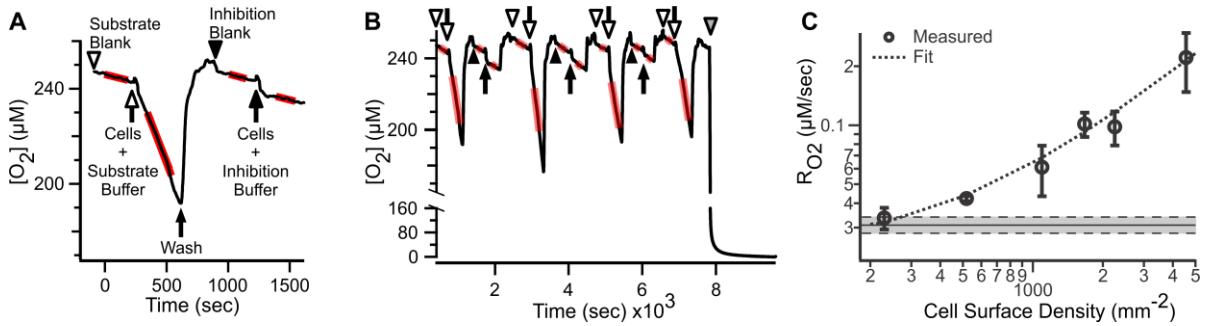

Figure 3.2. R_{O2} by ARPE-19 cell suspension in the microrespirometer. (A) Detailed view of ARPE-19 substrate supported and KCN inhibited respiration (12.5×10^3 cells/μL). (B) Reproducibility of alternating injections of respiring and inhibited cells. Arrows and arrowheads indicate cell suspension and blank measurements, respectively. Hollow and solid symbols indicate respiration buffer (RB_C: 10 mM glucose, 10 mM lactate, 1 mM pyruvate) and inhibition (IB_C: RB_C + 5 mM KCN) buffer, respectively. Gray arrowhead shows anaerobic calibration. Regions used for determining R_{O2} are shown by red highlights. (C) Basal R_{O2} of ARPE-19 cells with various densities, including linear fit of data (dashed line, $y = 0.02 + 4.22 \times 10^{-5} x$, $R^2 = 0.98$). Shaded area – mean of inhibited cells ± SEM (N=5). R_{O2} are expressed as mean ± SEM (N=3-5).

A representative oxygen concentration trace using suspensions of ARPE-19 cells is shown in Figure 3.2A and 3.2B. Buffer blanks were used for system equilibration (arrowheads) until stable baseline was observed. Aliquots of ARPE-19 cells were pre-mixed with respiration buffer (hollow arrows; 10 mM glucose, 10 mM lactate, 1 mM pyruvate) or inhibition buffer (solid arrows; respiration buffer + 5 mM KCN) and loaded into the microchannel. Separate aliquots were prepared from the same suspension stock and sequentially sampled. After acquiring cellular R_{O2} for 3-7 min, the microchannel was purged using blank buffer at 2.25 mL/min for 3-5 min, resulting in rapid re-oxygenation of the microchannel and no evidence

of residual activity in the subsequent blank measurement. Cellular R_{O2} with inhibition buffer was not distinguishable from blank baseline. Injection of anaerobic standard (gray arrowhead) was used for calibration. Transient artifacts were seen immediately after sample loading, including O_2 consumption during handling, and were excluded from the steady-state R_{O2} assessment.

The microfluidic respirometer sensitivity was characterized using varying cell suspension densities. Figure 3.2C shows that R_{O2} scales linearly with cell density (R^2 = 0.98, linear regression) across an order of magnitude change in R_{O2}. Linear interpolation of observed R_{O2}, and its errors, showed the lower limit of detection of approximately 500 cells. Variances increased with increasing cell density, effectively limiting the upper bound of meaningful R_{O2} determinations. Examination of cell suspension delivery into the MfR by light microscopy revealed non-homogeneous cell distribution at cell densities higher than 17×10^3 cells/μL, likely contributing to the increased variability in dense suspension.

Oxygen diffusion limits the sensitivity of respirometers and leads to ambiguity in data interpretation. As glass is impermeable to O_2, diffusion of atmospheric O_2 from the open ports along the major axis of the microchannel and diffusion through the VeroClear walls are the two remaining routes in the microchannel. The first mechanism is unlikely to contribute significantly to O_2 ingress due to the diffusion distance (5.6 mm) and respiration by cells occupying the entire channel, effectively isolating the cells in the sampled volume. Thus, O_2 diffusion through VeroClear is the most probably source of O_2 ingress. The room temperature (23°C) barrier properties of VeroClear (0.125 ± 0.007 barrer) were comparable to that of PEEK (0.143 ± 0.001 barrer). Permeability of VeroClear increased 1.8-fold to 0.218 ± 0.006 barrer at 37°C. Since O_2 permeability at both temperatures was comparable and this study focuses on the fitness of the current approach for respirometry over details such as metabolic response to temperature, further analysis was performed at ambient temperature.

Since the ingress of O_2 into the sample during measurement may lead to a significant underestimation of

R_{O2}, we assessed the bi-directional mass transfer of dissolved O_2 between the microchannel and the enclosing materials, including plastic and capillaries [79,110,162]. Figure 3.3 illustrates changes in dissolved O_2 at the minimal and maximal concentration gradients in aerobically (left) and anaerobically (right) conditioned open-shell chip. To eliminated potential contribution of proteins adsorbed to the chip surfaces, measurement was performed on a fresh chip that was not used in other studies.

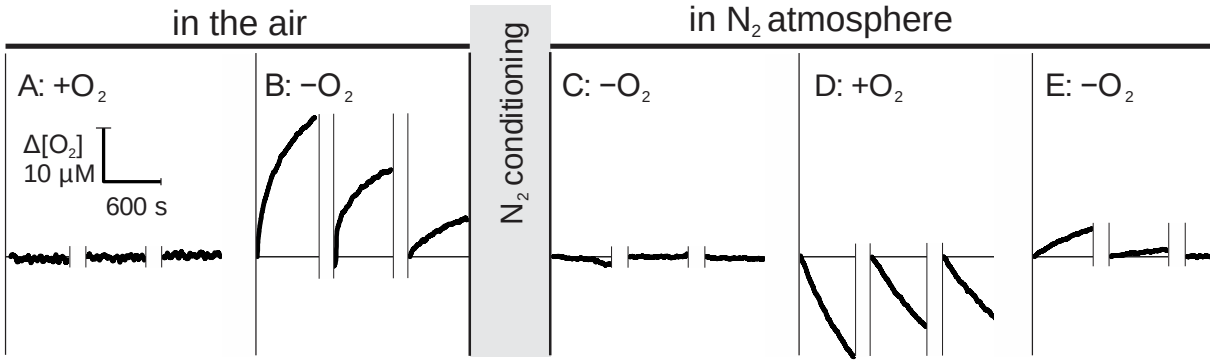

Figure 3.3. Interface mass transfer of O_2 under zero and maximal gradients. *Left:* Sequential measurements in a fresh, closed-shell chip that remained in the air since printing. Measurements using air-equilibrated (A) and anaerobic (B) water were performed in stationary solution and were alternated with 10-min wash and replenishment phases, shown by the breaks over time axis. Changeover from (A) to (B) included a 20-min purge with anaerobic water. *Right*: The same chip was transferred into a glovebox and conditioned for 48 h with N_2 stream over microchannel. Measurements were performed as in the left panel using anaerobic (C), air-equilibrated (D), and again anaerobic (E) water. In all cases, O_2 concertation is expressed as a change from the start of each stationary measurement. Changes in the concentration indicate ingress (B, E) and egress (D) of O_2 into and from the solution, respectively.

Sequential sampling of aerobic water in the air-equilibrated chip (Figure 3.3A) showed no distinguishable changes in the solution [O_2], as expected for zero pO_2 gradient between the plastic and the solution. Rapid replacement of aerobic water with anaerobic water to impose a maximal gradient on the same chip resulted in pronounced ingress of O_2 from plastic into the solution (Figure 3.3B). The observed ingress is attributed entirely to the immediate vicinity of the optode and not the upstream components because measurements were performed in the stationary solution. The average ingress rate decreased from 0.04 µM/sec to 0.01 µM/sec between the first and the third measurement, suggesting that while a substantial

amount of O_2 may be dissolved in the thin layer of air-equilibrated plastic, contribution of mass transfer from deeper layers is small, in agreement with direct permeability measurements.

This conclusion was further supported by the opposite trend that was observed when the same chip was pre-conditioned in anaerobic (N_2) atmosphere for 48 hours. Initial measurement of anaerobic water in the N_2-conditioned chip (Figure 3.3C) showed no ingress of O_2 into the sample. A noticeable loss of O_2 was observed when air-equilibrated water was subsequently measured in the same N_2-conditioned chip, attributable to the mass transfer of O_2 from the solution into plastic. The O_2 transferred into the plastic from the aerobic solution can be available for re-entry into the solution until it diffuses further from the interface. This was, indeed, observed when the perfusing solution was reverted to anaerobic water. Figure 3.3E shows a noticeable, but rapidly diminishing, re-entry of O_2 from transiently oxygenated plastic into the solution.

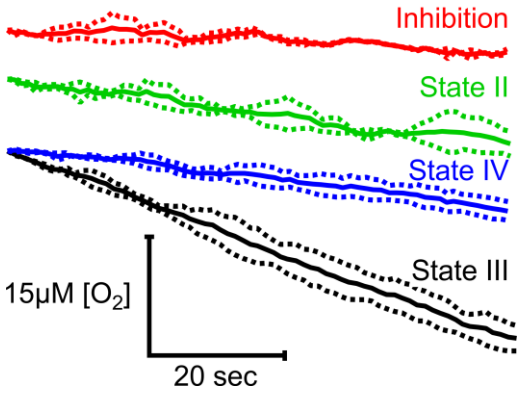

Figure 3.4. Classical states of mitochondrial R_{O2} in the MfR. Red trace indicates inhibition by KCN. Green – leak buffer, black – leak buffer + 0.24 mM ADP, blue – leak buffer + 0.24 mM ADP after complete ADP phosphorylation. Traces were overlaid at t=0 and averaged over the steady state (solid lines). Dashed lines show ± SD. N=2 for inhibition and state II, N=4 for state III and IV.

3.3.3 Isolated Mitochondria

To demonstrate the suitability of MfR for metabolic studies, R_{O2} of mitochondria isolated from ARPE-19 cells was investigated under conditions mimicking standard respirometric measurements (Figure 3.4). In

the presence of saturating substrates (State II), mitochondrial respiration is limited by a protonmotive force and the observed R_{O2} is controlled by ATP hydrolysis and proton leak. Addition of ADP activates ATP synthase, decreasing the proton motive force and increasing the observed R_{O2} (State III). Upon complete phosphorylation of ADP, the increase in proton motive force again limits the observed R_{O2} (State IV) to levels similar to the leak state. Background R_{O2} is determined from KCN-inhibited samples.

3.3.4 R_{O2} of Cells in Suspension

Similar substrate-inhibitor modulation of whole cell suspensions in the microchannel is shown in Figure 3.5. Substrate-inhibitor modulation of R_{O2} by the same cell line in a high-resolution respirometer is shown for direct comparison. Inhibition of ATP synthase and a corresponding increase in the inner membrane potential by oligomycin caused the expected decrease in cell specific R_{O2} relative to basal R_{O2} in both

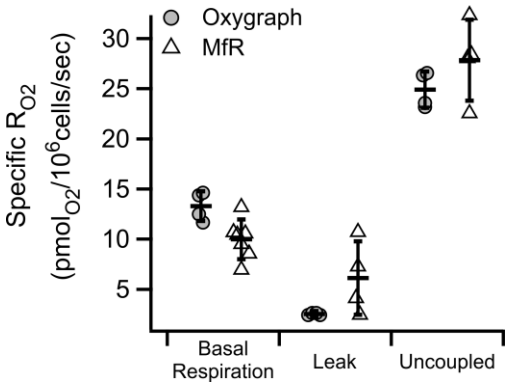

Figure 3.5. Characteristic R_{O2} states of whole cell in the MfR compared to traditional oxygraph. Specific R_{O2} are inhibition corrected, normalized to cell density and expressed as mean ± SD. N=4 for oxygraph, N=4-7 for MfR.

approaches (Leak). Maximal cell-specific R_{O2}, achieved by dissipating the membrane potential using 5 µM CCCP (mitochondrial uncoupler) in the presence of substrates, were 0.025 ± 0.002 and 0.028 ± 0.004 $nmol_{O2}/10^6$cells/sec in the oxygraph and in microfluidic respirometer, respectively (Uncoupled). The increased variability of R_{O2} in the MfR was attributed to manual handling of high-density cellular suspensions.

3.3.5 Variability in Homogeneous Samples

To characterize the sensitivity and reproducibility of the MfR independent of the variability associated with suspensions, measurements were performed using a homogeneous glucose-glucose oxidase (Glu-GOx) enzyme system to mimic cellular R_{O2}. Figure 3.6A shows a representative trace of sequential Glu-GOx measurements. Inter-trial R_{O2} reproducibility was high and little residual Glu-GOx activity was detected following washes, which would appear as a loss of O_2 during blank measurements. Figure 3.6B shows averaged traces of multiplicate measurements of R_{O2} at [GOx] of 0, 0.09, 4.85 and 333.5 µg/mL with 75 mM Glu. At low [GOx] the R_{O2} (blue) is statistically indistinguishable from the blank (red). At

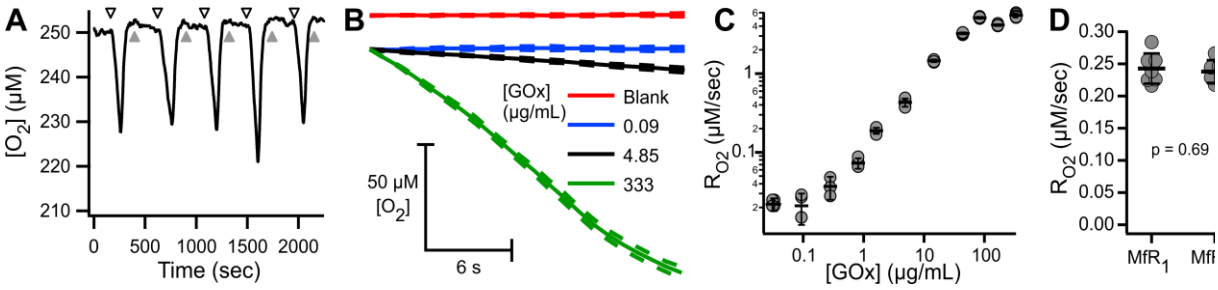

Figure 3.6. Characterization of MfR using homogeneous model reaction. (A) Raw trace of Glu-GOx R_{O2} assay. Gray and black arrows show buffer blank and 4.85 µg/mL GOx + 75mM Glu in 50mM KPi (pH 7.5), respectively. (B) O_2 consumption traces by select GOx concentrations. Solid lines indicate overlaid and averaged blank and reaction trials. Dashed lines represent ± SD (N = 5-6). (C) Dynamic range of the MfR using Glu-GOx R_{O2} expressed as mean ± SD, N = 3-5. (D) Inter-MfR reproducibility using Glu-GOx expressed as mean ± SD, N = 6-7.

intermediate [GOx], there is a linear decrease in $[O_2]$ (black), and at high [GOx] there is a loss of linearity in the $[O_2]$ decrease (green). The loss of linearity at the upper limit of MfR sensitivity corresponds to the sensor response time. Maximum apparent R_{O2} was 5.22 ± 0.43 µM/sec (N = 3), observed following injection of anaerobic standard. R_{O2} between of 0.03 and 2.5 µM/sec showed a linear dependence on [GOx] (Figure 3.6C).

The Glu-GOx model was also used to assess inter-instrument variability of the MfR (Figure 3.6D). R_{O2} were measured in parallel, on two separate MfR and fluorimeters, using common Glu-GOx stocks. The R_{O2}

values obtained on each instrument, 0.243 ± 0.024 and 0.238 ± 0.018 µM/sec (N = 6-7), were not statistically distinguishable (p = 0.69, t-test).

3.3.6 R_{O2} of Adherent Cell Samples

Adherent cell culture models were used to increase reproducibitliy, decrease sample demand, and permit transient sample stimulation using repetitive measurements of a given biological sample. As cell adhesion

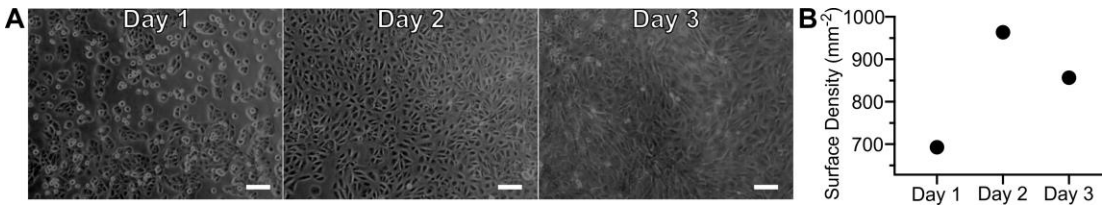

Figure 3.7: Adherent cell configuration of the MfR. Photomicrographs (A) and quantitation (B) of ARPE-19 cell growth and proliferation on cell culture well of the MfR. Scale bars = 100 µm.

required extended incubation in proximity to a material with unknown biocompatibility, gross toxicity was assessed by culturing ARPE-19 cells on-chip, without a seeding mask, for several days (Figure 3.7A and 3.7B). Photomicrographs, obtained daily, showed no visible differences between cells in the central and peripheral areas, indicating that proximity to polymer did not affect cell growth. After overnight incubation ARPE-19 cells exhibited an adherent cell morphology. Subsequent proliferation over the three-day incubation period resulted in the cobblestone appearance typical of this cell type [163]. Cell surface density quantitation over time is presented in Figure 3.7B, demonstrating an initial increase followed by a plateau at day two in culture. The biocompatibility of the MfR instrument was further confirmed by a long-term continuous measurement of adherent cells, which showed no changes in respiration over 24 hours (Figure 3.11 in Appendix A).

Following cell culture under standard conditions, the removable insert was used to form a microchannel immediately prior to R_{O2} measurements.

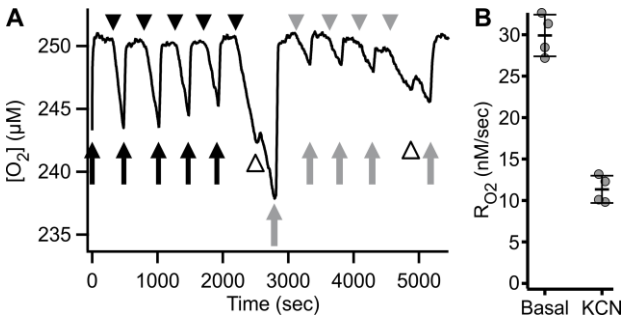

Figure 3.8. Repetitive R_{O2} assessment of adhered ARPE-19 cells. (A) Representative O_2 trace showing R_{O2} of 2800 ARPE-19 cells. Arrowheads – no buffer flow, arrows – buffer flow, black – respiration buffer, gray – inhibition buffer, white arrowheads – buffer exchange artifact. (B) Quantitation of basal (RB_C) and inhibited (IB_C) R_{O2} obtained from (A), expressed as mean ± SD (N=4).

Figure 3.8 shows an example of R_{O2} measurements in adherent ARPE-19 cells. Under a constant flow of buffer (Figure 3.8A, arrows), the microchannel remains fully oxygenated as O_2 delivery is faster than consumption. Assessment of R_{O2} was achieved by arresting buffer flow (Figure 3.8A, arrowheads), resulting in a linear decrease of dissolved O_2 over time. Resumption of flow (Figure 3.8A, arrows), leads to re-oxygenation of the microchannel. Analysis showed a mean basal R_{O2} of 0.030 ± 0.002 (± 8.4%) μM/sec and a mean inhibited R_{O2} of 0.011 ± 0.002 (± 14.6%) μM/sec (N = 4) as shown in Figure 3.8B.

The continuous medium flow utilized in the microchannel allows for fast and complete exchange of buffer for reversible activation/inhibition cycles using a single cell sample. This capability is illustrated in Figure 3.9A and 3.9B. Basal R_{O2} is inhibited in the presence of the reversible inhibitor KCN. Upon subsequent perfusion with KCN-free buffer (RB_C), 99.6% of basal activity is recovered within 880 seconds at 10 μL/min flow. Finally, R_{O2} of adherent ARPE-19 cells was examined using the same sequence of modulation as described above for cell suspensions (Figure 3.5). Figure 3.9C shows basal, oligomycin-inhibited, CCCP-uncoupled and KCN-inhibited R_{O2} obtained from 3.4×10^3 cells. The patterns of stimulation and inhibition were recapitulated with adherent cells and, importantly, showed significantly decreased variance of R_{O2}

using the adherent configuration compared to cell suspensions. Significant and reproducible decreases were noted in R_{O2} after cell adhesion, as discussed below.

3.4 Discussion

Measurement of dissolved O_2 content provides valuable information on metabolic activity of plant, bacterial, animal and human samples. Sophisticated systems are commercially available for respirometric

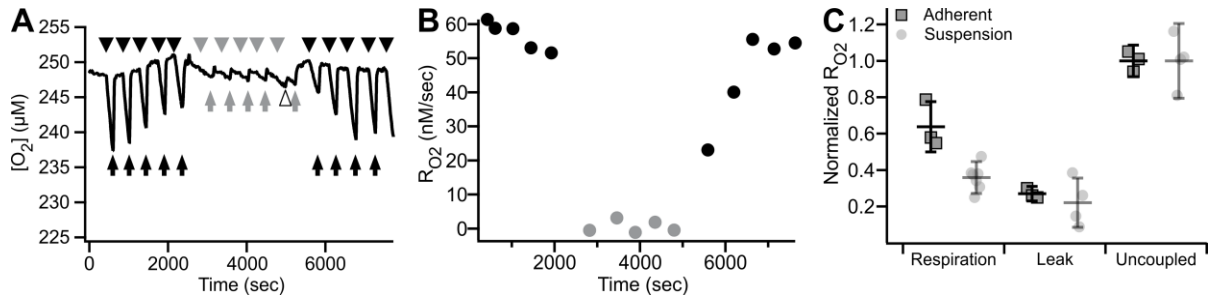

Figure 3.9. Reversible inhibition of respiration in the MfR. (A) Trace of reversible respiratory inhibition by KCN in adherent ARPE-19 cells cultured on MfR. Arrows – buffer flow, arrowheads – static buffer, black – RB_C, gray – IB_c, white arrowhead – buffer exchange artifact. (B) R_{O2} quantitation of the results shown in (A). Black circles – respiration buffer, gray circles – inhibition buffer. (C) Classical states of whole cell R_{O2} in the adherent compared to suspension MfR configuration. Respiration was in glucose, lactate, pyruvate (10, 10, 1 mM), leak was by addition of oligomycin (2.5 μM), and uncoupled R_{O2} was by addition of CCCP (5 μM). Squares – adherent cells, gray faded circles – suspension (from Figure 5). R_{O2} were normalized to uncoupled respiration and expressed as mean ± SD (N = 3).

measurements; however, the advantages of each are balanced by unique limitations such as high sample demand, operating cost, and limited adaptability to sample type [81,106,164]. In this study we combined the advantages of high-resolution 3D printing with fluorometric O_2 detection to produce a simple, versatile, and highly sensitive method for micro-scale repetitive respirometry.

Measurements on cell suspensions demonstrated the high sensitivity of the MfR, detecting R_{O2} in as few as several hundred cells (Figure 3.2). This represents three orders of magnitude higher sensitivity than large volume respirometers, and approximately 10 times the sensitivity of plate-based respirometry [81,106]. Such sensitivities are afforded by the small volumes, tight control over O_2 ingress, and short distances between the optode and respiring cells. Suspension measurements showed minimal gain from

increasing cell density as higher absolute R_{O2} were offset by decreased reproducibility. Sensitivity of adherent cell measurements is proportional to surface cell density and inversely proportional to the channel depth, but is independent of channel width or length, assuming a uniform cell monolayer and sensor width greater than channel depth. Therefore, reduction in channel depth is beneficial until shear stress and O_2 ingress become liming factors (below). The phase-based fluorescence lifetime detection of O_2 by PtOEP in a polystyrene matrix is independent of film thickness and fluorophore concentration, enhancing reproducibility (Figure 3.6D and Figure 3.8) [94].

In Figure 3.5 we showed R_{O2} modulation by respiratory effectors, measured using a traditional oxygraph and the MfR. The expected trends were recapitulated in the MfR with some notable exceptions. The magnitude of inhibition caused by oligomycin was smaller in the MfR whereas the magnitude of stimulation by CCCP was larger. Additionally, MfR cell suspensions showed high R_{O2} variances compared to polarographic R_{O2}, where cell densities were 2-6-fold lower than in MfR. Both higher variances and changes in modulation efficiencies are likely to arise from the higher cell densities in the MfR. Though the chemical composition of assay buffers were the same, the lipophilic modulators, oligomycin and CCCP, require optimization of modulator to membrane ratios in order to achieve optimal membrane concentrations without side effects [165–168]. Despite these differences, we observed excellent agreement of cell-specific uncoupled R_{O2} between the oxygraph-2k and microfluidic respirometer, demonstrating the utility of microfluidic respirometry in classical respirometric assays. Uncoupled R_{O2} was chosen as a normalization between instruments because it represents near-maximal respiratory capacity without the limiting effects of metabolic load.

High variances in cell suspension measurements are attributed to micropipetting of concentrated cell stocks and cell sedimentation during sample loading, which can be minimized by incorporating hydrodynamic focusing [169,170]. We reasoned, however, that the high variability between independent cell suspension trials can be remediated by immobilization of the sample, which also improves

physiological relevance due cell-cell and cell-substrate contacts in natively adherent cell types. Repeated probing of a given sample in the adherent configuration not only improved variability of R_{O2} determination (Figure 3.8) but further reduced sample demand relative to cell suspensions, requiring delivery of homogeneous medium between samplings. Importantly, ARPE-19 cells had lower metabolic rate in the native adherent state compared to the same cells in suspension. Such changes in metabolic rate upon resuspension of natively adherent cells is expected and highlight the versatility of the microfluidic respirometer, allowing for precise tuning of experimental design to the research question.

The interrupted-flow approach in the adherent microfluidic respirometer configuration enables development of novel measurement strategies [154]. First, cell samples are kept at the desired [O_2] (near saturation in this study) because cellular R_{O2} is measured for a short period before medium replenishment. This allows the microfluidic respirometer to sustain prolonged experiments without inducing metabolic changes associated with hypoxic responses (Figures 3.8, 3.9A and 3.10). Continuous buffer exchange can mimic classical titration-based protocols and is further amenable to addition and removal of metabolic stimuli to study reversibility of metabolic switches (Figure 3.9). As an example, we demonstrated reversible respiratory inhibition by KCN (Figure 3.9A and 3.9B) and observed the kinetics of R_{O2} recovery prior to reaching the near-complete pre-inhibition activity. These transient metabolic states are attributed either to partial washout of the inhibitor or, alternatively, to cellular recovery from the metabolic insult. Regardless of the cause, these observations open intriguing possibilities for the investigation of time-dependent metabolic changes affecting R_{O2} in real-time and the opportunity to resolve transient metabolic states during stimulation.

Isolation of the sample from the atmospheric environment is particularly important for microrespirometry due to the high surface area to volume ratios inherent in microfluidics. In such regimes, surface exchange of O_2 can lead to relatively rapid changes in bulk O_2 concentrations in the medium. This property is used widely for the development of microfluidic hypoxia incubators which focus on controlling

and rapidly changing dissolved oxygen concentrations within microchannels [161,171]. These devices, however, are fundamentally different from respirometers. Whereas control over dissolved oxygen concentration in a microchannel requires highly permeable polymers, microrespirometers require low permeability barriers because real-time detection of bulk analyte and the kinetic analysis of its dynamics are greatly hindered in the presence of extraneous analyte sources or sinks [161,172]. Ingress of atmospheric O_2 into the microchannel can adversely affect results, decreasing instrument sensitivities and causing non-linear responses due to the accumulation of concentration gradients and diffusion according to Fick's Law [87,88,105]. The non-linearity of steady-state R_{O2} is particularly problematic for multi-phasic processes, such as in the transition from ADP-dependent to ADP-limited respiratory states of isolated mitochondria (Figure 3.4). For example, ADP-limited respiration could be under-estimated when samples reach lower [O_2], affecting calculated parameters such as respiratory control and ADP:O ratios [93,110,173].

Excellent barrier properties of VeroClear play a critical role in preventing interference from atmospheric O_2. However, VeroClear has some O_2 buffering capacity due to a limited solubility of O_2 in the plastic. Oxygen transfer between the solution and the plastic results in small changes in the solution O_2 following rapid imposition of concentration gradient of over 200 µM. Even at the maximal gradient, the observed mass transfer was significantly slower than the R_{O2} reported elsewhere in this study. Since mass transfer is directly proportional to the difference of concentration at the boundary of the sample and all biological measurements were performed with 5 to 10 times smaller gradients, effective contribution of mass transfer is negligible. It is important to note that the maximal gradient conditions were designed to test the limits of O_2 mass transfer at the boundary and do not represent a biologically relevant model. A well-designed applied experiment should be performed at relatively constant [O_2] at physiological pO_2, including hypoxic conditions. In such cases, pre-conditioning of the MfR by gas stream or a flow of a solution is the best strategy.

The results shown in Figure 3.3A clearly demonstrated that there is no chemical O_2 scavenging by the resin itself. This shows that a small, but consistent, non-zero initial R_{O2} drift with static blank solutions (Figures 3.2A, 3.2B and 3.6A) may originate from partial retention of proteins or organelles from previous measurements. Such background drifts are much smaller than mitochondrial R_{O2} and are corrected with standard respiratory inhibition controls in differential measurements.

While reduction in the depth of the channel enhances sensitivity in adherent cell measurements, it also increases shear stress on cells during perfusion. This physiologically relevant stimulus is lacking in traditional cell culture models [172,174,175]. Physiological shear stress can range from 10^{-2} to 10^{1} dyne/cm^2 [175,176]. In the adherent MfR configuration, ARPE-19 cells experienced an estimated shear stress of 0.27 dyne/cm^2, assuming a rectangular channel of nominal dimensions, flow rate of 10 µL/min and dynamic viscosity of 0.94 cP [172,175,177]. As epithelial cells experience fluid flow velocities closer to that of the interstitium *in vivo*, the low, intermittent shear imposed by the MfR is likely comparable to physiologically relevant conditions and can be further adjusted as needed [174].

Optical transparency and O_2 barrier properties of VeroClear are ideally suited for MfR, but its biocompatibility requires further studies. Cell suspension samples are exposed to VeroClear for ≤10 min in MfR, in contrast to adherent cells which are cultured in the proximity of the polymer for many hours. We used several strategies to prevent or reduce potential cytotoxic effects. First, the cells were seeded as a tight cluster in the center of the well with glass base and polymer walls, separated from the bulk media by a seeding mask. The seeding mask was coated with polymethylmethacrylate to act as a barrier film between VeroClear and cells. This impeded mass transfer from the perimeter of the well and sequestered the cell cluster from interaction with potentially toxic leachates [116]. We have successfully cultured human epithelial (ARPE-19, Figure 3.7A) and bovine retinal endothelial cells (Figure 3.11) in the well without the use of a mask, although further investigation of cytotoxicity is needed for printed materials. During adherent cell measurements, the polystyrene matrix of the PtOEP optode is unlikely to

interfere with cellular metabolism, or suffer from bio-fouling, and provides an additional barrier against potential leaching of toxic compounds from the underlying printed polymer [116].

3D printing technology now enables the production of micron scale features in an array of polymers. High resolution and flexibility permitted the manufacture of most components with adequate precision and reproducibility without specialized tooling or casting. An alternative to 3D printing, micro-milling, creates a rougher surface that is prone to trapping air bubbles, which can affect oxygen measurements. In contrast, 3D printed parts have smooth surfaces when properly oriented with respect to the supporting plastics, improving the reproducibility of the measurements. A more powerful and flexible open shell design (Figure 3.1C) would be very difficult to implement using a traditional manufacturing techniques.

While 3D printing has been a major enabling technology for this study, yielding hundreds of chambers of varying design, methodologies can vary widely from a single prototype chip to industrial production. Common to all methodologies is the concept of an isolated microchannel with an aspect ratio amenable to bulk analyte measurement without interference from mass transfer. The Z-dimension in 3D printing typically has higher resolution than the X- and Y-dimensions and limits microchannel depths to 10's of microns [178,179]. This is sufficient for optimal MfR channel depths of 70-150 □m because shear stress scales linearly with flow rate and as the inverse square of the channel height. Further reduction of height would necessitate large reductions in flow rates to control shear of adherent cells. The increased cell aggregation would negatively affect reproducibility in suspension measurements.

3.5 Conclusion

This work describes the development of microfluidics-based respirometry for studies on biological energy transduction. Taking advantage of remote sensing in an isolated microchannel, this simple, yet versatile, method can detect O_2 consumption by minute amounts of sample, ranging from soluble enzyme systems to cell or organelle suspensions and adherent samples. We demonstrated performance of this analytical

tool in the context of eukaryotic respiration, although it can be employed for measurements of bacterial and plant metabolism. A combination of low oxygen permeability with flexible configuration allow for direct, uncompensated data acquisition, amenable for automation and development of fundamentally new experimental protocols for use in a wide array of basic and applied biomedical fields.

APPENDIX

3.6 Appendix

Polymer	Permeability (Barrer)
Reported	
Poly(dimethylsiloxane) (PDMS)	610
Polyethylene (PE)	23
Poly(tetrafluoroethylene) (PTFE)	4.2
Poly(methyl methacrylate) (PMMA)	0.09
Polyetheretherketone (PEEK)	0.13
Measured	
PEEK	0.143 ± 0.001
VeroClear	0.125 ± 0.007†
	0.218 ± 0.006‡

Figure 3.10: Oxygen permeability of selected polymers. Barrer = 10^{-10} cm^3 cm cm^{-2} s^{-1} $cmHg^{-1}$, mean ± SD (N=4). † - measured at 23° C. ‡ - measured at 37° C.

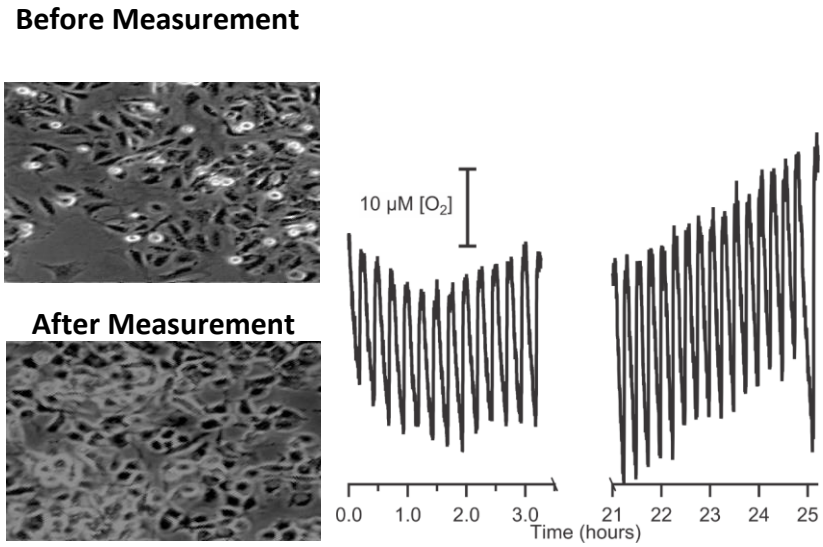

Figure 3.11. Biocompatibility of the MfR. Photomicrographs of BRECs grown on the MfR before (top) and after (bottom) ~25 hours of continuous measurement (right). The experiment was reproduced multiple times, with the continuous measurements longer than 24 hours without apparent loss of activity.

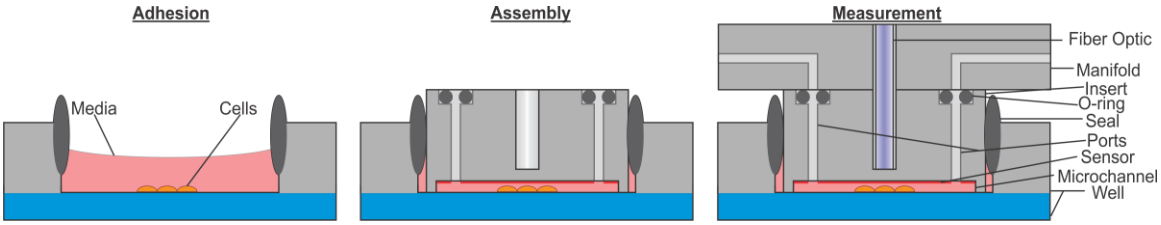

Figure 3.12. Schematic of the MfR for adherent samples. Cells are cultured on the glass base of the well, open to the incubator atmosphere (Adhesion). Assembly and Measurement refer to sequential application of MF chip and manifold immediately prior to R_{O2} determination.

Chapter 4: Mitochondrial Ceramide Effects on the Retinal Pigment Epithelium in Diabetes

4.1 Introduction

Diabetic retinopathy is the leading cause of blindness among working-age adults, representing a large socioeconomic burden on society. To date, medical and surgical treatment options have been revolutionary; however, indications for treatment rely on advanced markers of disease. Development of effective treatments for early stages of the disease require elucidation of the underlying biochemical pathophysiology.

The retina is composed of a highly ordered and bioenergetically active neural tissue, perfused by two independent vasculatures. The retinal and choroidal vessels, supplying the inner and outer retina, respectively, regulate molecular exchange across the inner and outer blood–retinal barriers. Breakdown of these barriers results in clinically observable lesions, such as microaneurysms and hemorrhages, ultimately leading to retinal hypoxia or ischemia and disease progression [59]. The inner blood–retinal barrier, consisting of non-fenestrated retinal endothelial cells and pericytes, has been the focus of many studies, but the outer barrier has received comparatively less attention [55,59,61]. The choriocapillaris, a vascular layer supplying circulation to the outer third of the retina, consists of a fenestrated endothelium separated by Bruch's membrane from the retinal pigment epithelium (RPE). The RPE provides a barrier function, with expression of tight junction proteins and regulation of transcellular water, ion, and metabolite transport by polarized expression of transporters [180,181]. Apart from regulating the osmotic and ionic balance of the outer retina, the RPE plays a key role in vision by phagocytosing shed photoreceptor outer segments and recycling retinoids for the visual cycle [180,181]. Therefore, RPE dysfunction can contribute to the hypoxic conditions common in DR, and to the fluid and ion fluxes thought to cause diabetic macular edema [22,182,183].

Diabetic retinopathy is a neurovascular complication of diabetes resulting from chronic exposure to

hyperglycemia, dyslipidemia, and inflammation. Diabetic dyslipidemia leads to changes in systemic and local lipid metabolism that drive the pro-inflammatory and pro-apoptotic cellular changes typical of diabetic retinopathy (DR) [16]. Ratios of key sphingolipid species, such as ceramide and sphingosine-1-phosphate, are a major factor in sphingolipid metabolism and play key roles in cell fate [48]. These ratios are termed a "sphingolipid rheostat" due to their importance in determining cell growth, proliferation, and apoptosis. In particular, ceramides are bioactive sphingolipid species which regulate cell stress responses [53,184]. Ceramides can be synthesized de novo from serine and palmitate or salvaged from other sphingolipid species, depending on the physiological state of the tissue [47]. Structurally, ceramide is composed of a sphingoid base and an exchangeable fatty acid. The chain length of the latter determines the biological effect of the ceramide. While short-chain ceramides (<20 carbons) are associated with pro-apoptotic effects, long-chain ceramides (>20 carbons) exert a protective effect on cells [43]. Ceramide is produced from sphingomyelin by hydrolysis of the phosphocholine head group, and the enzymes which catalyze this reaction, the sphingomyelinases, are distinguished by the pH at which they show optimum catalytic activity [47].

Acid sphingomyelinase (ASM) catalyzes sphingomyelin hydrolysis in lysosomes and at the plasma membrane, showing relative specificity for producing short-chain ceramides [54,185]. The ASM-knockout mouse has been well characterized as an animal model of Neimann Pick disease, showing remarkable resistance to cellular toxicity stemming from a variety of stressors such as hypoxia, radiation, and ischemia-reperfusion injury [52–54]. Specifically, the ASM-knockout mouse is resistant to retinal ischemia-reperfusion injury, confirming the central role of ceramide generation in the response to cell stress [54]. Studies in animal and cell culture models of DR have shown that it is the ASM, rather than the neutral SM, that is increased in the retina and retinal cells [54]. Moreover, inhibition of ceramide synthase, the central enzyme of the de novo ceramide production pathway, had no effect on cytokine-induced pro-inflammatory changes in the retina and retinal cells [55], further supporting the central role of ASM in

ceramide-mediated retinal pathology.

Reports of direct effects of ceramide on mitochondrial structure and function [46,66,71,73,186,187] prompted us to consider whether diabetes-induced ASM upregulation might lead to mitochondrial ceramide accumulation and, in turn, to structural and functional changes. Overall changes in sphingolipid levels have been documented in the diabetic retina, but elevated ceramide levels were not evident. Instead, decreases in ceramide species were compensated with increases in hexosylceramides, consistent with an increase in ceramide glycosylation in diabetes [188]. In the current study, we examine diabetes-induced changes in retinal mitochondria-specific ceramide and demonstrated that changes in mitochondrial network structure and function occur in an ASM-dependent manner, in contrast to the sphingolipid changes in the whole retina.

4.2 Methods

4.2.1 Rodents

All animal procedures complied with the National Institutes of Health (NIH) Guide for the Care and Use of Laboratory Animals. Procedures received prior approval by IACUC at Michigan State University, approval #Busik08/17-151-00, 28/08/2017.

Diabetes was induced in male Sprague–Dawley rats (237–283 g) with a single intraperitoneal injection of streptozotocin (STZ) (65 mg/kg) (Sigma Aldrich, St. Louis, MO, USA) dissolved in 100 mM citric acid (pH = 4.5) (29). Body weights and blood glucose were monitored biweekly. Blood glucose concentration was maintained in the 20 mM range. Rats were used 7 weeks after diabetes induction. C57BL/6J ASM-deficient ($ASM^{-/-}$) male mice and littermate wild-type controls at 6–8 weeks of age were used in the study.

4.2.2 Cell Culture

Primary human RPE were isolated according to standard procedures and cellular phenotype was

confirmed by staining for ZO-1 and RPE65 markers [189]. ARPE-19 (ATCC CRL-2302) cells were grown in Dulbecco's modified Eagle's medium/F12 (1:1, *v*/*v*) supplemented with 10% fetal bovine serum and 1% penicillin/streptomycin at 37 °C in 95% relative humidity and 5% CO_2. Primary human RPE cells were used at Passages 4–8.

4.2.3 Mitochondrial Isolation

Mitochondria were isolated according to previously described protocols with minor modifications [190,191]. Briefly, cells were resuspended in ice-cold mitochondrial isolation buffer (mIB) and lysed for 20 s with a Scilogex D160 homogenizer (Scilogex, Rocky Hill, USA) equipped with a 5 mm diameter probe operated at 18,000 rpm. The homogenate was brought to 30 mL with fresh mIB and centrifuged at 1000× *g* for 10 min at 4 °C. The supernatant was reserved, and the pellet was homogenized and centrifuged as above. The pooled supernatants were centrifuged at 8000× *g* for 15 min, and the mitochondrial pellet was washed with fresh mIB and subjected to further processing as indicated. Where required, half of the isolated mitochondrial sample was further purified via sucrose step-density gradient ultracentrifugation without modifications using a Sorvall M120 SE Micro-Ultracentrifuge (S55S-1155, ThermoFisher Scientific, Waltham, USA) [190].

4.2.4 Mass Spectrometry

Mitochondria on dry ice were subjected to lipid extraction with chloroform, methanol, and water as previously described [192]. Dried lipid extracts were washed with 10 mM ammonium bicarbonate solution to remove salts and buffer contaminants, and then dried under a vacuum and resuspended in methanol by normalizing volumes to total mitochondrial protein. Immediately before analysis, mitochondrial lipids were diluted 5-fold by drying aliquots in a speed-vac centrifuge and resuspending in five volumes of isopropanol/methanol/chloroform (4:2:1, *v*:*v*:*v*) containing 20 mM ammonium formate. Lipids were analyzed by high-resolution/accurate mass spectrometry and tandem mass spectrometry in positive- and

negative-ionization modes on an LTQ-Orbitrap Velos mass spectrometer (Thermo Scientific, Waltham, MA, USA) [192]. A TriVersa Nanomate (Advion, Ithaca, NY, USA) functioned as a nano-electrospray ionization source and autosampler. The nESI spray voltage was held at 2.4 kV and nESI gas pressure was 0.3 psi. The 96 well sample plate (Eppendorf, Hamburg, Germany) was held at 12 °C. Sphingolipid species were quantified as their formate adducts in negative-ionization mode against spiked synthetic sphingolipid internal standards of Cer(30:1) and SM(30:1) (Avanti Polar Lipids, Alabaster, AL, USA) at 250 femtomole/microliter [193]. Sphingolipid structures were confirmed by higher-energy collisional dissociation MS/MS in positive ionization mode. Each mass spectrum was subjected to offline mass recalibration using Thermo Xcalibur software to correct for any instrumental drift in mass calibration. Lipid peaks were subjected to isotope correction, identified, and quantified against sphingolipid internal standards using LIMSA software [194] as previously described [192].

4.2.5 Immunocytochemistry and Mitochondrial Morphology

Cells were washed three times with PBS and fixed for 15 min at room temperature with Histochoice fixative (Sigma, cat no. H2904). Cells were permeabilized with 0.1% Triton X-100 in PBS for 20 min and blocked with 1.5% BSA, 1% Tween-10 in PBS (PBST) overnight at 4 °C. Blocked samples were incubated with anti-ceramide antibody (Sigma, cat no. 8104) at a 1:100 dilution at 4 °C overnight. After three washes with PBST, cells were incubated with anti-mouse secondary antibody conjugated to Alexafluor 488 at a 1:100 dilution. Cells were counterstained with DAPI and imaged on a Nikon Eclipse TE2000 (Nikon Instruments Inc., Melville, NY, USA) equipped with a Photometrics CoolSNAP HQ2 camera (Photometrics, Tucson, AZ, USA). Fluorescence intensity was quantified with ImageJ software (version 1.53a, National Institutes of Health, Bethesda, MD, USA). For mitochondrial morphology determination, primary human RPE were grown on coverslips and stained with 50 nM MitoTracker Green at 37 °C for 30 min. After washing with PBS, cells were imaged on a Ziess LSM880 microscope (Zeiss, Oberkochen, Germany).

Mitochondrial length, as a marker of fragmentation, was determined by measuring the major axis of individual mitochondria in a 5 × 5 μm square from a randomly selected cell in the field of view. Five cells from three fields of view were selected from each sample to represent the cellular population. 3D animations of the z-stacked images were created use the 3D projection command in ImageJ, setting layer height to 0.17 μm and a full 360° rotation.

4.2.6 Quantitative Real-Time Polymerase Chain Reaction

Total cellular RNA extraction and RT-PCR were performed as previously described [54]. Human gene-specific primers for acid sphingomyelinase, interleukin 1β (IL-1β), interleukin 6 (IL-6), intercellular adhesion molecule (ICAM1), and vascular endothelial growth factor (VEGF) were used to measure gene expression. Results were normalized to cyclophilin A.

4.2.7 Western Blot Analysis

Protein extraction and Western blots were carried out using the NuPAGE system as previously described [55]. Fractions of mitochondrial isolates were normalized by suspension volume and quantitated relative to voltage-dependent anion channel (VDAC) intensity. Primary antibodies against LAMP-1 (SC-20011, Santa Cruz, Dallas, TX, USA), VDAC (PAI-954A, Invitrogen, Waltham, MA, USA), and ASM were used at 1:1000 dilution. Anti-ASM antibody was a generous gift from Richard Kolesnick. Secondary antibodies against rabbit IgG (926-68073, Odyssey, Lincoln, NE, USA) and mouse IgG (610-731-124, Rockland Immunochemicals, Limerick, PA, USA) were used at 1:10,000 dilution. Bands were imaged on a LiCor Odyssey imaging system. Densitometric analysis was performed in ImageJ software after splitting the RGB image into individual channels and a background subtraction using a rolling ball radius of 16.3 pixels.

4.2.8 Citrate Synthase Activity

Enzymatic activity was measured using a citrate synthase activity assay kit (Sigma, cat no. CS0720) per the manufacturer's instructions using a 96 well plate. Citrate synthase activity was normalized to total protein content, measured using the Bradford assay (BioRad, Hercules, CA, USA).

4.2.9 Microrespirometry

Cellular respirometry was measured as previously described [195]. Briefly, cells were seeded on-chip at a density of 860 cells/mm^2 and cultured overnight under standard cell culture conditions at 37 °C, 95% relative humidity, 5% CO_2. Microrespirometer chips were assembled immediately before the measurement and the cells were perfused with the basal respiration buffer, which consisted of DPBS with calcium and magnesium supplemented with 10 mM glucose, 10 mM lactate, 1 mM pyruvate, and 0.2% bovine serum albumin. Respiratory control ratio [77] was determined from sequential respiration measurements in the leak buffer, consisted of respiration buffer supplemented with 2.5 µM oligomycin, and the uncoupling buffer, consisted of leak buffer supplemented with 5 µM carbonyl cyanide m-chlorophenylhydrazone (CCCP). Measurements in inhibition buffer, consisting of uncoupling buffer supplemented with 5 mM potassium cyanide, were used for correction of non-respiratory oxygen consumption. Perfusion was controlled using a syringe infusion pump (KD Scientific, Holliston, MA, USA) operating at a flow rate of 10 µL/min at room temperature. Activity determinations were performed under stationary buffer conditions for 5–10 min, maintaining oxygen concentrations above 150 µM.

4.3 Results

4.3.1 Diabetes Results in Retinal Mitochondrial Ceramide Accumulation

We used an streptozotocin (STZ)-induced diabetic rat model to determine whether upregulation of ASM expression and activity in cells comprising the inner and outer blood–retinal barriers (BRBs) [54]

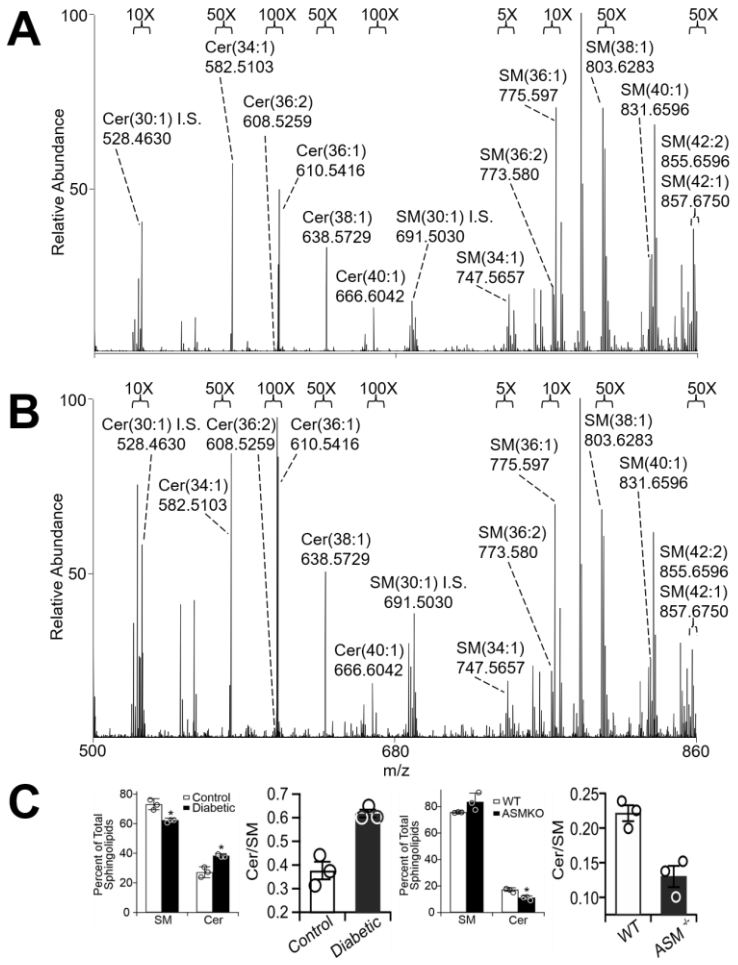

Figure 4.1. Negative-ion high-resolution/accurate mass spectrometric quantification of sphingolipids in retinal mitochondria. Mass spectra of control (**A**) and diabetic (**B**) rat retinal mitochondrial sphingolipids after 7 weeks of diabetes. Full-scan MS spectra are shown from mitochondrial lipids analyzed by negative-ionization mode direct-infusion nano-ESI mass spectrometry. Sphingolipids are shown under magnifications indicated at the top of each panel. Abundant non-labeled peaks correspond to phospholipids. "I.S." indicates internal standards. (**C**) Quantification of total sphingomyelin (SM), ceramide (Cer), and the Cer/SM ratio based on mass spectrometry analysis of mitochondria from control and diabetic rat retinas (left panel), and wild type (WT) and acid sphingomyelinase knock out (ASMKO) mouse retinas (right panel). * $p < 0.05$, $n = 3$.

contributed to the mitochondrial ceramide accumulation that further leads to cell damage [196]. Mitochondria were isolated from control and diabetic rat retinas using differential centrifugation protocols, followed by lipid extraction using chloroform, methanol, and water [192] and Orbitrap high-resolution/accurate mass mass spectrometry (MS) and MS/MS analysis. Samples were normalized based

on total mitochondrial protein, and sphin-golipid peaks were compared to synthetic sphingolipid internal standards incorporated in each run. As presented in Figure 4.1A,B, diabetes resulted in a decrease in endogenous levels of mito-chondrial ceramide and sphin-gomyelin, consistent with previous reports [188].

To quantify changes in sphingolipid composition, total detected sphin-golipid abundances were summed, and sphingolipid species were expressed as a percentage of total sphingolipids. This approach revealed significant increases in relative ceramide levels and decreases in the relative sphingomyelin levels in retinal mitochondria isolated from STZ-induced diabetic rat retinas (7-week duration) compared to controls (Figure 4.1C, left). To test the role of ASM in the control of mitochondrial ceramide more directly, sphingolipid profiles of mitochondria prepared from ASM-knockout mice were similarly analyzed. In contrast to the diabetes-induced increase in the ceramide-to-sphingomyelin ratio, depletion of ASM resulted in lower relative levels of ceramide versus sphingomyelin compared to wild-type controls (Figure 4.1C, right), confirming that ASM plays an important role in mitochondrial sphingolipid dynamics.

4.3.2 Diabetes Results in Pro-Inflammatory Changes in Human Retinal Pigment Epithelial (RPE) Cells

Whole-retina preparations, as shown in Figure 4.1, lack the RPE layer, a site of diabetes-induced ASM upregulation [54]. We therefore sought to determine sep-arately whether RPE cells demonstrated similar diabetes-induced changes.

Results of fluorescent ceramide staining in control- and diabetic-derived cultured human RPE cells are presented in Figure 4.2A and demonstrated an average 2.7-fold increase in cellular ceramide staining of diabetic-derived RPE cells compared to controls (Figure 4.2B). Analysis of inflammatory gene expression in the same cells showed significant increases in IL1β and IL6, and a trend toward increased ASM expression in diabetic-derived RPE cells compared to controls (Figure 4.2C), which was consistent with the

increases in ceramide observed by immunohistochemistry. Furthermore, *in vitro* treatment of control-derived RPE cells with 25 mM glucose for 72 h led to significant increases in ASM, VEGF, and ICAM1 mRNA compared to untreated control-derived RPE cells (Figure 4.2D), supporting their roles in hyperglycemic response.

4.3.3 Diabetes Results in Mitochondrial Fragmentation in Human RPE Cells

As mitochondria are known to accumulate ceramide [63], and we demonstrated that diabetes changes the ceramide-to-sphingomyelin ratio in retinal mitochondria (Figure 4.1), we next sought to determine whether structural and functional changes could be detected in mitochondria isolated from control- or diabetic-derived RPE cells. Figure 4.3A demonstrates staining with MitoTracker Green, used to reveal the expected reticular mitochondrial network in the control RPE cells. This network appeared to be disrupted in the diabetic-derived RPE cells, which had predominantly round and fragmented mitochondria. Quantitation of morphological features revealed that the average mitochondrial length in diabetic-

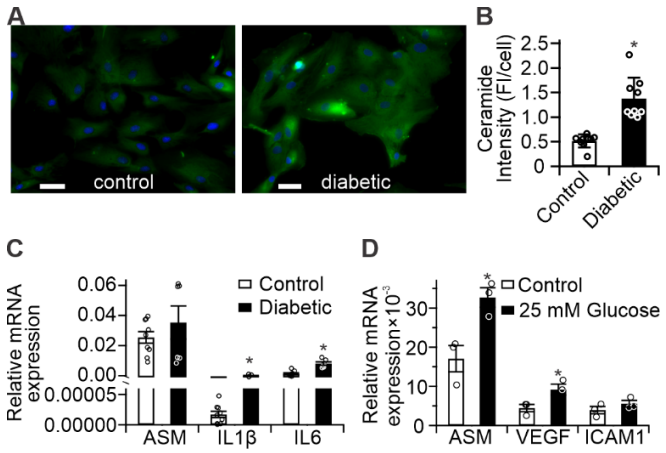

Figure 4.2. Diabetes-induced pro-inflammatory changes in human RPE (**A**) Representative images of control- and diabetic-derived retinal pigment epithelial (RPE) cells showing ceramide (green) and nuclear staining (blue). Scale bars = 50 µm; (**B**) Quantitation of ceramide-staining fluorescence intensity from panel (A). n = 9, error bars = S.D., * $p < 0.05$; (**C**) Inflammatory gene expression in diabetic-derived RPE (black bars) compared to control (white bars); (**D**) Upregulation of inflammatory gene expression in control RPE treated with 25 mM glucose for 72 h (black bars) compared to untreated cells (white bars). * $p < 0.01$, n = 6.

derived RPE cells was 1.2 ± 0.57 µm (*n* = 3), whereas control-derived RPE cells' mitochondria were 3.4 ± 0.78 µm (*n* = 3) in length, (Figure 4.3B).

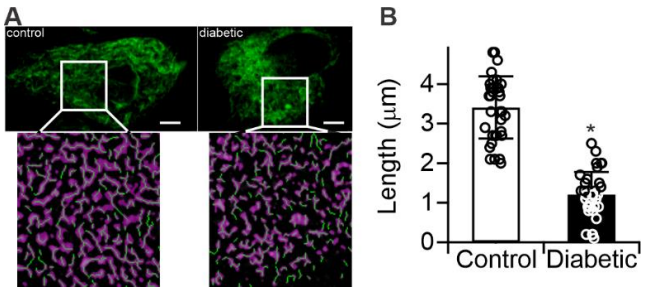

Figure 4.3. Structural analysis of human RPE mitochondria. (**A**) Mitochondrial morphology determined by MitoTracker Green staining of control- and diabetic-derived RPE. Inset = skeletonized (green lines) binary mask (purple) of deconvoluted photomicrographs highlighting mitochondrial morphology. Scale bars = 5 µm; (**B**) Quantitation of average mitochondrial length. *n* = 3, * $p < 0.05$.

4.3.4 Diabetes Induces Acid Sphingomyelinase (ASM)-Mediated Changes in Mitochondrial Function of Human RPE Cells

To determine whether the structural changes of mitochondria were correlated with detectable functional differences, we used micro-respirometry to examine oxidative phosphorylation in control- and diabetic-derived RPE cells [195]. In this approach, the flow of oxygenated medium over adherent cells is intermittently stopped and respiration leads to a steady consumption of oxygen, seen as periodic downward slopes in the O_2 concentration traces (Figure 4.4A). Ensuing resumption of flow reoxygenates the sample and the measurement is repeated. Following growth to confluency, RPE cells were transferred into the micro-respirometer and perfused with a medium containing glucose, lactate, and pyruvate as substrates, supplemented with the ATP-synthase inhibitor oligomycin (Figure 4.4A, leak). Respiratory activity in this state is limited by a high proton motive force and predominantly represents proton leakage through the inner mitochondrial membrane [81]. No substantial differences between sample groups were observed in this state, suggesting a lack of diabetes-induced changes to inner mitochondrial membrane

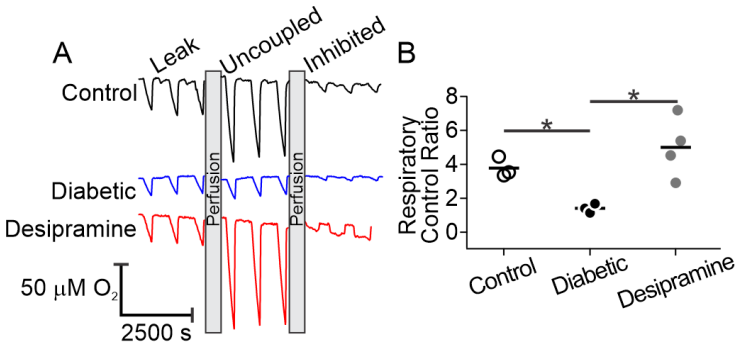

Figure 4.4. Microrespirometric analysis of human RPE cells. (**A**) Representative oxygen concentration traces of control (black), diabetic (blue), and desipramine-pretreated diabetic (red) RPE cells. Respirometry was performed in the presence of oligomycin (leak), carbonyl cyanide m-chlorophenylhydrazone (CCCP, uncoupled), and potassium cyanide (KCN, inhibited). (**B**) Respiratory control ratios of control (white circles), diabetic (black circles), and desipramine-pretreated diabetic groups (gray circles). * $p < 0.05$, $n = 3–4$.

proton permeability. Next, the maximal respiratory rate was assessed by dissipation of the proton motive force with the chemical uncoupler, carbonyl cyanide m-chlorophenylhydrazone (CCCP, uncoupled). In this state, control over respiration is shifted to substrate delivery pathways and innate turnover capacity of the electron transport chain. Dissipation of the proton motive force with CCCP resulted in an increase in oxygen consumption rates of RPE cells over that observed with oligomycin alone. While the expected increase in respiration due to uncoupling was observed in control RPE cells and in diabetic cells with desipramine pretreatment, little response to the uncoupler was observed in the diabetic cells without desipramine pretreatment. The latter observation indicated that mitochondria in resting diabetic RPE cells operate close to the maximal respiratory activity, which is limited by electron transport chain turnover or substrate delivery. Subsequent perfusion with potassium cyanide resulted in complete inhibition of mitochondria-dependent oxygen consumption, evident in all experimental groups and used to correct for non-mitochondrial oxygen-consuming processes. The relative changes in the oxygen consumption between three conditions were used to calculate a respiratory control ratio (RCR, Equation (1)), a quantitative measure of mitochondrial fitness [77].

$$Respiratory\ Control\ Ratio\ (RCR) = \frac{(Oligomycin + \ CCCP)_{OCR} - (KCN)_{OCR}}{(Oligomycin)_{OCR} - (KCN)_{OCR}} \quad (1)$$

As shown in Figure 4.4B, diabetic-derived RPE cells displayed a significantly decreased RCR compared to control-derived RPE cells (1.41 ± 0.27 vs. 3.78 ± 0.59). This difference was abolished by perfusion of diabetic-derived RPE cells with 15 µM desipramine, an ASM inhibitor, [197,198] for 1 h, which increased the RCR to 5.00 ± 1.78.

4.3.5 Mitochondrial ASM Contributes to Impaired Mitochondrial Function In Vitro

Accumulation of ceramide at the expense of sphingomyelin with concomitant change in ceramide/sphingomyelin ratio (see above) suggests that it is the result of sphingomyelin hydrolysis, a reaction catalyzed by ASM. This raises the question of whether ceramide accumulation in mitochondria is due to the activity of mitochondrial ASM or to the transport of ceramide from remote sites. The presence of intrinsic ASM in mitochondrial membranes is demonstrated in Figure 4.5. In addition to mitochondria, ASM is known to be present in the lysosomes and the plasma membrane. Although a high degree of separation between the mitochondrial and plasma membrane fractions is easily achievable by standard methodology, the lysosomes and mitochondria and are much harder to separate due to very similar size, shape, and density characteristics [191,199–201]. To conclusively localize ASM to mitochondrial membranes, we obtained mitochondrial preparations with increasing levels of purity from human RPE cells and subjected them to immunoblotting for (i) ASM; (ii) the mitochondrial outer membrane marker voltage-dependent anion channel (VDAC); and (iii) the lysosomal membrane marker lysosomal-associated membrane protein 1 (LAMP-1). As shown in Figure 4.5A, mitochondria prepared by standard differential centrifugation protocols showed the presence of VDAC and LAMP-1 (crude), indicating co-purification of lysosomes in mitochondrial preparations. However, further purification by successive centrifugations at 8000× *g* (pure) resulted in significant depletion of the lysosomal marker LAMP-1 relative to the

mitochondrial marker VDAC. Each fraction was sampled at varying concentrations, ensuring fidelity of optical density quantitation, which revealed that extra purification yielded a two-fold depletion of LAMP-1 (Figure 4.5B, left panel). The same samples were then probed for the level of ASM, which is known to localize to the lysosome. If most of the ASM shown in Figure 4.5 originated from the lysosomal compartment, the ratio of ASM to VDAC would follow that of LAMP-1. The experimental results demonstrated only a small ASM depletion in the purified mitochondrial sample, and optical density quantitation revealed an apparent enrich-ment of ASM when normalized to VDAC density (Figure 4.5B, right panel).

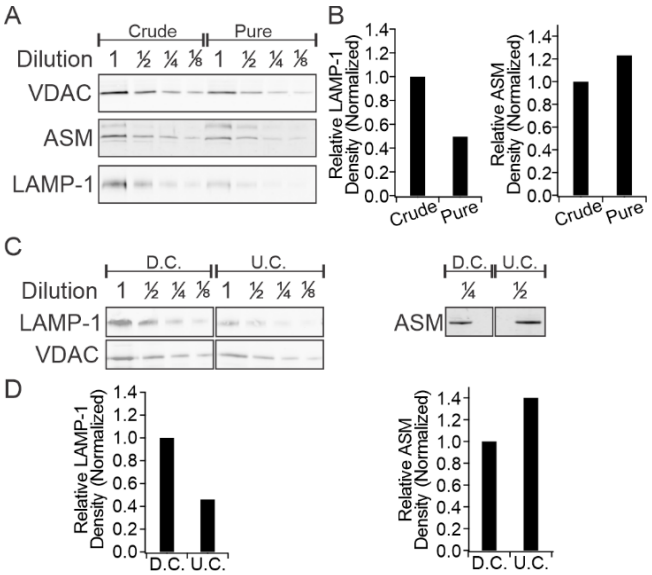

Figure 4.5. Colocalization between ASM and mitochondrial markers. (**A**) Western blot analysis of human RPE cell mitochondria at varying levels of purity and (**B**) associated optical density quantitation; (**C**) Western blot analysis of ARPE-19 cell mitochondria at varying purity levels and associated optical density quantitation (**D**). LAMP-1 = lysosome associated membrane protein 1, VDAC = voltage dependent anion channel, crude = one 8000×*g* centrifugation, pure = three 8000×*g* centrifugations, D.C. = differential centrifugation, U.C. = sucrose step-density ultracentrifugation.

These results were replicated in mitochondria isolated from ARPE-19 using a similar protocol (Figures 4.5C). In this case, the mitochondrial fractions were examined by immunoblotting after initial differential centrifugation (D.C.) and again after a second sucrose-step density

ultracentrifugation (U.C.). Consistent with the results from the human RPE cells (Figure 4.5B), the ultracentrifugation resulted in a two-fold depletion of LAMP-1 normalized to VDAC (Figure 4.5D, left panel) compared to the differential centrifugation preparation of mitochondria. ASM enrichment was also observed after ultracentrifugation when normalized to VDAC in ARPE-19 samples (Figure 4.5D, right panel).

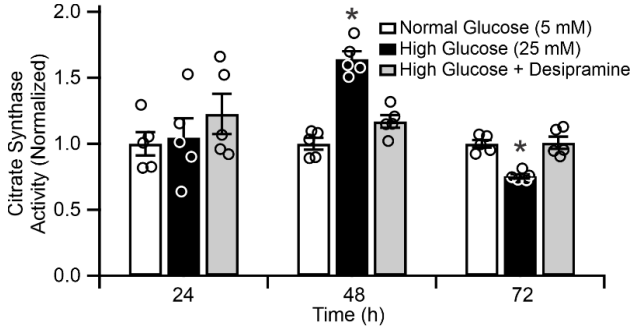

Figure 4.6. Citrate synthase activity in ARPE-19 cells. White bars = control cells, black bars = 25 mM glucose-treated cells, gray bars = 25 mM glucose-treated cells with daily 1 h treatment with 15 µM desipramine. * $p < 0.05$, $n = 5$.

To examine the consequences of increased mitochondrial ASM expression and the resulting mitochondrial ceramide accumulation, we assessed changes in citrate synthase activity in response to high glucose treatment of ARPE-19 (Figure 4.6). Citrate synthase resides exclusively in the mitochondrial matrix and catalyzes the condensation of acetyl-CoA and oxaloacetate to citrate, in the first step of the tricarboxylic acid cycle. As such, it is widely used as a mitochondrial content marker [202].

The effect of glucose concentration on citrate synthase activity in ARPE-19 cells is presented in Figure 4.6. No statistically significant effect of high glucose was observed after 24 h ($n = 5$, $p > 0.05$). At 48 h, the 25 mM glucose treatment increased citrate synthase activity to 164.3% ± 5.8% vs. 5.5 mM glucose control, followed by the reduction in activity to 75% ± 1.6% of the control at 72 h ($p < 0.05$, $n = 5$). To evaluate whether these glucose-induced changes in citrate synthase activity was mediated by ASM, parallel measurements were conducted on ARPE-19 cells incubated in high-glucose conditions with daily, intermittent treatments with 15 µM desipramine. These treatments abolished the biphasic

hyperglycemia-induced response in citrate synthase activity, and the desipramine-treated group displayed a time profile closely corresponding to that of the control group ($p > 0.05$, $n = 5$).

4.4 Discussion

Diabetes is a multifactorial pathological process resulting in micro- and macrovascular complications. Diabetic retinopathy is a common microvascular complication of diabetes, which results from hyperglycemia, dyslipidemia, and chronic inflammatory changes in the retina leading to blood–retinal barrier breakdown and disease progression [203]. Diabetic dyslipidemia results in both systemic and local changes to lipid metabolism and, in the retina, contributes to the pro-apoptotic changes seen in the inner and outer blood–retinal barrier cellular components [16].

We previously demonstrated that diabetes leads to enhanced ASM expression predominantly in retinal endothelial- and retinal pigment epithelial cells [54] suggesting that sphingomyelin hydrolysis is the primary cause of cellular ceramide accumulation. Despite these findings, measurements of sphingolipid composition in diabetic rodent retinas revealed that ceramide levels are, in fact, decreased whereas glucosylceramides are increased [188]. Such results suggest hyperglycemia-induced diversion of ceramide toward the glycosylated forms in total retinal sphingolipid pools. The increased glycosylation in the diabetic retina was attributed to increases in uridine diphosphate glucose (UDP-glucose) production through the pentose phosphate pathway, rather than changes in enzymatic activity. As the pentose phosphate pathway occurs in the cytoplasm, we argue that an increase in glucosylceramide production due to higher UDP-glucose availability would be limited to the cytoplasm, rather than the mitochondria. In contrast to whole-retina sphingolipid measurements, we show in Figure 4.1A that diabetes-induced increases in relative ceramide levels can be detected in mitochondria after subcellular fractionation of whole retina. Similarly, mitochondria isolated from the retinas of ASM-knockout animals displayed an inversion of the ceramide-to-sphingomyelin ratio (Figure 4.1B), demonstrating the direct connection

between ASM activity and mitochondrial ceramide accumulation. It is worth mentioning that the degree of these changes in the barrier cells was likely underestimated because the major component of the mitochondrial preparations from whole retina originate from photoreceptors. Diabetes-induced increase in ASM expression and activity is the highest in the cells that make up the BRB, namely REC and RPE cells [54,55,185]. Smaller changes are observed in the Muller cells and microglia, and no changes are seen in the photoreceptors [54]. The changes in the whole-retina mitochondria preparations were thus diluted by the large population of the non-changing photoreceptor mitochondria and by the mitochondrial ceramide from endothelial, Muller, and microglia cells, which shows smaller changes.

Here, we focused on the role of ASM-dependent sphingomyelin hydrolysis in barrier cells. ASM-dependent mitochondrial ceramide accumulation is strongly supported by our present finding that a population of cellular ASM can be localized to mitochondrial membranes in RPE cells (Figure 4.5). These results are consistent with our previous reports that diabetes-induced ASM upregulation is a key player in blood–retinal barrier breakdown and provide evidence for a proposed mechanism of metabolic dysfunction in retinal cells mediated by the accumulation of cellular ceramide. Although our results support the role of mitochondrial ASM in the observed changes, we cannot presently rule out the contributions of alternative pathways, such as neutral-sphingomyelinase- and/or reverse-ceramidase-mediated mitochondrial ceramide generation, as described in other systems [63,196]. Our previous data show that neutral sphingomyelinase expression does not change in the diabetic retina [54], and that inhibition of ceramide synthase has no effect on cytokine-induced pro-inflammatory changes in the retina and retinal cells [55]. In combination with the sensitivity of both the diabetes-induced changes in RCR and citrate synthase to desipramine reported here, we strongly argue that ASM plays a key role in RPE cell mitochondrial dysfunction. Alternatively, stress-induced production and transport of ceramide to mitochondria from distal sites has also been reported [204].

In this work we focused on the RPE cells, a cellular component of the outer blood–retinal barrier. As RPE cells were not a part of the whole-retina preparations, we examined mitochondria from the control and diabetic donors RPE cells separately from the whole-retina mitochondria. Human RPE cell culture could be used due to a well-known metabolic memory legacy effect. Metabolic memory was first described in diabetic patients as a prolonged effect of early glycemic control on the development of diabetic complications, even after glycemic control is established later in the course of disease progression [205]. The metabolic memory phenomenon is well accepted in the field of diabetic complications [205–208]. The molecular mechanisms underpinning sustained metabolic memory are not fully understood. Recent work, however, has demonstrated that epigenetic modifications to mtDNA mismatch-repair machinery result in decreased transcript levels, decreased mitochondrial localization, and accumulation of mtDNA mutations [38]. As mtDNA is particularly vulnerable to ROS-induced DNA mutations, decreased functioning of repair machinery results in accumulation of damaged oxidative phosphorylation complexes and, ultimately, impairment of oxidative phosphorylation as a whole [39]. As these changes accumulate over time, they perpetuate a vicious cycle of oxidative stress and sustained inflammatory changes, leading to the progression of diabetic complications despite correction of diabetic hyperglycemia.

These effects have been shown to occur in animal models as well as in cell culture models. Cells isolated from diabetic donor retinas or animal models retain their diabetic metabolic phenotype for several passages [205–210]. Human control and diabetic donor cells were previously shown to display metabolic memory characteristics right after the isolation and for up to eight passages [205]. Dysfunction of these cells is implicated in the development of diabetic macular edema and they represent a site of significant diabetes-induced ASM upregulation [22,54]. Despite culturing control- and diabetic-derived RPE cells under identical, euglycemic, conditions, we detected increased ceramide and inflammatory gene expression in diabetic-derived RPE cells compared to controls (Figure 4.2). Furthermore, we showed that control-derived RPE cells retained their sensitivity to the diabetic milieu, as high-glucose treatment

resulted in enhanced inflammatory gene expression (Figure 4.2D). Accompanying these changes, diabetic-derived RPE cells displayed fragmented mitochondria and impaired mitochondrial-dependent metabolism (Figures 4.3 and 4.4). These results support the metabolic memory hypothesis, implying that diabetes induces permanent changes to cellular metabolism in the long term, despite achievement of a euglycemic state.

Our results are consistent with previous reports detailing diabetes-induced mitochondrial fragmentation and impaired oxidative phosphorylation in retinal endothelial cells [211], although mitochondrial fragmentation alone is insufficient to universally predict dysfunctional metabolism. The observation of diabetes-induced mitochondrial fragmentation was rationalized by the critical finding of functional changes to oxidative phosphorylation (Figures 4.3, 4.4, and 4.6). Citrate synthase is a marker of mitochondrial content and its activity parallels electron transport chain capacity of the cell [202]. Steady-state mitochondrial content, however, is controlled by the relative flux of mitochondrial biogenesis and mitophagy which are, in turn, related to mitochondrial fission and fusion dynamics. This quality-control mechanism is useful to clear bioenergetically dysfunctional mitochondria by fission and subsequent mitophagy. It ensures a steady-state population of robust mitochondria capable of sustaining ATP synthesis rates over a wide range of metabolic demands. Indeed, diabetes-induced increases in mitophagy have been described in RPE cells with increased mitophagic flux attributed to ROS-dependent mitochondrial damage [58,212]. Our observations of diabetes-induced oxidative phosphorylation dysfunction (Figure 4.4), likely followed mitochondrial fragmentation (Figure 4.3), rationalize earlier reports of the increased mitophagic flux. Our data showed that diabetes-induced ASM upregulation led to an accumulation of ceramide in mitochondrial membranes that limits the maximal metabolic capacity of the respiratory chain. Combined with excessive electron supply from glucose and adequate oxygenation in the hyperglycemic stage of the diabetes, such a restriction stimulates ROS production. This metabolic insult then leads to the production of dysfunctional mitochondria, which stimulates the

mitophagy pathway and, under continuously elevated ASM levels, results in a steady population of fragmented and bioenergetically impaired mitochondria in RPE cells.

Our current finding that desipramine treatment can rescue functional (RCR, Figure 4.4) and mitochondrial mass (Figure 4.6) changes in diabetic-derived RPE cells demonstrates that ASM-dependent ceramide metabolism plays a central role in diabetes-induced mitochondrial damage. Desipramine belongs to a class of antidepressants known as tricyclic amines which are functional inhibitors of ASM activity [197,198]. Although there are reports that at a high dose, desipramine can also interact with mitochondrial proteins directly, leading to impaired NADH oxidation, electron transport, and ATP synthase activity [213], these effects were not observed at the low dosage (15 μM) and short treatment time (1 h daily) use in this study. Indeed, our results showed no changes of the basal rate (Figure 4.7) and substantial enhancement of the maximal oxidative phosphorylation function, which were not consistent with direct effects of desipramine on mitochondrial oxidative phosphorylation machinery. The observed changes rather support the effect of desipramine via inhibition of ASM activity, leading to the depletion of mitochondrial ceramide, reversing its inhibitory effect on the oxidative phosphorylation and increasing RCR, as described here.

As a gross measure of mitochondrial fitness, the whole-cell RCR is sensitive to a range of metabolic processes including substrate delivery, maximal electron transport chain capacity, proton leakage, and outer mitochondrial membrane integrity [77,123]. A greater than two-fold decrease in the whole-cell RCR of diabetic-derived RPE cells suggests substantial impairment of oxidative phosphorylation with a concomitant decrease in mitochondrial ATP-synthesis capacity and increase in mitochondrial ROS generation. It is remarkable that the mitochondrial functional impairment was retained despite culturing the cells for several generations under standard, euglycemic conditions. Whether the diabetes-induced RCR changes arise from direct inhibition of substrate delivery, electron transport, or the phosphorylation system, such as direct ceramide inhibition of Complex III or ceramide-mediated formation of outer

mitochondrial membrane pores [71,73,186,187], is the subject of ongoing research. The sensitivity of diabetic-derived RPE cells to desipramine strongly suggests ASM-mediated ceramide inhibition of oxidative phosphorylation. Depletion of mitochondrial ceramide upon ASM inhibition, therefore, would reverse these effects, reduce oxidative stress, and favor retention of a robust mitochondrial population, as we saw in this work (Figures 4.4 and 4.6).

Chapter 5: Conclusions and Future Directions

5.1 Conclusions and Future Directions

Respirometry is a powerful tool that is well suited as a screen for potential metabolic derangements and to perform highly detailed studies on specific segments of oxidative metabolism. Development of a flow-through microrespirometer, as described in Chapter 3, enables bioenergetic characterizations of a variety of biological samples by significantly increasing sensitivity, permitting varied sample preparations, integrating into standard cell culture practices, and by executing novel experimental protocols. Despite these advantages, data presented in Chapter 3 indicate that cell suspension measurements suffer from large variances. As these variances were attributed to handling of dense cell suspensions and sedimentation of cells along the inlet and microchannel during loading, implementation of flow focusing can be explored to remediate these effects. Additionally, multiplexing the oxygen sensing with reactive oxygen species quantitations and/or in-line glucose sensors can yield complementary information about diabetes-induced metabolic changes in whole cells or tissues.

The data presented in Chapter 4 show that diabetic-derived retinal pigment epithelial cells display a significantly decreased respiratory control ratios compared to control-derived cells, suggesting that diabetes results in derangements in oxidative metabolism. These changes are additionally sensitive to the acid sphingomyelinase inhibitor desipramine, suggesting that acid sphingomyelinase-dependent mitochondrial ceramide accumulation impairs oxidative metabolism. Ceramides are well known pro-apoptotic sphingolipids and have been reported to inhibit complex III activity and induce mitochondrial outer membrane permeabilization (see Chapter 1).

Application of the concepts described in Chapter 2 to these results will aid in localizing the functional consequences of acid-sphingomyelinase-dependent mitochondrial ceramide generation. Proceeding with this model system would therefore involve plasma membrane permeabilization of cell culture monolayers

with subsequent assessment for exogenous cytochrome *c* sensitivity and maximal ETC turnover. Results of these studies can resolve ceramide-mediated inhibition of ETC from induction of cytochrome *c* release. Decreases in maximal ETC turnover suggest flux limitations upstream of the pmf, including complex III as a candidate, whereas exogenous cytochrome *c* sensitivity suggests an increasing population of apoptotic cells in treatment conditions. Flux limitations in ETC turnover can then be further probed to determine complex- or substrate-specific respiratory rates to localize the metabolic dysfunction, as described in Chapter 2.

Complementary to the functional studies, assessment of diabetes-induced mitochondrial fragmentation (Chapter 4) in the presence of ASMase inhibition can be used to show downstream effects of ASMase-induced mitochondrial dysfunction. Ceramide accumulation can play a role in ROS generation, through ETC inhibition, or in mitochondrial fission due to its role in regulation of membrane biophysical properties. Reports of mitochondrial fragmentation and increased flux through mitophagy suggest that diabetes-induced mitochondrial dysfunction stimulates organelle removal pathways and ceramides may play a significant role in the process.

Finally, localization of ASMase to mitochondrial membranes by immunoblotting is also reported in Chapter 4. Similar localization patterns were seen using primary cells and ARPE-19, a cell line, strongly suggesting that a portion of ASMase is localized to mitochondria. To extend these results, quantitative assays for ASMase activity can confirm presence of active ASMase in mitochondria and further to probe for treatment-induced changes to mitochondrial ASMase activity. Electron microscopy can help confirm localization to mitochondrial membranes and reveal whether the detected ASMase localizes to intra-organelle contact points.

REFERENCES

REFERENCES

1. *Diabetes 2014 Report Card*; 2014;

2. *National Diabetes Statistics Report*; Atlanta, 2020;

3. Chen, R.; Ovbiagele, B.; Feng, W. Diabetes and Stroke: Epidemiology, Pathophysiology, Pharmaceuticals and Outcomes. *Am. J. Med. Sci.* **2016**, *351*, 380–386, doi:10.1016/j.physbeh.2017.03.040.

4. Fong, D.S.; Aiello, L.P.; Ferris, F.L.; Klein, R. Diabetic retinopathy. *Diabetes Care* **2004**, *27*, 2540–2553, doi:10.2337/diacare.27.10.2540.

5. Cheung, N.; Mitchell, P.; Wong, T.Y. Diabetic Retinopathy. *Lancet* **2010**, *376*, 124–136, doi:10.1016/S0140-6736(09)62124-3.

6. Bhavsar, A.R. Diabetic Retinopathy 2019.

7. Solomon, S.D.; Chew, E.; Duh, E.J.; Sobrin, L.; Sun, J.K.; VanderBeek, B.L.; Wykoff, C.C.; Gardner, T.W. Diabetic retinopathy: A position statement by the American Diabetes Association. *Diabetes Care* **2017**, *40*, 412–418, doi:10.2337/dc16-2641.

8. Wright, A.D.; Dodson, P.M. Medical management of diabetic retinopathy: fenofibrate and ACCORD Eye studies. *Eye* **2011**, *25*, 843–9, doi:10.1038/eye.2011.62.

9. Simó, R.; Hernández, C. Prevention and treatment of diabetic retinopathy: evidence from large, randomized trials. The emerging role of fenofibrate. *Rev. Recent Clin. Trials* **2012**, *7*, 71–80.

10. Nabulsi, A.; Folsom, A.; White, A.; Patsch, W.; Heiss, G.; Wu, K.; Szklo, M. The Effect of Intensive Treatment of Diabetes on the Development and Progression of Long-Term Complications in Insulin-Dependent Diabetes Mellitus. *N. Engl. J. Med.* **1993**, *328*, 1069–1075.

11. Lyons, T.J.; Jenkins, A.J.; Zheng, D.; Lackland, D.T.; McGee, D.; Garvey, W.T.; Klein, R.L. Diabetic retinopathy and serum lipoprotein subclasses in the DCCT/EDIC cohort. *Invest. Ophthalmol. Vis. Sci.* **2004**, *45*, 910–8.

12. Keech, A.; Mitchell, P.; Summanen, P.; O'Day, J.; Davis, T.; Moffitt, M.; Taskinen, M.R.; Simes, R.; Tse, D.; Williamson, E.; et al. Effect of fenofibrate on the need for laser treatment for diabetic retinopathy (FIELD study): a randomised controlled trial. *Lancet* **2007**, *370*, 1687–1697, doi:10.1016/S0140-6736(07)61607-9.

13. Group, A. to C.C.R. in D. (ACCORD) S. Effects of Intensive Glucose Lowering in Type 2 Diabetes. *N. Engl. J. Med.* **2008**, *358*, 225–237.

14. Baldeweg, S.E.; Yudkin, J.S. Implications of the United Kingdom prospective diabetes study. *Diabetes Journals* **2002**, *25*, doi:10.1016/S0095-4543(05)70132-9.

15. Nathan, D.M. The diabetes control and complications trial/epidemiology of diabetes interventions and complications study at 30 years: Overview. *Diabetes Care* **2014**, *37*, 9–16, doi:10.2337/dc13-2112.

16. Hammer, S.S.; Busik, J. V. The role of dyslipidemia in diabetic retinopathy. *Vision Res.* **2017**, *139*, 228–236, doi:10.1016/j.visres.2017.04.010.

17. Rübsam, A.; Parikh, S.; Fort, P.E. Role of inflammation in diabetic retinopathy. *Int. J. Mol. Sci.* **2018**, *19*, 1–31, doi:10.3390/ijms19040942.

18. Chew, E.Y.; Davis, M.D.; Danis, R.P.; Lovato, J.F.; Perdue, L.H.; Greven, C.; Genuth, S.; Goff, D.C.; Leiter, L.A.; Ismail-beigi, F.; et al. The Effects of Medical Management on the Progression of Diabetic Retinopathy in Persons with Type 2 Diabetes: The ACCORD Eye Study. *Ophthalmology* **2014**, *121*, 2443–2451, doi:10.1016/j.ophtha.2014.07.019.The.

19. Preliminary Report on Effects of Photocoagulation Therapy. *Am. J. Ophthalmol.* **1976**, *81*, 383–396, doi:10.1016/0002-9394(76)90292-0.

20. Early Photocoagulation for Diabetic Retinopathy: ETDRS Report Number 9. *Ophthalmology* **1991**, *98*, 766–785, doi:10.1016/S0161-6420(13)38011-7.

21. Deschler, E.K.; Sun, J.K.; Silva, P.S. Side-effects and complications of laser treatment in diabetic retinal disease. *Semin. Ophthalmol.* **2014**, *29*, 290–300, doi:10.3109/08820538.2014.959198.

22. Romero-Aroca, P.; Baget-Bernaldiz, M.; Pareja-Rios, A.; Lopez-Galvez, M.; Navarro-Gil, R.; Verges, R. Diabetic Macular Edema Pathophysiology: Vasogenic versus Inflammatory. *J. Diabetes Res.* **2016**, *2016*, doi:10.1155/2016/2156273.

23. Antonetti, D.A.; Barber, A.J.; Bronson, S.K.; Freeman, W.M.; Gardner, T.W.; Jefferson, L.S.; Kester, M.; Kimball, S.R.; Krady, J.K.; LaNoue, K.F.; et al. Diabetic retinopathy: seeing beyond glucose-induced microvascular disease. *Diabetes* **2006**, *55*, 2401–11, doi:10.2337/db05-1635.

24. Funk, R. Blood Supply of the Retina. *Ophthalmic Res.* **1997**, *29*, 320–325, doi:10.1159/000268030.

25. Allen, C.L.; Malhi, N.K.; Whatmore, J.D.; Bates, D.O.; Arkill, K.P. Non-invasive measurement of retinal permeability in a diabetic rat model. *Microcirculation* **2020**, *1*, doi:10.1111/micc.12623.

26. Simó, R.; Hernández, C. Neurodegeneration is an early event in diabetic retinopathy: Therapeutic implications. *Br. J. Ophthalmol.* **2012**, *96*, 1285–1290, doi:10.1136/bjophthalmol-2012-302005.

27. Thebeau, C.; Zhang, S.; Kolesnikov, A. V.; Kefalov, V.J.; Semenkovich, C.F.; Rajagopal, R. Light deprivation reduces the severity of experimental diabetic retinopathy. *Neurobiol. Dis.* **2020**, *137*, 104754, doi:10.1016/j.nbd.2020.104754.

28. Carrasco, E.; Hernandez, C.; Miralles, A.; Huguet, P.; Farres, J.; Simo, R.; Hernández, C.; Miralles, A.; Huguet, P.; Farrés, J.; et al. Lower Somatostatin Expression Is an Early Event in Diabetic Retinopathy and Is Associated With Retinal Neurodegeneration. *Diabetes Care* **2007**, *30*, 2902–2908, doi:10.2337/dc07-0332.Additional.

29. Barber, A.J.; Lieth, E.; Khin, S.A.; Antonetti, D.A.; Buchanan, A.G.; Gardner, T.W. Neural apoptosis in the retina during experimental and human diabetes: Early onset and effect of insulin. *J. Clin. Invest.* **1998**, *102*, 783–791, doi:10.1172/JCI2425.

30. Bogdanov, P.; Corraliza, L.; Villena, J.A.; Carvalho, A.R.; Garcia-Arumí, J.; Ramos, D.; Ruberte, J.; Simó, R.; Hernández, C. The db/db mouse: A useful model for the study of diabetic retinal neurodegeneration. *PLoS One* **2014**, *9*, doi:10.1371/journal.pone.0097302.

31. Duh, E.J.; Sun, J.K.; Stitt, A.W. Diabetic retinopathy: current understanding, mechanisms, and treatment strategies. *JCI insight* **2017**, *2*, 1–13, doi:10.1172/jci.insight.93751.

32. Busik, J. V.; Mohr, S.; Grant, M.B. Hyperglycemia-Induced reactive oxygen species toxicity to endothelial cells is dependent on paracrine mediators. *Diabetes* **2008**, *57*, 1952–1965, doi:10.2337/db07-1520.

33. Brownlee, M. Biochemistry and Molecular Cell Biology of Diabetic Complications. *Nature* **2001**, *414*, 813–820, doi:10.1038/414813a.

34. LEE, A.Y.W.; CHUNG, S.S.M. Contributions of polyol pathway to oxidative stress in diabetic cataract. *FASEB J.* **1999**, *13*, 23–30, doi:10.1096/fasebj.13.1.23.

35. McNulty, M.; Mahmud, A.; Feely, J. Advanced Glycation End-Products and Arterial Stiffness in Hypertension. *Am. J. Hypertens.* **2007**, *20*, 242–247, doi:10.1016/j.amjhyper.2006.08.009.

36. Xu, J.; Chen, L.J.; Yu, J.; Wang, H.J.; Zhang, F.; Liu, Q.; Wu, J. Involvement of Advanced Glycation End Products in the Pathogenesis of Diabetic Retinopathy. *Cell. Physiol. Biochem.* **2018**, *48*, 705–717, doi:10.1159/000491897.

37. Koya, D.; King, G.L. Perspectives in Diabetes Protein Kinase C Activation and the Development of Diabetic Complications. *Diabetes* **1998**, *47*, 859–866.

38. Korshunov, S.S.; Skulachev, V.P.; Starkov, A.A. High protonic potential actuates a mechanism of production of reactive oxygen species in mitochondria. *FEBS Lett.* **1997**, *416*, 15–18, doi:10.1016/S0014-5793(97)01159-9.

39. Krauss, R.M. Lipids and lipoproteins in patients with type 2 diabetes. *Diabetes Care* **2004**, *27*, 1496–1504, doi:10.2337/diacare.27.6.1496.

40. Chew, E.Y.; Klein, M.L.; Ferris, F.L.; Remaley, N.A.; Murphy, R.P.; Chantry, K.; Hoogwerf, B.J.; Miller, D. Association of elevated serum lipid levels with retinal hard exudate in diabetic retinopathy. Early Treatment Diabetic Retinopathy Study (ETDRS) Report 22. *Arch. Ophthalmol.* **1996**, *114*, 1079–84.

41. Cetin, E.N.; Bulgu, Y.; Ozdemir, S.; Topsakal, S.; Akin, F.; Aybek, H.; Yildirim, C. Association of serum lipid levels with diabetic retinopathy. *Int. J. Ophthalmol.* **2013**, *6*, 346–349, doi:10.3980/j.issn.2222-3959.2013.03.17.

42. Tikhonenko, M.; Lydic, T.A.; Wang, Y.; Chen, W.; Opreanu, M.; Sochacki, A.; McSorley, K.M.; Renis, R.L.; Kern, T.; Jump, D.B.; et al. Remodeling of retinal Fatty acids in an animal model of

diabetes: a decrease in long-chain polyunsaturated fatty acids is associated with a decrease in fatty acid elongases Elovl2 and Elovl4. *Diabetes* **2010**, *59*, 219–27, doi:10.2337/db09-0728.

43. Kady, N.M.; Liu, X.; Lydic, T.A.; Syed, M.H.; Navitskaya, S.; Wang, Q.; Hammer, S.S.; O'Reilly, S.; Huang, C.; Seregin, S.S.; et al. ELOVL4-Mediated Production of Very Long-Chain Ceramides Stabilizes Tight Junctions and Prevents Diabetes-Induced Retinal Vascular Permeability. *Diabetes* **2018**, *67*, 769–781, doi:10.2337/db17-1034.

44. Busik, J. V; Reid, G.E.; Lydic, T.A. Global Analysis of Retina Lipids by Complementary Precursor Ion and Neutral Loss Mode Tandem Mass Spectrometry. In *Lipidomics. Methods in Molecular Biology*; Armstrong, D., Ed.; Humana Press: Totowa, NJ, 2009; pp. 33–70 ISBN 978-1-60761-322-0.

45. Hannun, Y.A.; Obeid, L.M. Sphingolipids and their metabolism in physiology and disease. *Nat. Rev. Mol. Cell Biol.* **2018**, *19*, 175–191, doi:10.1038/nrm.2017.107.

46. Novgorodov, S. a; Szulc, Z.M.; Luberto, C.; Jones, J. a; Bielawski, J.; Bielawska, A.; Hannun, Y. a; Obeid, L.M. Positively charged ceramide is a potent inducer of mitochondrial permeabilization. *J. Biol. Chem.* **2005**, *280*, 16096–105, doi:10.1074/jbc.M411707200.

47. Hannun, Y.A.; Obeid, L.M. Principles of bioactive lipid signalling: Lessons from sphingolipids. *Nat. Rev. Mol. Cell Biol.* **2008**, *9*, 139–150, doi:10.1038/nrm2329.

48. Newton, J.; Lima, S.; Maceyka, M.; Spiegel, S. Revisiting the sphingolipid rheostat: Evolving concepts in cancer therapy. *Exp. Cell Res.* **2015**, *333*, 195–200, doi:10.1016/j.yexcr.2015.02.025.

49. Taniguchi, M.; Kitatani, K.; Kondo, T.; Hashimoto-Nishimura, M.; Asano, S.; Hayashi, A.; Mitsutake, S.; Igarashi, Y.; Umehara, H.; Takeya, H.; et al. Regulation of autophagy and its associated cell death by "sphingolipid rheostat": Reciprocal role of ceramide and sphingosine 1-phosphate in the mammalian target of rapamycin pathway. *J. Biol. Chem.* **2012**, *287*, 39898–39910, doi:10.1074/jbc.M112.416552.

50. Jenkins, R.W.; Canals, D.; Idkowiak-Baldys, J.; Simbari, F.; Roddy, P.; Perry, D.M.; Kitatani, K.; Luberto, C.; Hannun, Y.A. Regulated secretion of acid sphingomyelinase: Implications for selectivity of ceramide formation. *J. Biol. Chem.* **2010**, *285*, 35706–35718, doi:10.1074/jbc.M110.125609.

51. Schuchman, E.H.; Desnick, R.J. Types A and B Niemann-Pick disease. *Mol. Genet. Metab.* **2017**, *120*, 27–33, doi:10.1016/j.ymgme.2016.12.008.

52. Yu, Z.F.; Nikolova-Karakashian, M.; Zhou, D.; Cheng, G.; Schuchman, E.H.; Mattson, M.P. Pivotal role for acidic sphingomyelinase in cerebral ischemia-induced ceramide and cytokine production, and neuronal apoptosis. *J. Mol. Neurosci.* **2000**, *15*, 85–97, doi:10.1385/JMN:15:2:85.

53. Santana, P.; Peña, L.A.; Haimovitz-Friedman, A.; Martin, S.; Green, D.; McLoughlin, M.; Cordon-Cardo, C.; Schuchman, E.H.; Fuks, Z.; Kolesnick, R. Acid sphingomyelinase-deficient human lymphoblasts and mice are defective in radiation-induced apoptosis. *Cell* **1996**, *86*, 189–199, doi:10.1016/S0092-8674(00)80091-4.

54. Opreanu, M.; Tikhonenko, M.; Bozack, S.; Lydic, T.A.; Reid, G.E.; McSorley, K.M.; Sochacki, A.; Perez, G.I.; Esselman, W.J.; Kern, T.; et al. The unconventional role of acid sphingomyelinase in regulation of retinal microangiopathy in diabetic human and animal models. *Diabetes* **2011**, *60*, 2370–8, doi:10.2337/db10-0550.

55. Opreanu, M.; Lydic, T.A.; Reid, G.E.; McSorley, K.M.; Esselman, W.J.; Busik, J. V Inhibition of cytokine signaling in human retinal endothelial cells through downregulation of sphingomyelinases by docosahexaenoic acid. *Invest. Ophthalmol. Vis. Sci.* **2010**, *51*, 3253–63, doi:10.1167/iovs.09-4731.

56. Van Blitterswijk, W.J.; Van Der Luit, A.H.; Veldman, R.J.; Verheij, M.; Borst, J. Ceramide: Second messenger or modulator of membrane structure and dynamics? *Biochem. J.* **2003**, *369*, 199–211, doi:10.1042/BJ20021528.

57. Chakravarthy, H.; Navitskaya, S.; O'Reilly, S.; Gallimore, J.; Mize, H.; Beli, E.; Wang, Q.; Kady, N.; Huang, C.; Blanchard, G.J.; et al. Role of Acid Sphingomyelinase in Shifting the Balance between Proinflammatory and Reparative Bone Marrow Cells in Diabetic Retinopathy. *Stem Cells* **2016**, *34*, 972–983, doi:10.1002/stem.2259.

58. Devi, T.S.; Yumnamcha, T.; Yao, F.; Somayajulu, M.; Kowluru, R.A.; Singh, L.P. TXNIP mediates high glucose-induced mitophagic flux and lysosome enlargement in human retinal pigment epithelial cells. *Biol. Open* **2019**, *8*, 1–13, doi:10.1242/bio.038521.

59. Du, Y.; Miller, C.M.; Kern, T.S. Hyperglycemia increases mitochondrial superoxide in retina and retinal cells. *Free Radic. Biol. Med.* **2003**, *35*, 1491–1499, doi:10.1016/j.freeradbiomed.2003.08.018.

60. Kumar, B.; Kowluru, A.; Kowluru, R.A. Lipotoxicity augments glucotoxicity-induced mitochondrial damage in the development of diabetic retinopathy. *Invest. Ophthalmol. Vis. Sci.* **2015**, *56*, 2985–92, doi:10.1167/iovs.15-16466.

61. Trudeau, K.; Molina, A.J.A.; Guo, W.; Roy, S. High Glucose Disrupts Mitochondrial Morphology in Retinal Endothelial Cells: Implications for Diabetic Retinopathy. *Am. J. Pathol.* **2010**, *177*, 447–455, doi:10.2353/ajpath.2010.091029.

62. Roy, S.; Trudeau, K.; Roy, S.; Tien, T.; Barrette, K.F. Mitochondrial dysfunction and endoplasmic reticulum stress in diabetic retinopathy: mechanistic insights into high glucose-induced retinal cell death. *Curr. Clin. Pharmacol.* **2013**, *8*, 278–84.

63. Kogot-Levin, A.; Saada, A. Ceramide and the mitochondrial respiratory chain. *Biochimie* **2014**, *100*, 88–94, doi:10.1016/j.biochi.2013.07.027.

64. Dai, Q.; Liu, J.; Chen, J.; Durrant, D.; McIntyre, T.M.; Lee, R.M. Mitochondrial ceramide increases in UV-irradiated HeLa cells and is mainly derived from hydrolysis of sphingomyelin. *Oncogene* **2004**, *23*, 3650–3658, doi:10.1038/sj.onc.1207430.

65. Yu, J.; Novgorodov, S.A.; Chudakova, D.; Zhu, H.; Bielawska, A.; Bielawski, J.; Obeid, L.M.; Kindy, M.S.; Gudz, T.I. JNK3 signaling pathway activates ceramide synthase leading to mitochondrial dysfunction. *J. Biol. Chem.* **2007**, *282*, 25940–9, doi:10.1074/jbc.M701812200.

66. Managò, A.; Becker, K.A.; Carpinteiro, A.; Wilker, B.; Soddemann, M.; Seitz, A.P.; Edwards, M.J.; Grassmé, H.; Szabò, I.; Gulbins, E. *Pseudomonas aeruginosa* Pyocyanin Induces Neutrophil Death *via* Mitochondrial Reactive Oxygen Species and Mitochondrial Acid Sphingomyelinase. *Antioxid. Redox Signal.* **2015**, *22*, 1097–1110, doi:10.1089/ars.2014.5979.

67. BIRBES, H.; EL BAWAB, S.; HANNUN, Y.A.; OBEID, L.M. Selective hydrolysis of a mitochondrial pool of sphingomyelin induces apoptosis. *FASEB J.* **2001**, *15*, 2669–2679, doi:10.1096/fj.01-0539com.

68. Chang, K.-T.; Anishkin, A.; Patwardhan, G.A.; Beverly, L.J.; Siskind, L.J.; Colombini, M. Ceramide channels: destabilization by Bcl-xL and role in apoptosis. *Biochim. Biophys. Acta - Biomembr.* **2015**, *1848*, 2374–2384, doi:10.1016/j.bbamem.2015.07.013.

69. Colombini, M. Membrane channels formed by ceramide. *Handb. Exp. Pharmacol.* **2013**, 109–26, doi:10.1007/978-3-7091-1368-4_6.

70. Colombini, M. Ceramide channels and mitochondrial outer membrane permeability. *J. Bioenerg. Biomembr.* **2017**, *49*, 57–64, doi:10.1007/s10863-016-9646-z.

71. Siskind, L.J.; Kolesnick, R.N.; Colombini, M. Ceramide channels increase the permeability of the mitochondrial outer membrane to small proteins. *J. Biol. Chem.* **2002**, *277*, 26796–803, doi:10.1074/jbc.M200754200.

72. Perera, M.N.; Ganesan, V.; Siskind, L.J.; Szulc, Z.M.; Bielawski, J.; Bielawska, A.; Bittman, R.; Colombini, M. Ceramide channels: influence of molecular structure on channel formation in membranes. *Biochim. Biophys. Acta* **2012**, *1818*, 1291–1301, doi:10.1016/j.bbamem.2012.02.010.

73. Gudz, T.I.; Tserng, K.-Y.; Hoppel, C.L. Direct Inhibition of Mitochondrial Respiratory Chain Complex III by Cell-permeable Ceramide. *J. Biol. Chem.* **1997**, *272*, 24154–24158, doi:10.1074/jbc.272.39.24154.

74. Zimorski, V.; Ku, C.; Martin, W.F.; Gould, S.B. Endosymbiotic theory for organelle origins. *Curr. Opin. Microbiol.* **2014**, *22*, 38–48, doi:10.1016/j.mib.2014.09.008.

75. Nobel Prize in Chemistry for Biological Energy Transfer Available online: https://www.nobelprize.org/prizes/chemistry/1978/press-release/ (accessed on Mar 5, 2020).

76. Morelli, A.M.; Ravera, S.; Calzia, D.; Panfoli, I. An update of the chemiosmotic theory as suggested by possible proton currents inside the coupling membrane. *Open Biol.* **2019**, *9*, doi:10.1098/rsob.180221.

77. Brand, M.D.; Nicholls, D.G. Assessing mitochondrial dysfunction in cells. *Biochem. J.* **2011**, *435*, 297–312, doi:10.1042/BJ20110162.

78. Ortiz-Prado, E.; Dunn, J.F.; Vasconez, J.; Castillo, D.; Viscor, G. Partial pressure of oxygen in the human body: a general review. *Am. J. Blood Res.* **2019**, *9*, 1–14.

79. Gnaiger, E.; Lassnig, B.; Kuznetsov, a; Rieger, G.; Margreiter, R. Mitochondrial oxygen affinity,

respiratory flux control and excess capacity of cytochrome c oxidase. *J. Exp. Biol.* **1998**, *201*, 1129–1139.

80. Gnaiger, E. Polarographic Oxygen Sensors, the Oxygraph, and High-Resolution Respirometry to Assess Mitochondrial Function. In *Drug-Induced Mitochondrial Dysfunction*; Dykens, J.A., Will, Y., Eds.; John Wiley & Sons, Inc, 2008; pp. 327–351.

81. Pesta, D.; Gnaiger, E. High-Resolution Respirometry: OXPHOS Protocols for Human Cells and Permeabilized Fibers from Small Biopsies of Human Muscle. In *Methods in Molecular Biology*; Humana Press, 2012; pp. 25–58.

82. Salabei, J.K.; Gibb, A.A.; Hill, B.G. Comprehensive measurement of respiratory activity in permeabilized cells using extracellular flux analysis. *Nat. Protoc.* **2014**, *9*, 421–438, doi:10.1038/nprot.2014.018.

83. Clark, L.C.; Wolf, R.; Granger, D.; Taylor, Z. Continuous Recording of Blood Oxygen Tensions by Polarography. *J. Appl. Physiol.* **1953**, *6*, 189–193.

84. Otto, A.M. Warburg effect(s)—a biographical sketch of Otto Warburg and his impacts on tumor metabolism. *Cancer Metab.* **2016**, *4*, 1–8, doi:10.1186/s40170-016-0145-9.

85. Mookerjee, S.A.; Goncalves, R.L.S.; Gerencser, A.A.; Nicholls, D.G.; Brand, M.D. The contributions of respiration and glycolysis to extracellular acid production. *Biochim. Biophys. Acta - Bioenerg.* **2015**, *1847*, 171–181, doi:10.1016/j.bbabio.2014.10.005.

86. Lighton, J.R.B. *Measuring Metabolic Rates: A Manual for Scientists*; 1st ed.; Oxford University Press: New York, New York, 2008; Vol. 1; ISBN 9780195310610.

87. Gerencser, A.A.; Neilson, A.; Choi, S.W.; Edman, U.; Yadava, N.; Oh, R.J.; Ferrick, D.A.; Nicholls, D.G.; Brand, M.D. Quantitative microplate-based respirometry with correction for oxygen diffusion. *Anal. Chem.* **2009**, *81*, 6868–78, doi:10.1021/ac900881z.

88. Kondrashina, A. V.; Papkovsky, D.B.; Dmitriev, R.I. Measurement of cell respiration and oxygenation in standard multichannel biochips using phosphorescent O2-sensitive probes. *Analyst* **2013**, *138*, 4915, doi:10.1039/c3an00658a.

89. Severinghaus, J.W. First electrodes for blood PO2 and PCO2 determination. *J. Appl. Physiol.* **2004**, *97*, 1599–1600, doi:10.1152/classicessays.00021.2004.Editorial.

90. Bhalla, N.; Jolly, P.; Formisano, N.; Estrela, P. Introduction to biosensors. *Essays Biochem.* **2016**, *60*, 1–8, doi:10.1042/EBC20150001.

91. Severinghaus, J.W.; Freeman, B.A. Electrodes for Blood PO, and pC0, Determination. *J. Appl. Physiol.* **1958**, *13*, 515–520.

92. Chance, B.; Williams, G.R. Respiratory Enzymes in Oxidative Phosphorylation. *J. Biol.* **1955**, *1*, 409–428.

93. Hinkle, P.C. P/O ratios of mitochondrial oxidative phosphorylation. *Biochim. Biophys. Acta -*

Bioenerg. **2005**, *1706*, 1–11, doi:10.1016/j.bbabio.2004.09.004.

94. Oomen, P.E.; Skolimowski, M.; Verpoorte, S. Implementing Oxygen Control in Chip-Based Cell and Tissue Culture Systems. *Lab Chip* **2016**, *16*, 3394–3414, doi:10.1039/C6LC00772D.

95. Papkovsky, D.B.; Dmitriev, R.I. Biological detection by optical oxygen sensing. *Chem. Soc. Rev.* **2013**, *42*, 8700–8732, doi:10.1039/c3cs60131e.

96. Ochs, C.J.; Kasuya, J.; Pavesi, A.; Kamm, R.D. Oxygen levels in thermoplastic microfluidic devices during cell culture. *Lab Chip* **2014**, *14*, 459–62, doi:10.1039/c3lc51160j.

97. Khan, D.H.; Roberts, S.A.; Cressman, J.R.; Agrawal, N. Rapid Generation and Detection of Biomimetic Oxygen Concentration Gradients in Vitro. *Sci. Rep.* **2017**, *7*, 1–11, doi:10.1038/s41598-017-13886-z.

98. Lam, R.H.W.; Kim, M.C.; Thorsen, T. Culturing aerobic and anaerobic bacteria and mammalian cells with a microfluidic differential oxygenator. *Anal. Chem.* **2009**, *81*, 5918–5924, doi:10.1021/ac9006864.

99. Pham, T.D.; Wallace, D.C.; Burke, P.J. Microchambers with solid-state phosphorescent sensor for measuring single mitochondrial respiration. *Sensors* **2016**, *16*, doi:10.3390/s16071065.

100. Zand, K.; Pham, T.; Jr, A.D. Nanofluidic Platform for Single Mitochondria Analysis Using Fluorescence Microscopy. *Anal. …* **2013**, *85*, 6018–6025.

101. Kelbauskas, L.; Ashili, S.P.; Lee, K.B.; Zhu, H.; Tian, Y.; Meldrum, D.R. Simultaneous multiparameter cellular energy metabolism profiling of small populations of cells. *Sci. Rep.* **2018**, *8*, 1–12, doi:10.1038/s41598-018-22599-w.

102. Bénit, P.; Chrétien, D.; Porceddu, M.; Yanicostas, C.; Rak, M.; Rustin, P. An Effective, Versatile, and Inexpensive Device for Oxygen Uptake Measurement. *J. Clin. Med.* **2017**, *6*, 58, doi:10.3390/jcm6060058.

103. Molter, T.W.; Holl, M.R.; Dragavon, J.M.; McQuaide, S.C.; Anderson, J.B.; Young, A.C.; Burgess, L.W.; Lidstrom, M.E.; Meldrum, D.R. A new approach for measuring single-cell oxygen consumption rates. *IEEE Trans. Autom. Sci. Eng.* **2008**, *5*, 32–40, doi:10.1109/TASE.2007.909441.

104. Molter, T.W.; Mcquaide, S.C.; Suchorolski, M.T.; Strovas, T.J.; Lloyd, W.; Meldrum, D.R.; Lidstrom, M.E.; Hall, B.; Northlake, N.E.; Rm, P. A microwell array device capable of measuring single-cell oxygen consumption rates. *Sensors Actuators B Chem* **2009**, *135*, 678–686, doi:10.1016/j.snb.2008.10.036.A.

105. Oppegard, S.C.; Blake, A.J.; Williams, J.C.; Eddington, D.T. Precise control over the oxygen conditions within the Boyden chamber using a microfabricated insert. *Lab Chip* **2010**, *10*, 2366, doi:10.1039/c004856a.

106. Rogers, G.W.; Brand, M.D.; Petrosyan, S.; Ashok, D.; Elorza, A.A.; Ferrick, D.A.; Murphy, A.N. High throughput microplate respiratory measurements using minimal quantities of isolated mitochondria. *PLoS One* **2011**, *6*, e21746, doi:10.1371/journal.pone.0021746.

107. Divakaruni, A.S.; Paradyse, A.; Ferrick, D.A.; Murphy, A.N.; Jastroch, M. *Analysis and interpretation of microplate-based oxygen consumption and pH data*; 1st ed.; Elsevier Inc., 2014; Vol. 547; ISBN 1557-7988 (Electronic)r0076-6879 (Linking).

108. Divakaruni, A.S.; Wiley, S.E.; Rogers, G.W.; Andreyev, A.Y.; Petrosyan, S.; Loviscach, M.; Wall, E.A.; Yadava, N.; Heuck, A.P.; Ferrick, D.A.; et al. Thiazolidinediones are acute, specific inhibitors of the mitochondrial pyruvate carrier. *Proc. Natl. Acad. Sci.* **2013**, *110*, 5422–7, doi:10.1073/pnas.1303360110.

109. Haller, T.; Ortner, M.; Gnaiger, E. A Respirometer for Investigating Oxidative Cell Metabolism: Toward Optimization of Respiratory Studies. *Anal. Biochem.* **1994**, *218*, 338–342.

110. Gnaiger, E.; Steinlechner-Maran, R.; Méndez, G.; Eberl, T.; Margreiter, R. Control of mitochondrial and cellular respiration by oxygen. *J. Bioenerg. Biomembr.* **1995**, *27*, 583–596, doi:10.1007/BF02111656.

111. Steinlechner-Maran, R.; Eberl, T.; Kunc, M.; Margreiter, R.; Gnaiger, E. Oxygen dependence of respiration in coupled and uncoupled endothelial cells. *Am. J. Physiol. - Cell Physiol.* **1996**, *271*, doi:10.1152/ajpcell.1996.271.6.c2053.

112. Iliescu, C.; Taylor, H.; Avram, M.; Miao, J.; Franssila, S. A practical guide for the fabrication of microfluidic devices using glass and silicon. *Biomicrofluidics* **2012**, *6*, 16505–1650516, doi:10.1063/1.3689939.

113. Waheed, S.; Cabot, J.M.; Macdonald, N.P.; Lewis, T.; Guijt, R.M.; Paull, B.; Breadmore, M.C. 3D printed microfluidic devices: Enablers and barriers. *Lab Chip* **2016**, *16*, 1993–2013, doi:10.1039/c6lc00284f.

114. Gebhardt, A. *Understanding Additive Manufacturing*; 1st ed.; Hanser Publications: Cincinnati, 2011; ISBN 9781569905074.

115. Gross, B.C.; Erkal, J.L.; Lockwood, S.Y.; Chen, C.; Spence, D.M. Evaluation of 3D printing and its potential impact on biotechnology and the chemical sciences. *Anal. Chem.* **2014**, *86*, 3240–3253, doi:10.1021/ac403397r.

116. Rimington, R.P.; Capel, A.J.; Player, D.J.; Bibb, R.J.; Christie, S.D.R.; Lewis, M.P. Feasibility and Biocompatibility of 3D-Printed Photopolymerized and Laser Sintered Polymers for Neuronal, Myogenic, and Hepatic Cell Types. *Macromol. Biosci.* **2018**, *18*, 1–12, doi:10.1002/mabi.201800113.

117. Gross, B.C.; Anderson, K.B.; Meisel, J.E.; McNitt, M.I.; Spence, D.M. Polymer Coatings in 3D-Printed Fluidic Device Channels for Improved Cellular Adherence Prior to Electrical Lysis. *Anal. Chem.* **2015**, *87*, 6335–6341, doi:10.1021/acs.analchem.5b01202.

118. Nock, V.; Blaikie, R.J.; David, T. Patterning, integration and characterisation of polymer optical oxygen sensors for microfluidic devices. *Lab Chip* **2008**, *8*, 1300–1307, doi:10.1039/b801879k.

119. Carraway, E.R.; Demas, J.N.; DeGraff, B.A.; Bacon, J.R. Photophysics and Photochemistry of Oxygen Sensors Based on Luminescent Transition-Metal Complexes. *Anal. Chem.* **1991**, *63*, 337–

342, doi:10.1021/ac00004a007.

120. Fluorescence Quenching Studies Available online: https://www.chem.uzh.ch/de/study/download/year2/che211.html.

121. Forstner, H.; Gnaiger, E. Calculation of Equilibrium Oxygen Concentration. In *Polarographic Oxygen Sensors: Aquatic and Physiological Applications*; Gnaiger, E., Forstner, H., Eds.; Springer-Verlag Berline Heidelberg: Heidelberg, 1983; pp. 321–333 ISBN 978-3-642-81865-3.

122. Kneas, K.A.; Xu, W.; Demas, J.N.; Degraff, B.A. Oxygen sensors based on luminescence quenching: Interactions of tris(4,7-diphenyl-1,10-phenanthroline)ruthenium(II) chloride and pyrene with polymer supports. *Appl. Spectrosc.* **1997**, *51*, 1346–1351, doi:10.1366/0003702971942024.

123. Murphy, M.P. How understanding the control of energy metabolism can help investigation of mitochondrial dysfunction, regulation and pharmacology. *Biochim. Biophys. Acta - Bioenerg.* **2001**, *1504*, 1–11, doi:10.1016/S0005-2728(00)00234-6.

124. Rolfe, D.F.S.; Brown, G.C. Cellular energy utilization and molecular origin of standard metabolic rate in mammals. *Physiol. Rev.* **1997**, *77*, 731–758, doi:10.1152/physrev.1997.77.3.731.

125. Clerc, P.; Carey, G.B.; Mehrabian, Z.; Wei, M.; Hwang, H.; Girnun, G.D.; Chen, H.; Martin, S.S.; Polster, B.M. Rapid detection of an ABT-737-sensitive primed for death state in cells using microplate-based respirometry. *PLoS One* **2012**, *7*, 15–18, doi:10.1371/journal.pone.0042487.

126. Moreadith, R.W.; Lehninger, A.L. The pathways of glutamate and glutamine oxidation by tumor cell mitochondria. Role of mitochondrial NAD(P)+-dependent malic enzyme. *J. Biol. Chem.* **1984**, *259*, 6215–6221.

127. Hutter, E.; Renner, K.; Pfister, G.; Stöckl, P.; Jansen-Dürr, P.; Gnaiger, E. Senescence-associated changes in respiration and oxidative phosphorylation in primary human fibroblasts. *Biochem. J.* **2004**, *380*, 919–928, doi:10.1042/BJ20040095.

128. Keuper, M.; Jastroch, M.; Yi, C.X.; Fischer-Posovszky, P.; Wabitsch, M.; Tschöp, M.H.; Hofmann, S.M. Spare mitochondrial respiratory capacity permits human adipocytes to maintain ATP homeostasis under hypoglycemic conditions. *FASEB J.* **2014**, *28*, 761–770, doi:10.1096/fj.13-238725.

129. Kuznetsov, A. V.; Strobl, D.; Ruttmann, E.; Königsrainer, A.; Margreiter, R.; Gnaiger, E. Evaluation of mitochondrial respiratory function in small biopsies of liver. *Anal. Biochem.* **2002**, *305*, 186–194, doi:10.1006/abio.2002.5658.

130. Gnaiger, E. *Mitochondrial Pathways and Respiratory Control An Introduction to OXPHOS Analysis*; 2014; ISBN 9783950239966.

131. Brand, M.D.; Chien, L.F.; Diolez, P. Experimental discrimination between proton leak and redox slip during mitochondrial electron transport. *Biochem. J.* **1994**, *297*, 27–29, doi:10.1042/bj2970027.

132. Harper, M.; Brand, D. The Quantitative Contributions of Mitochondrial Proton Leak and ATP

Turnover Reactions to the Changed Respiration Rates of Hepatocytes from Rats of Different Thyroid Status. *J. Biol. Chem.* **1993**, *268*, 14850–14860.

133. Divakaruni, A.S.; Brand, M.D. The regulation and physiology of mitochondrial proton leak. *Physiology* **2011**, *26*, 192–205, doi:10.1152/physiol.00046.2010.

134. Ruas, J.S.; Siqueira-Santos, E.S.; Amigo, I.; Rodrigues-Silva, E.; Kowaltowski, A.J.; Castilho, R.F. Underestimation of the maximal capacity of the mitochondrial electron transport system in oligomycin-treated cells. *PLoS One* **2016**, *11*, 1–20, doi:10.1371/journal.pone.0150967.

135. Jaber, S.M.; Yadava, N.; Polster, B.M. Mapping Mitochondrial Respiratory Chain Deficiencies by Respirometry: Beyond the Mito Stress Test. *Exp. Neurol.* **2020**, doi:https://doi.org/10.1016/j.expneurol.2020.113282.

136. Fell, D.A. *Understanding the control of metabolism*; Fell, D.A., Snell, K., Eds.; Ashgate Publishing: Surrey, 1997;

137. Eigentler, A.; Draxl, A.; Wiethüchter, A. Laboratory protocol: citrate synthase a mitochondrial marker enzyme. *Mitochondrial Physiol. Netw.* **2015**, *04*, 1–11.

138. CHANCE, B.; WILLIAMS, G.R. Respiratory enzymes in oxidative phosphorylation. IV. The respiratory chain. *J. Biol. Chem.* **1955**, *217*, 429–438.

139. Picard, M.; Taivassalo, T.; Ritchie, D.; Wright, K.J.; Thomas, M.M.; Romestaing, C.; Hepple, R.T. Mitochondrial structure and function are disrupted by standard isolation methods. *PLoS One* **2011**, *6*, e18317, doi:10.1371/journal.pone.0018317.

140. Benador, I.Y.; Veliova, M.; Mahdaviani, K.; Petcherski, A.; Wikstrom, J.D.; Assali, E.A.; Acín-Pérez, R.; Shum, M.; Oliveira, M.F.; Cinti, S.; et al. Mitochondria Bound to Lipid Droplets Have Unique Bioenergetics, Composition, and Dynamics that Support Lipid Droplet Expansion. *Cell Metab.* **2018**, *27*, 869-885.e6, doi:10.1016/j.cmet.2018.03.003.

141. Kuznetsov, A. V.; Veksler, V.; Gellerich, F.N.; Saks, V.; Margreiter, R.; Kunz, W.S. Analysis of mitochondrial function in situ in permeabilized muscle fibers, tissues and cells. *Nat. Protoc.* **2008**, *3*, 965–976, doi:10.1038/nprot.2008.61.

142. Salabei, J.K.; Gibb, A.A.; Hill, B.G. Comprehensive measurement of respiratory activity in permeabilized cells using extracellular flux analysis Joshua. *Nat. Protoc.* **2014**, *9*, 421–438, doi:10.1016/j.pestbp.2011.02.012.Investigations.

143. Saks, V.A.; Belikova, Y.O.; Kuznetsov, A. V. In vivo regulation of mitochondrial respiration in cardiomyocytes: specific restrictions for intracellular diffusion of ADP. *Biochim. Biophys. Acta* **1991**, *1074*, 302–311, doi:10.1016/0304-4165(91)90168-G.

144. Mathers, K.E.; Staples, J.F. Saponin-permeabilization is not a viable alternative to isolated mitochondria for assessing oxidative metabolism in hibernation. *Biol. Open* **2015**, *4*, 858–864, doi:10.1242/bio.011544.

145. Picard, M.; Ritchie, D.; Wright, K.J.; Romestaing, C.; Thomas, M.M.; Rowan, S.L.; Taivassalo, T.;

Hepple, R.T. Mitochondrial functional impairment with aging is exaggerated in isolated mitochondria compared to permeabilized myofibers. *Aging Cell* **2010**, *9*, 1032–1046, doi:10.1111/j.1474-9726.2010.00628.x.

146. Munier-Lehmann, H.; Vidalain, P.O.; Tangy, F.; Janin, Y.L. On dihydroorotate dehydrogenases and their inhibitors and uses. *J. Med. Chem.* **2013**, *56*, 3148–3167, doi:10.1021/jm301848w.

147. Gnaiger, E. Mitochondrial Pathways to Complex I : Respiration with Glutamate and Malate. *Mitochondrial Physiol. Netw.* **2011**, *11*, 1–4.

148. Gnaiger, E. Capacity of oxidative phosphorylation in human skeletal muscle. New perspectives of mitochondrial physiology. *Int. J. Biochem. Cell Biol.* **2009**, *41*, 1837–1845, doi:10.1016/j.biocel.2009.03.013.

149. Puchowicz, M.A.; Varnes, M.E.; Cohen, B.H.; Friedman, N.R.; Kerr, D.S.; Hoppel, C.L. Oxidative phosphorylation analysis: Assessing the integrated functional activity of human skeletal muscle mitochondria - Case studies. *Mitochondrion* **2004**, *4*, 377–385, doi:10.1016/j.mito.2004.07.004.

150. Kimelberg, H.K.; Nicholls, P. Kinetic Studies on the Interaction c and Cytochrome of TMPD with c Oxidase ' Cytochrome Iieilin and Hartree first used p-phenylene- diamine routinely in the manometric assay of cytochrome c oxidase activity in heart muscle preparations chrome oxidase . He. *Arch. Biochem. Biophys.* **1969**, *133*, 327–335.

151. Gnaiger, E.; Boushel, R.; Søndergaard, H.; Munch-Andersen, T.; Damsgaard, R.; Hagen, C.; Díez-Sánchez, C.; Ara, I.; Wright-Paradis, C.; Schrauwen, P.; et al. Mitochondrial coupling and capacity of oxidative phosphorylation in skeletal muscle of Inuit and Caucasians in the arctic winter. *Scand. J. Med. Sci. Sport.* **2015**, *25*, 126–134, doi:10.1111/sms.12612.

152. Kasper, J.D.; Meyer, R.A.; Beard, D.A.; Wiseman, R.W. Effects of altered pyruvate dehydrogenase activity on contracting skeletal muscle bioenergetics. *Am. J. Physiol. - Regul. Integr. Comp. Physiol.* **2019**, *316*, R76–R86, doi:10.1152/ajpregu.00321.2018.

153. Wanders, R.J.A.; Westerhoff, H. V. Sigmoidal Relation between Mitochondrial Respiration and log ([ATP]/[ADP])OUtunder Conditions of Extramitochondrial ATP Utilization. Implications for the Control and Thermodynamics of Oxidative Phosphorylation. *Biochemistry* **1988**, *27*, 7832–7840, doi:10.1021/bi00420a037.

154. Jekabsons, M.B.; Nicholls, D.G. In Situ respiration and bioenergetic status of mitochondria in primary cerebellar granule neuronal cultures exposed continuously to glutamate. *J. Biol. Chem.* **2004**, *279*, 32989–33000, doi:10.1074/jbc.M401540200.

155. Zirath, H.; Rothbauer, M.; Spitz, S.; Bachmann, B.; Jordan, C.; Müller, B.; Ehgartner, J.; Priglinger, E.; Mühleder, S.; Redl, H.; et al. Every breath you take: Non-invasive real-time oxygen biosensing in two- and three-dimensional microfluidic cell models. *Front. Physiol.* **2018**, *9*, 1–12, doi:10.3389/fphys.2018.00815.

156. Kathuria, A.; Brouwers, N.; Buntinx, M.; Harding, T.; Auras, R. Effect of MIL-53 (Al) MOF particles on the chain mobility and crystallization of poly(L-lactic acid). *J. Appl. Polym. Sci.* **2017**, *53*, 45690, doi:10.1002/app.45690.

157. Auras, R.A.; Singh, S.P.; Singh, J.J. Evaluation of oriented poly(lactide) polymers vs. existing PET and oriented PS for fresh food service containers. *Packag. Technol. Sci.* **2005**, *18*, 207–216, doi:10.1002/pts.692.

158. Frezza, C.; Cipolat, S.; Scorrano, L. Organelle isolation: functional mitochondria from mouse liver, muscle and cultured fibroblasts. *Nat. Protoc.* **2007**, *2*, 287–95, doi:10.1038/nprot.2006.478.

159. Green, E.J.; Carritt, D.E. Oxygen Solubility in Sea Water: Thermodynamic Influence of Sea Salt. *Science (80-.).* **1967**, *157*, 191–193.

160. Gillanders, R.N.; Tedford, M.C.; Crilly, P.J.; Bailey, R.T. Thin film dissolved oxygen sensor based on platinum octaethylporphyrin encapsulated in an elastic fluorinated polymer. *Anal. Chim. Acta* **2004**, *502*, 1–6, doi:10.1016/j.aca.2003.09.053.

161. Thomas, P.C.; Raghavan, S.R.; Forry, S.P. Regulating Oxygen Levels in a Microfluidic Device. *Anal. Chem.* **2011**, *83*, 8821–8824, doi:10.1021/ac202300g.

162. Krab, K.; Kempe, H.; Wikström, M. Explaining the enigmatic KM for oxygen in cytochrome c oxidase: A kinetic model. *Biochim. Biophys. Acta - Bioenerg.* **2011**, *1807*, 348–358, doi:10.1016/J.BBABIO.2010.12.015.

163. Vellonen, K.-S.; Malinen, M.; Mannermaa, E.; Subrizi, A.; Toropainen, E.; Lou, Y.-R.; Kidron, H.; Yliperttula, M.; Urtti, A. A critical assessment of in vitro tissue models for ADME and drug delivery. *J. Control. release* **2014**, *190C*, 94–114, doi:10.1016/j.jconrel.2014.06.044.

164. Horan, M.P.; Pichaud, N.; Ballard, J.W.O. Review: Quantifying mitochondrial dysfunction in complex diseases of aging. *Journals Gerontol. - Ser. A Biol. Sci. Med. Sci.* **2012**, *67 A*, 1022–1035, doi:10.1093/gerona/glr263.

165. Arato-Oshima, T.; Matsui, H.; Wakizaka, A.; Homareda, H. Mechanism responsible for oligomycin-induced occlusion of Na+ within Na/K-ATPase. *J. Biol. Chem.* **1996**, *271*, 25604–25610, doi:10.1074/jbc.271.41.25604.

166. Glaser, E.; Norling, B.; Kopecky, J.; Ernster, L. Comparison of the Effects of Oligomycin and Dicyclohexylcarbodiimide on Mitochondrial ATPase and Related Reactions. *Eur. J. Biochem.* **1982**, *121*, 525–531, doi:10.1111/j.1432-1033.1982.tb05818.x.

167. Padman, B.S.; Bach, M.; Lucarelli, G.; Prescott, M.; Ramm, G. The protonophore CCCP interferes with lysosomal degradation of autophagic cargo in yeast and mammalian cells. *Autophagy* **2013**, *9*, 1862–1875, doi:10.4161/auto.26557.

168. Heytler, P.G. Uncoupling of Oxidative Phosphorylation by Carbonyl Cyanide Phenylhydrazones. I. Some Characteristics of m-Cl-CCP Action on Mitochondria and Chloroplasts. *Biochemistry* **1963**, *2*, 357–361, doi:10.1021/bi00902a031.

169. Yun, H.; Kim, K.; Lee, W.G. Effect of a dual inlet channel on cell loading in microfluidics. *Biomicrofluidics* **2014**, *8*, 1–9, doi:10.1063/1.4901929.

170. Kolnik, M.; Tsimring, L.S.; Hasty, J. Vacuum-assisted cell loading enables shear-free mammalian

microfluidic culture. *Lab Chip* **2012**, *12*, 4732–4737, doi:10.1039/c2lc40569e.Vacuum-assisted.

171. Grist, S.M.; Chrostowski, L.; Cheung, K.C. Optical oxygen sensors for applications in microfluidic cell culture. *Sensors* **2010**, *10*, 9286–9316, doi:10.3390/s101009286.

172. Abaci, H.E.; Devendra, R.; Smith, Q.; Gerecht, S.; Drazer, G. Design and development of microbioreactors for long-term cell culture in controlled oxygen microenvironments. *Biomed. Microdevices* **2012**, *14*, 145–52, doi:10.1007/s10544-011-9592-9.

173. Lemasters, J.J. The ATP-to-Oxygen Stoichiometries of Oxidative Phosphorylation by Rat Liver Mitochondria. *J. Biol. Chem.* **1984**, *259*, 13123–13130.

174. Chau, L.; Doran, M.; Cooper-White, J. A novel multishear microdevice for studying cell mechanics. *Lab Chip* **2009**, *9*, 1897–1902, doi:10.1039/b823180j.

175. Shao, J.; Wu, L.; Wu, J.; Zheng, Y.; Zhao, H.; Jin, Q.; Zhao, J. Integrated microfluidic chip for endothelial cells culture and analysis exposed to a pulsatile and oscillatory shear stress. *Lab Chip* **2009**, *9*, 3118–3125, doi:10.1039/b909312e.

176. Oyre, S.; Pedersen, E.M.; Ringgaard, S.; Boesiger, P.; Paaske, W.P. In vivo wall shear stress measured by magnetic resonance velocity mapping in the normal human abdominal aorta. *Eur. J. Vasc. Endovasc. Surg.* **1997**, *13*, 263–271, doi:10.1016/S1078-5884(97)80097-4.

177. Fröhlich, E.; Bonstingl, G.; Höfler, A.; Meindl, C.; Leitinger, G.; Pieber, T.R.; Roblegg, E. Comparison of two in vitro systems to assess cellular effects of nanoparticles-containing aerosols. *Toxicol. Vitr.* **2013**, *27*, 409–417, doi:10.1016/j.tiv.2012.08.008.

178. Chen, F.; Luo, Y.; Tsoutsos, N.G.; Maniatakos, M.; Shahin, K.; Gupta, N. Embedding Tracking Codes in Additive Manufactured Parts for Product Authentication. *Adv. Eng. Mater.* **2018**, *1800495*, 1–8, doi:10.1002/adem.201800495.

179. Robins, M.; Solomon, J.B.; Samei, E. Can a 3D task transfer function accurately represent the signal transfer properties of low-contrast lesions in non-linear CT systems? *Med. Imaging 2018 Phys. Med. Imaging* **2018**, *10573*, 148, doi:10.1117/12.2294588.

180. Simó, R.; Villarroel, M.; Corraliza, L.; Hernández, C.; Garcia-Ramírez, M. The retinal pigment epithelium: something more than a constituent of the blood-retinal barrier--implications for the pathogenesis of diabetic retinopathy. *J. Biomed. Biotechnol.* **2009**, *2010*, 15, doi:10.1155/2010/190724.

181. R. Sparrrow, J.; Hicks, D.; P. Hamel, C. The Retinal Pigment Epithelium in Health and Disease. *Curr. Mol. Med.* **2010**, *10*, 802–823, doi:10.2174/156652410793937813.

182. Berkowitz, B.A.; Olds, H.K.; Richards, C.; Joy, J.; Rosales, T.; Podolsky, R.H.; Childers, K.L.; Brad Hubbard, W.; Sullivan, P.G.; Gao, S.; et al. Novel imaging biomarkers for mapping the impact of mild mitochondrial uncoupling in the outer retina in vivo. *PLoS One* **2020**, *15*, 1–16, doi:10.1371/journal.pone.0226840.

183. Saint-Geniez, M.; Kurihara, T.; Sekiyama, E.; Maldonado, A.E.; D'Amore, P. a An essential role for

RPE-derived soluble VEGF in the maintenance of the choriocapillaris. *Proc. Natl. Acad. Sci. U. S. A.* **2009**, *106*, 18751–18756, doi:10.1073/pnas.0905010106.

184. Ion, G.; Fajka-Boja, R.; Kovács, F.; Szebeni, G.; Gombos, I.; Czibula, Á.; Matkó, J.; Monostori, É. Acid sphingomyelinase mediated release of ceramide is essential to trigger the mitochondrial pathway of apoptosis by galectin-1. *Cell. Signal.* **2006**, *18*, 1887–1896, doi:10.1016/j.cellsig.2006.02.007.

185. Tikhonenko, M.; Lydic, T.A.; Opreanu, M.; Li Calzi, S.; Bozack, S.; McSorley, K.M.; Sochacki, A.L.; Faber, M.S.; Hazra, S.; Duclos, S.; et al. N-3 polyunsaturated Fatty acids prevent diabetic retinopathy by inhibition of retinal vascular damage and enhanced endothelial progenitor cell reparative function. *PLoS One* **2013**, *8*, e55177, doi:10.1371/journal.pone.0055177.

186. Novgorodov, S.A.; Gudz, T.I. Ceramide and mitochondria in ischemic brain injury. *Int. J. Biochem. Mol. Biol.* **2011**, *2*, 347–61.

187. France-Lanord, V.; Brugg, B.; Michel, P.P.; Agid, Y.; Ruberg, M. Mitochondrial free radical signal in ceramide-dependent apoptosis: a putative mechanism for neuronal death in Parkinson's disease. *J. Neurochem.* **1997**, *69*, 1612–1621, doi:10.1046/j.1471-4159.1997.69041612.x.

188. Fox, T.E.; Han, X.; Kelly, S.; Merrill, A.H.; Martin, R.E.; Anderson, R.E.; Gardner, T.W.; Kester, M. Diabetes alters sphingolipid metabolism in the retina: A potential mechanism of cell death in diabetic retinopathy. *Diabetes* **2006**, *55*, 3573–3580, doi:10.2337/db06-0539.

189. Jaffe, G.J.; Earnest, K.; Fulcher, S.; Lui, M.; Houston, L.L. Antitransferrin Receptor Immunotoxin Inhibits Proliferating Human Retinal Pigment Epithelial Cells. *Arch. Ophthalmol.* **1990**, *108*, 1163–1168, doi:10.1001/archopht.1990.01070100119046.

190. Clayton, D.A.; Shadel, G.S. Purification of mitochondria by sucrose step density gradient centrifugation. *Cold Spring Harb. Protoc.* **2014**, *2014*, 1115–1117, doi:10.1101/pdb.prot080028.

191. Clayton, D.A.; Shadel, G.S. Isolation of mitochondria from cells and tissues. *Cold Spring Harb. Protoc.* **2014**, *2014*, 1040–1041, doi:10.1101/pdb.top074542.

192. Lydic, T.A.; Busik, J. V.; Reid, G.E. A monophasic extraction strategy for the simultaneous lipidome analysis of polar and nonpolar retina lipids. *J. Lipid Res.* **2014**, *55*, 1797–1809, doi:10.1194/jlr.D050302.

193. Byeon, S.K.; Lee, J.Y.; Lee, J.S.; Moon, M.H. Lipidomic profiling of plasma and urine from patients with Gaucher disease during enzyme replacement therapy by nanoflow liquid chromatography-tandem mass spectrometry. *J. Chromatogr. A* **2015**, *1381*, 132–139, doi:10.1016/j.chroma.2015.01.004.

194. Haimi, P.; Uphoff, A.; Hermansson, M.; Somerharju, P. Software tools for analysis of mass spectrometric lipidome data. *Anal. Chem.* **2006**, *78*, 8324–8331, doi:10.1021/ac061390w.

195. Levitsky, Y.; Pegouske, D.J.; Hammer, S.S.; Frantz, N.L.; Fisher, K.P.; Muchnik, A.B.; Saripalli, A.R.; Kirschner, P.; Bazil, J.N.; Busik, J. V.; et al. Micro-respirometry of whole cells and isolated mitochondria. *RSC Adv.* **2019**, *9*, 33257–33267, doi:10.1039/c9ra05289e.

196. Novgorodov, S.A.; Wu, B.X.; Gudz, T.I.; Bielawski, J.; Ovchinnikova, T. V; Hannun, Y.A.; Obeid, L.M. Novel pathway of ceramide production in mitochondria: thioesterase and neutral ceramidase produce ceramide from sphingosine and acyl-CoA. *J. Biol. Chem.* **2011**, *286*, 25352–62, doi:10.1074/jbc.M110.214866.

197. Erdreich-Epstein, A.; Tran, L.B.; Bowman, N.N.; Wang, H.; Cabot, M.C.; Durden, D.L.; Vlckova, J.; Reynolds, C.P.; Stins, M.F.; Groshen, S.; et al. Ceramide signaling in fenretinide-induced endothelial cell apoptosis. *J. Biol. Chem.* **2002**, *277*, 49531–7, doi:10.1074/jbc.M209962200.

198. Perry, D.M.; Newcomb, B.; Adada, M.; Wu, B.X.; Roddy, P.; Kitatani, K.; Siskind, L.; Obeid, L.M.; Hannun, Y.A. Defining a Role for Acid Sphingomyelinase in the p38/Interleukin-6 Pathway. *J. Biol. Chem.* **2014**, *289*, 22401–22412, doi:10.1074/jbc.M114.589648.

199. Novgorodov, S.A.; Riley, C.L.; Yu, J.; Keffler, J.A.; Clarke, C.J.; Van Laer, A.O.; Baicu, C.F.; Zile, M.R.; Gudz, T.I. Lactosylceramide contributes to mitochondrial dysfunction in diabetes. *J. Lipid Res.* **2016**, *57*, 546–562, doi:10.1194/jlr.M060061.

200. Kappler, L.; Li, J.; Häring, H.U.; Weigert, C.; Lehmann, R.; Xu, G.; Hoene, M. Purity matters: A workflow for the valid high-resolution lipid profiling of mitochondria from cell culture samples. *Sci. Rep.* **2016**, *6*, 1–10, doi:10.1038/srep21107.

201. Franko, A.; Baris, O.R.; Bergschneider, E.; Von Toerne, C.; Hauck, S.M.; Aichler, M.; Walch, A.K.; Wurst, W.; Wiesner, R.J.; Johnston, I.C.D.; et al. Efficient isolation of pure and functional mitochondria from mouse tissues using automated tissue disruption and enrichment with anti-TOM22 magnetic beads. *PLoS One* **2013**, *8*.

202. Larsen, S.; Nielsen, J.; Hansen, C.N.; Nielsen, L.B.; Wibrand, F.; Stride, N.; Schroder, H.D.; Boushel, R.; Helge, J.W.; Dela, F.; et al. Biomarkers of mitochondrial content in skeletal muscle of healthy young human subjects. *J. Physiol.* **2012**, *590*, 3349–60, doi:10.1113/jphysiol.2012.230185.

203. Kern, T.S.; Antonetti, D.A.; Smith, L.E.H. Pathophysiology of Diabetic Retinopathy: Contribution and Limitations of Laboratory Research. *Ophthalmic Res.* **2019**, *62*, 196–202, doi:10.1159/000500026.

204. Babiychuk, E.B.; Atanassoff, A.P.; Monastyrskaya, K.; Brandenberger, C.; Studer, D.; Allemann, C.; Draeger, A. The targeting of plasmalemmal ceramide to mitochondria during apoptosis. *PLoS One* **2011**, *6*, doi:10.1371/journal.pone.0023706.

205. Kowluru, R.A. Diabetic retinopathy, metabolic memory and epigenetic modifications. *Vision Res.* **2017**, *139*, 30–38, doi:10.1016/j.visres.2017.02.011.

206. Alivand, M.R.; Soheili, Z.S.; Pornour, M.; Solali, S.; Sabouni, F. Novel Epigenetic Controlling of Hypoxia Pathway Related to Overexpression and Promoter Hypomethylation of TET1 and TET2 in RPE Cells. *J. Cell. Biochem.* **2017**, *118*, 3193–3204, doi:10.1002/jcb.25965.

207. Desjardins, D.; Liu, Y.; Crosson, C.E.; Ablonczy, Z. Histone Deacetylase Inhibition Restores Retinal Pigment Epithelium Function in Hyperglycemia. *PLoS One* **2016**, *11*, 1–16, doi:10.1371/journal.pone.0162596.

208. Dolinko, A.H.; Chwa, M.; Atilano, S.R.; Kenney, M.C. African and Asian Mitochondrial DNA Haplogroups Confer Resistance Against Diabetic Stresses on Retinal Pigment Epithelial Cybrid Cells In Vitro. *Mol. Neurobiol.* **2020**, *57*, 1636–1655, doi:10.1007/s12035-019-01834-z.

209. Peng, Q.H.; Tong, P.; Gu, L.M.; Li, W.J. Astragalus polysaccharide attenuates metabolic memory-triggered ER stress and apoptosis via regulation of miR-204/SIRT1 axis in retinal pigment epithelial cells. *Biosci. Rep.* **2020**, *40*, 1–15, doi:10.1042/BSR20192121.

210. Roy, S.; Sala, R.; Cagliero, E.; Lorenzi, M. Overexpression of fibronectin induced by diabetes or high glucose: Phenomenon with a memory. *Proc. Natl. Acad. Sci. U. S. A.* **1990**, *87*, 404–408, doi:10.1073/pnas.87.1.404.

211. Duraisamy, A.J.; Mohammad, G.; Kowluru, R.A. Mitochondrial fusion and maintenance of mitochondrial homeostasis in diabetic retinopathy. *Biochim. Biophys. Acta - Mol. Basis Dis.* **2019**, *1865*, 1617–1626, doi:10.1016/j.bbadis.2019.03.013.

212. Qi, X.; Mitter, S.K.; Yan, Y.; Busik, J. V; Grant, M.B.; Boulton, M.E. Diurnal Rhythmicity of Autophagy Is Impaired in the Diabetic Retina. *Cells* **2020**, *9*, 1–17, doi:10.3390/cells9040905.

213. Weinbach, E.C.; Costa, J.L.; Nelson, B.D.; Claggett, C.E.; Hundal, T.; Bradley, D.; Morris, S.J. Effects of tricyclic antidepressant drugs on energy-linked reactions in mitochondria. *Biochem. Pharmacol.* **1986**, *35*, 1445–1451, doi:10.1016/0006-2952(86)90108-5.